Master Thesis Mechanical Engineering
Document Number: 358

A Numerical Study to help understand the effects of Nasal High Flow Therapy using the Lattice Boltzmann Method

B.J. Wessels
December 2020

Graduation committee:
dr. ir. R. Hagmeijer
Dr.-Ing. K. Jain
ir. R.H.J. Hebbink
Dr.-Ing. J. Arens

Department of Thermal Fluid Engineering
Engineering Fluid Dynamics
Faculty of Engineering Technology

University of Twente
P.O. Box 217
7500 AE Enschede
The Netherlands

Abstract

Nasal High Flow Therapy (NHFT) is a treatment method for people with COPD. During Nasal High Flow Therapy, a heated and humidified airflow is supplied via cannulas in the nostrils under a high flow rate, creating positive end-expiratory pressure and washing out the death space in the nasal cavities. The exact working mechanisms and optimal therapy settings of NHFT are unknown and understanding this can help patients. Numerical methods, such as the Lattice Boltzmann Method (LBM), can simulate and visualize the airflow in the nasal cavities and therefore help in understanding the physics during NHFT.

To study the effects of Nasal High Flow Therapy, the computational Lattice Boltzmann method is used which is able to simulate the flow in the complex geometry of the human nose. Lattice Boltzmann simulations are performed in the LBM solver Musubi. A 2D benchmark case of flow around a cylinder and an other case of blood flow in a femoral artery bifurcation are simulated to gain more insight in the LBM. The results are compared with results that are obtained by using the Finite Volume Method (Fluent) and the Finite Element Method (SimVascular) respectively and show good agreement.

To simulate the airflow in the nose, a geometry obtained directly from a CT-scan of the nasal cavities up until the trachea is used. Experiments are conducted parallel to this work, using a 3D-printed version of the same geometry with several pressure tap measurements. Airflow is generated by a lung simulator that is connected to the trachea.
Unassisted breathing simulations are performed using a realistic transient breathing profile for both inspiration and expiration. Meshes with $\pm$ 1000M cells are used to obtain high resolution solutions.
Velocity and vorticity plots are calculated at several intersection planes in the geometry. Pharyngeal and laryngeal jets with high velocity magnitudes are observed during exhalation and inhalation. Recirculation in the region of the olfactory cleft is observed. Pressure drop is directly compared with experiments and are in good agreement.

Simulations of NHFT have not been performed, but the unassisted breathing simulations in this work pave the path towards future NHFT simulations with LBM, which will require even higher resolutions or local mesh refinements due to high Reynolds numbers.

Keywords: Lattice Boltzmann Method; Nasal High Flow Therapy; Human Airflow; Transient simulation; Nasal Cavities; Musubi; Breathing profile; High resolution; Computational Fluid Dynamics.

List of Symbols & Abbreviations

Abbreviations

AE	Acute Exacerbation
AFP	Arteria Femoralis Profunda
AFS	Arteria Femoralis Superficialis
BGK	Bhatnagar–Gross–Krook (operator)
CFD	Computational Fluid Dynamics
COPD	Chronic Obstructive Pulmonary Disease
CT	Computed Tomography
DNS	Direct Numerical Simulation
FDM	Finite Difference Method
FEM	Finite Element Method
FHP	Frish, Hasslacher and Pomeau
FVM	Finite Volume Method
LBM	Lattice Boltzmann Method
LES	Large Eddy Simulation
LIC	Line Integral Convolution
NHFT	Nasal High Flow Therapy
NIMV	Non-Invasive Mechanical Ventilation
PEEP	Positive End-Expiratory Pressure
PIV	Particle Image Velocimetry
RANS	Reynolds Averaged Navier-Stokes
RCR	Resistor–Capacitor-Resistor

Roman symbols

C	Lattice velocity	**[**$h/\Delta t$ **or** m/s**]**
C_D	Drag coefficient	**[-]**
C_L	Lift coefficient	**[-]**
C_s	Smagorinsky–Lilly model coefficient	**[-]**

c_s	(Lattice) speed of sound	[$h/\Delta t$ **or** m/s]
D_h	Hydraulic diameter	[m]
e_i	Unit velocity	[m/s]
F	Force	[$kg \cdot m/s^2$]
f	Distribution function	[-]
h	Grid spacing	[m]
m	Mass	[kg]
Ma	(Lattice) Mach number	[-]
p	Momentum	[$kg \cdot m/s$]
Re	Reynolds number	[-]
St	Strouhal number	[-]
t	Time	[s]
u	Velocity	[m/s]
w_i	Weighting factor	[-]
x	Global coordinate	[m]
S_{ij}	Rate of strain tensor	[$1/s$]

Greek symbols

μ	Dynamic viscosity parameter	[$kg/m \cdot s$]
ν	Kinematic viscosity parameter	[m^2/s]
ρ	Density	[kg/m^3]
τ	Relaxation parameter	[-]

Contents

1 Introduction **7**
1.1 Chronic Obstructive Pulmonary Disease . . . 7
1.2 Nasal High Flow Therapy . . . 8
1.3 Computational methods in Nasal High Flow Therapy . . . 9
1.4 Previous work . . . 9
1.4.1 Airflow during unassisted breathing . . . 9
1.4.2 Nasal High Flow Therapy . . . 11
1.5 Research Question . . . 12
1.6 Thesis outline . . . 12

2 Theory **13**
2.1 The Boltzmann equation . . . 13
2.2 Lattice Gas Cellular Automata . . . 14
2.2.1 Lattice Gas Cellular Automata in fluid flows . . . 14
2.3 Lattice Boltzmann Method . . . 14
2.3.1 Lattice parameters . . . 17
2.3.2 Choosing the parameters . . . 19
2.3.3 Boundary conditions . . . 19
2.4 APES . . . 22
2.4.1 Seeder . . . 22
2.4.2 Musubi . . . 23
2.4.3 Execution of the code . . . 23

3 Comparison of Lattice Boltzmann method with the Finite Volume Method **25**
3.1 Benchmark case description . . . 25
3.2 Kármán vortex street: Results and performance of LBM . . . 25
3.3 Comparison with Ansys Fluent . . . 27
3.3.1 Flow physics comparison . . . 29
3.3.2 Velocity profiles . . . 30

4 Flow in a femoral artery bifurcation: A comparison of Lattice Boltzmann and the Finite Element method **33**
4.1 Case description . . . 33
4.2 Results . . . 34
4.3 Discussion . . . 34

5 Unassisted breathing: Case description and methodology **43**
5.1 Geometry . . . 43
5.2 Experimental set-up . . . 43
5.3 Breathing profile . . . 44
5.3.1 Expiration boundary conditions . . . 44
5.3.2 Inspiration boundary conditions . . . 45
5.4 Volume flow rate ratio estimation during inhalation . . . 45
5.4.1 Approach . . . 46
5.4.2 Results . . . 46
5.5 Flow and simulation parameters . . . 47
5.6 Grid convergence . . . 48
5.7 Mesh configuration . . . 50

5.8 Last notes . . . 51

6 Lattice Boltzmann method in unassisted breathing 53
6.1 Inhalation . . . 53
6.2 Exhalation . . . 60
6.3 Discussion . . . 64
6.3.1 Inhalation . . . 64
6.3.2 Exhalation . . . 69
6.3.3 Concluding remarks . . . 69

7 Lattice Boltzmann method in Nasal High Flow Therapy 71
7.1 Case description . . . 71
7.2 Dimensionless numbers . . . 71
7.3 On Boundary conditions . . . 72

8 Recommendations and limitations 75

9 Conclusion 77

Appendices 87

A Binary update functions in Lattice Gas Automata 89

B Nasal geometry grid convergence 91

C Final Mesh 93

D Extra images of unassisted breathing 95
D.1 Discussion . . . 104

1 | Introduction

The respiratory tract has the important task to provide the human body with oxygen. A schematic overview of the respiratory tract can be seen in figure 1.1. It can be split into two parts, the upper respiratory tract and the lower respiratory tract. The upper respiratory tract consists of the nasal cavity with the paranasal sinuses, the pharynx and the larynx. The nasal cavity is divided into two nasal passages in which air moves during breathing. The nasal cavity and the paranasal sinuses together make sure that the air is filtered, warmed and humidified before it enters the lungs.
The lower respiratory tract consists of the tracheobronchial tree (the trachea, the bronchi, the bronchioles and the alveoli). The latter three make up the lungs. For a healthy person, breathing is the most common thing to do and it happens (almost) unconsciously. However, there are some diseases that can occur in the respiratory tract which can impact the live of these people significantly. One of these diseases is Chronic Obstructive Pulmonary Disease.

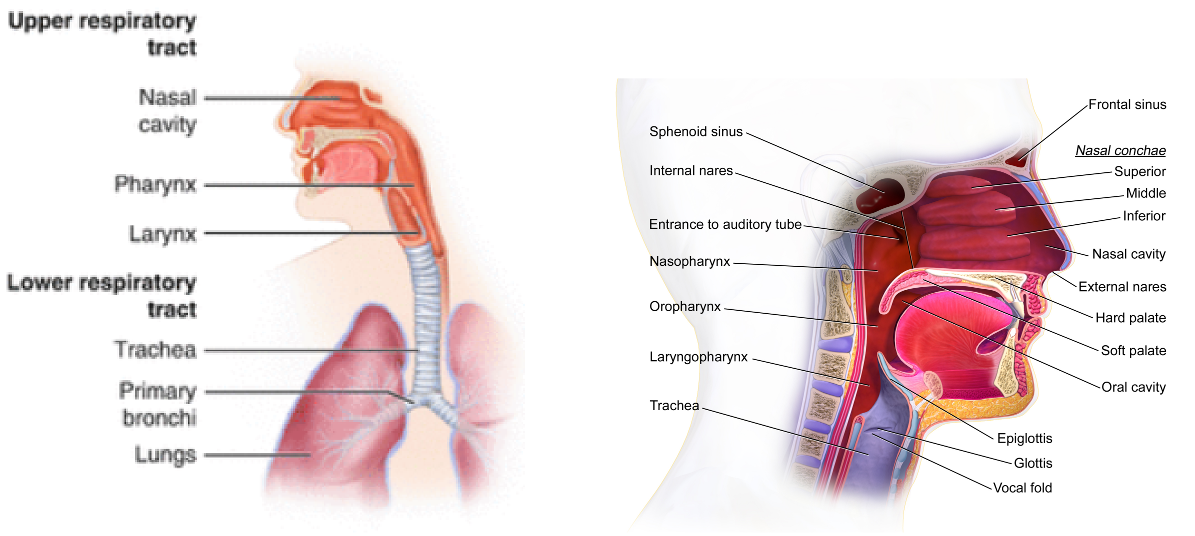

Figure 1.1: Left: Schematic overview of the respiratory tract with the upper and lower region [25], Right: Detailed overview of the upper respiratory tract [9].

1.1 Chronic Obstructive Pulmonary Disease

Chronic Obstructive Pulmonary Disease (COPD) is an umbrella term for a number of respiratory diseases including chronic bronchitis, chronic respiratory failure and emphysema [78]. The main cause of COPD is smoking. Symptoms slowly progress over the years and are being noticed by being out of breath, coughing and the production of sputum [72]. COPD can lead in premature death and is irreversible, making it very important that COPD is detected early to reduce decline in respiratory function [78]. The World Health Organization stated that COPD is the fourth leading cause of death in the world, causing approximately 2.75 million deaths annually [78]. Apart from the symptoms, COPD can cause acute exacerbation (AE): acute worsening of symptoms in the respiratory tract. These exacerbations cause most burden on healthcare systems, with an estimated 70% of the total COPD-related costs [98, 93]. AECOPD is often triggered by environmental pollution or infections and viruses. AECOPD causes a rapid decline in a person's health and is associated with high mortality.
AECOPD treatment can be split in pharmacological treatments and non-pharmacological treatments. Pharmacologic treatment is the treatment that involve drugs. For AECOPD, often bronchodilators such as SABA are prescribed, but also

steroids and antibiotics can be prescribed [12]. Bronchodilators dilate the airways, therefore decreasing the resistance in the respiratory tract and increasing the flow of air to the lungs. According to Crisafulli et al. [12], the use of steroids during AECOPD is justified from solid evidence, while the use of bronchodilators is not proven to be effective.
Non-pharmacological treatment methods that are used for AECOPD are Nasal High Flow Therapy (NHFT), Non-invasive mechanical ventilation (NIMV) and pulmonary rehabilitation [93, 12]. Non-Invasive Mechanical Ventilation is a treatment method where breathing is assisted by providing oxygenated gas to the airways via a tight-fitting facial mask [88]. Study shows that NIMV treatment can improve the survival of critically ill patients suffering from AECOPD [24, 30]. However, the main drawback of NIMV is the discomfort that the patients experience by wearing the mask [88]. It is possible for patients to feel claustrophobic during the treatment, and between 10% and 20% of the patients do not tolerate NIMV. This aspect demands for the search of alternative therapies [54].

1.2 Nasal High Flow Therapy

Nasal High Flow Therapy serves as an alternative treating method of NIMV, as it is regarded more comfortable than the interfaces used in NIMV [82]. During NHFT, cannulas are inserted into the patient's nostrils, which provide heated, humidified and oxygen-enriched air. The cannula is typically two times smaller than the area of the nostril, leaving a leak between the cannula and the nostril. This leak is crucial, since the airflow supplied during NHFT is often higher than the inspiratory airflow. The leak causes the surplus of air to be able to leave the nose. Since the cannulas are also inserted during expiration, the leak is also needed to exhale via the nostrils. Variables during NHFT are the supplied air rate, cannula size and positioning, the oxygen fraction in the supplied air and the temperature of the supplied air.

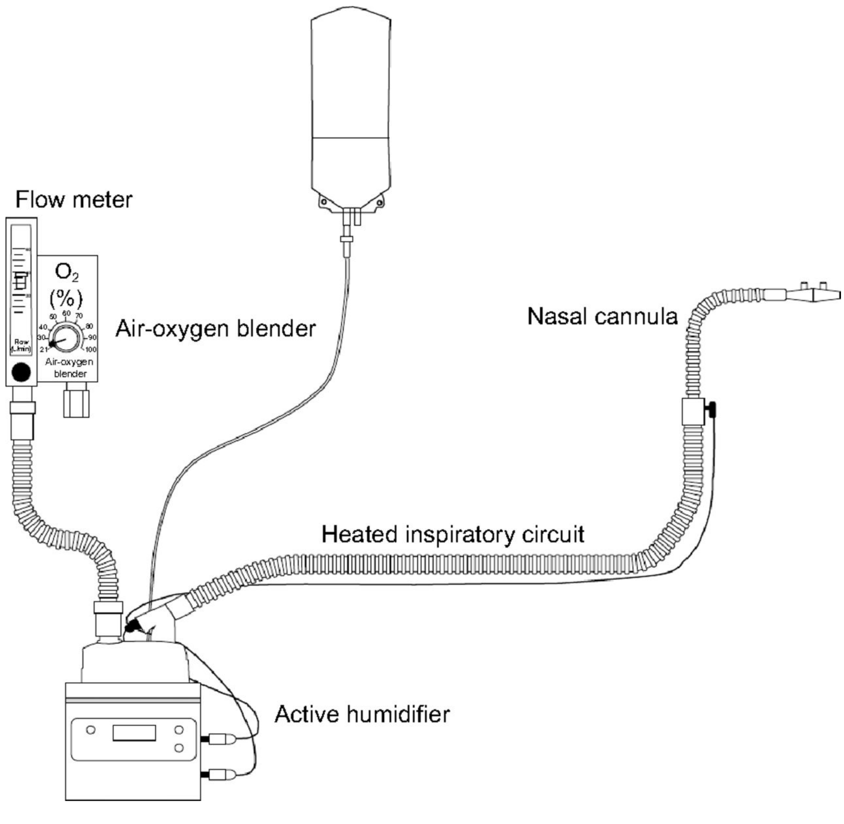

Figure 1.2: Overview of a typical NHFT set-up, ensuring that heated, humidified and oxygen-enriched air leaves the cannulas [70].

An overview of a typical NHFT set-up can be seen in figure 1.2. It consists of a flow generator, active heated humidifier, a heated circuit and the nasal cannulas. The flow generator creates the gas flow which ends up in the cannula. The most popular generators are so called air-oxygen blender systems [70]. Air-oxygen blenders provide a blended pressurized gas at a demanded oxygen concentration. The volume air flow rate is typically within a reach of 10 $\mathrm{L/min}$ to 60 $\mathrm{L/min}$. The gas that flows out of the generator is a dry gas, which can have some negative effects on the patients. Therefore, the air is humidified before it is passed through to the patient. Many humidifiers also heat the air to the desired temperature. Nevertheless, the temperature is also controlled in the inspiratory circuit to prevent the air from cooling down and therefore condensing. By doing so, it is possible to set the exact right temperature, humidification and oxygen concentration of the

air that comes out of the nasal cannula.
Dysart et al. [16] stated five main reasons that contribute to the working mechanism of NHFT. First of all, the washout of dead space in the (naso)pharynx. Dead space is air that is inhaled which does not contribute in the gas exchange at the lungs. The washout of dead space therefore cause higher oxygen concentrations in the airways. Secondly, it is stated that NHFT causes a reduction of inspiratory resistance, therefore reducing the inspiratory work of breathing. It is believed that NHFT reduces this resistance by providing a higher airflow than the patient's peak inspiratory flow. A third point addressed that contributes to the functionality of NHFT is that the therapy uses a humidified and warmed airflow. Dysart et al. [16] mention several studies that show that unheated or dry gas have significant adverse effects on the breathing process. Another point addressed, which elaborates on the third point, is the reduction in energy to condition the air. Normally, a person uses energy to warm the air that comes into the nostrils to reach a body temperature of approximately 37°C. Energy is also used to humidify the air to a 100% relative humidity. This energy is spared by providing air with the desired conditions. Finally, it is believed that NHFT can create continuous positive airway pressure. It is believed that due to this continuous positive distending pressure to the lungs, some ventilatory mechanics are improved. This generated pressure is most likely the highest when the mouth is closed and a fitting cannula size is used.

1.3 Computational methods in Nasal High Flow Therapy

Although there is already a lot of research in NHFT, it is desired to develop guidelines for the use of NHFT [49, 69, 68]. This is however only possible with a better basic understanding of the working mechanisms of NHFT. Physical models are able to measure all sorts of physics, from pressure drop to velocity distributions. The main disadvantage of physical models is the cost of the models and experiments [92].
Another possible method to gain more insight in the physics during NHFT is the use of numerical (computational) models to simulate the flow. It is however important that the simulations are meaningful from a physical standpoint. A literature is therefore needed to compare the results. The most common Computational Fluid Dynamics (CFD) models are based on solving the Navier-Stokes equations by discretization using for example the Finite Volume Method (FVM), the Finite Difference Method (FDM) or the Finite Element Method (FEM). Discretization of the domain is done by splitting the geometry in a large amount of smaller cells, a so called mesh. Creating a mesh can however be very difficult for anatomical geometries, since these geometries are often very complex. Complex geometries require often more cells and require therefore more time and resources, as the computation time is highly dependent on the mesh size. The Lattice Boltzmann Method (LBM) serves as an alternative to the more conventional CFD approaches. The Lattice Boltzmann method is a numerical method that can simulate the flow by solving an modified version of the Boltzmann equation on a lattice. The Lattice Boltzmann Method might be more suitable in simulating the airflow in a complex geometry, when compared to more conventional CFD models(FVM, FEM, FDM), because of two main advantages: The first advantage is that the LBM uses a structured grid, making the process of creating a mesh much faster and easier, especially for complex geometries such as the respiratory tract. Secondly, the LBM is very suitable for parallel computations and therefore efficient to use on more computation cores [77]. The method is therefore suitable for big computations of big geometries that require a high resolution mesh.

1.4 Previous work

In the near past, quite some research is conducted regarding NHFT. This research can be split into numerical research and experimental research, where the latter topic contains both *in vivo* and *in vitro* experiments that often use simplified models. To fully understand the effects of NHFT, it is fundamental to understand the airflow during unassisted breathing. There is quite some knowledge about the anatomy and physiology of the nasal cavities and the upper respiratory tract, both in health and in disease [63]. Early knowledge was obtained from experiments and models, but even as early as 1993 already numerical models were used to study the fluid dynamics in the human larynx and upper airways using a 2D simplified model [53]. More recent studies often show more physical resemblance. The working mechanics and effects of NHFT are less known, and according to Nishimura basic criteria for NHFT are highly wanted [68, 69].

1.4.1 Airflow during unassisted breathing

Doorly et al. [15] provided a critical evaluation of all the issues that are involved in modelling airflow in the human nose, using a long list of relevant studies. It was claimed that an individual perfectly model only provides partial information, due to the variation within the nasal geometry between individual persons. From the literature research performed, it was stated that despite earlier work, there are still some uncertainties in nasal airflow modelling. One of them is the question whether the flow can be modelled as laminar, transitional or turbulent flow. The other one is whether or not the flow can be modelled as a steady process or a series of quasi-steady flows. It was stated that flow instability most likely occurs at flow rates higher than approximately 12 $\mathrm{L/min}$. Banko et al. [3] and Xi et al. [102] studied the airflow without the nasal cavities, but by breathing from the mouth. Banko et al. [3] studied the airflow during inspiration. A 60 $\mathrm{L/min}$ flow rate that corresponds with a Reynolds number of approximately 4200 in the trachea was studied. Vorticity was observed in the trachea, which was generated in the larynx. Xi et al. [102] studied the influence of tidal inspiratory breathing and movement of the glottis in the respiratory tract using both *in vitro* experiments and a numerical model. The study uses a geometry of the mouth extended to the lungs. For the numerical model, Ansys was used, and important differences between steady and transient simulations were observed. Transient simulations (Large Eddy Simulation (LES) model) were able to capture the highly oscillating laryngeal jet that breaks in the tail as well as he multi-scale vortices in the trachea. The steady simulations, using the Reynolds-averaged Navier–Stokes (RANS) $k - \omega$ turbulence model, were not able to show them.

Numerical methods

The study by [102] is not the only numerical study in this scope. A common challenge that arises in simulating flow in the nasal geometry is the inflow prescription at the nostrils. Taylor et al. [92] studied the effect of different inflow boundary conditions by using Ansys Fluent in two different meshes based on two different CT-scans. Five different inflow conditions were investigated; a flat velocity profile, a pre-calculated velocity profile based on an earlier simulation, a convergent pipe inflow up to the nostrils with flat and parabolic inflow conditions and a pressure boundary condition which included the external face. It was stated that flow parameters and behaviour were little affected by the difference in inflow boundary conditions. High sensitivity was however observed for the flow in the region of the olfactory cleft.

Brüning et al. [11] combined the CT-scans of 25 patients to create an average nasal geometry using a statistical shape model. The airflow was then numerically simulated for each patient and compared with the average nasal geometry model. Boundary conditions were applied in such a way that the inhalation and exhalation match with a volume flow rate of 200 $\mathrm{mL/s}$. Despite having a very similar geometry, the average geometry showed quite a difference in the velocity field and maximum velocities when compared to the single geometries. The main reason mentioned is that the the averaging process causes the overall shape to be much more regularized than the patient-specific geometries, therefore being more symmetric and having less protrusions.

Xu et al. [106] conducted a combined experimental and numerical study with a MRI scan model of the human upper airway model using Particle Image Velocimetry (PIV) and Ansys. The model that was created consisted of both the nasal and oral geometry, which were both used as an inlet. The trachea was used as the visualization region in the experiments. Different RANS turbulence models were used in the CFD simulations. Oral, nasal and combined inlet flow was studied with flow rates that correspond to a physical flow rate of 18 $\mathrm{L/min}$, 32 $\mathrm{L/min}$ and 45 $\mathrm{L/min}$. The maximum velocities observed in the experiments were in the vicinity of two times the inlet velocity due to glottal jet flow. This phenomena is often described in the literature: due to the shape of the respiratory tract and the narrowing of the cross section at the glottis, the flow field velocities increase when passing the glottis. During inhalation, it can be seen that the flow jet enters the trachea at a certain angle [106]. The glottal (or laryngeal) jet can also cause flow separation near the glottis. The maximum velocities observed during exhalation were smaller than during inhalation. It was observed that the different RANS turbulence models showed significant deviation with respect to each other as well as to the experiment. Another study that used CFD to map the airflow in the respiratory tract is conducted by Zuber et al. [112]. The study used a RANS turbulence model and steady-state simulations on several flow rates. A maximum velocity of 4.2 $\mathrm{m/s}$ was observed in the nasal valve at a flow rate of 20 $\mathrm{L/min}$

There are a few known cases that use the Lattice Boltzmann method to simulate airflow in the nasal geometry. Lintermann et al. [47] used the Lattice Boltzmann method to study steady inhalation in three different nasal cavities. It is a very complete study, which study all kind of local fluid behaviour such as recirculation and vorticity by using PSD functions, streamlines and more. Flow rate with a steady inflow of 15 $\mathrm{L/min}$ flow was simulated. Mesh sizes used for the three geometries consist of 135M cells, 93M cells and 113M cells. A finer mesh was also investigated with 724M cells, which showed no extreme differences in results with the coarser meshes.

Finck et al. [20] used the LBM-BGK model with an additional damping factor in the viscosity term, similar to what happens in LES simulations, to model steady laminar flow of air through a model configuration of a nasal cavity. The model that was used was previously used by Hörschler et al. [32], who used a FVM to simulate the flow. The Reynolds number at the throat were set to be 790 during inspiration and 1000 during expiration. The LBM simulations have a grid size of 5M cells which is locally refined. The simulations in the FVM used 10 times as less cells. The results of the two simulation methods were in good agreement.

Zwicker et al. [114] used the Lattice Boltzmann method on three different geometries with a steady expiration flow. The goal of this research was however to present a validated protocol to reconstruct geometries of nasal cavities. A mesh with a grid spacing of 0.25 mm was used. Inflow with a constant flow rate of 1.5 $\mathrm{L/min}$ was prescribed.

1.4.2 Nasal High Flow Therapy

Studies regarding Nasal High Flow Therapy are present in literature using numerical methods as well as *in vitro* and *in vivo* experiments.

Positive end-expiratory pressure
Several studies of the working mechanics of Nasal High Flow Therapy show a positive relation between the flow rate of the NHFT and positive end-expiratory pressure (PEEP) [50, 59, 60, 73]. Parke et al. [73] found a linear relation between the pharyngeal pressure and the airflow rate. It was also noted that this pressure is higher with mouth closed than with mouth open. The increase in pressure is believed to be caused by the increase in exhalation resistance. The increase in pharyngeal pressure was also noted by Mundel et al. [62], who studied the ventilation of 10 different test subjects during NHFT both in wakefulness and sleep. The Airflow rates used were 15 $\mathrm{L/min}$, 30 $\mathrm{L/min}$ and 45 $\mathrm{L/min}$. It was noticed that pharyngeal pressure increased with NHFT with 0.5 to 1 cmH_2O per 10 $\mathrm{L/min}$ airflow supplied from the cannulas.

Moore et al. [59, 60] studied the influence of the gas type and flow rate on the airway pressure and CO_2 clearance using an accurate acrylic plastic 3D model of the upper respiratory tract with closed mouth of five different adults, connected to a lung simulator at the trachea. The airflow was provided with flow rates of 0, 15, 30 and 60 $\mathrm{L/min}$. It was concluded that the inhaled CO_2 factor is mainly influenced by the cannula flow rate. Geometry influences are present, but hard to quantify by geometrical parameters such as airway volume and surface area. A quadratic relationship between NHFT flow rate and PEEP was found.

Luo et al. [50] studied the PEEP with three different cannula devices, and found similar results. It was mentioned that breathing with open or closed mouth and the provided flow rate from the cannula are two of the main key factors in the increase of PEEP. The lung compliance was believed to be the third key factor. Nielsen et al. [67] elaborated on the studies in PEEP by using 3D models of babies, toddlers and adults. It was observed that all models had a change point: a certain amount of airflow rate after which a non-linear positive PEEP relation was experienced. The needed airflow to obtain a certain pressure was higher with the age of person, as well as the change point.

Visualization
Several methods were used to visualize the effects of Nasal High Flow Therapy. Spence et al. [87] used stereoscopic particle image velocimetry (SPIV) to measure the three-dimensional flow fields during NHFT and unassisted breathing. A scaled flow phantom of the nasal cavity was used which was obtained from a CT-scan. Fully developed flow was used as an inlet in the cannulas. It was concluded that NHFT has a significant effect on the flow velocity magnitude and distribution in the nasal cavity. Another important subject which is often being investigated is the wash-out of the death space. Möller et al. [57] studied the wash-out of death space using two simplified upper airway models and radioactive krypton gamma tracer gas with camera imaging in 2015. It was concluded that NHFT helps clearing the death space in the models. In 2017, Möller et al. [58] used a similar method on healthy volunteers. The research was limited due to the method used to only take into account the clearance during breath holding. In the second part of the study, three people with a tracheotomy volunteered. The ventilation parameters, peripheral capillary oxygen saturation and tissue CO_2 were investigated in the patients. It was concluded that the clearance in dead space was related to NHFT rate and time. Adams et al. [1] studied the effects on upper airway resistance during NHFT. A 3D-printed model was used based on a CT-scan. The pressure drop between the trachea and nostrils and the flow rate were measured to estimate the resistance in the airways. It was concluded that NHFT increases resistance during exhalation. It was noted that if respiratory rate and minute volume are reduced by NHFT, the work required to surpass the resistance is lower.

Numerical methods
Kumar et al. [43] were the first to use numerical methods to model NHFT. A simplified 'minimal' geometry was used, which was obtained by simplifying the cross-sections of the real nasal geometry. The impact of the geometry differences were studied by using three different nostril areas and three different nasal valve areas. Steady state flow was considered with at each nostril the same inlet flow rate. It was clear that the study showed quite some limitations, despite that an insight of the flow was given as well as some insights in the PEEP.
A very detailed and insightful numerical and experimental study with respect to NHFT was conducted by Van Hove et al. [31]. The same model, obtained from a CT scan, was used in both a numerical study in Ansys as well as in the experimental study. Cannulas were used with a clinical orientation and were inserted approximately 74% in the nostrils. Flow was modelled as a mixture of CO_2 and humidified air. The turbulence model used was the $k-\omega$ SST model. The experimental model was 3D-printed. Pressure was measured at 4 different points in the geometry. It was observed that the cannula orientation has a significant influence on the pressure, as changing the angle by $15°$ causes a change of pressure of 10%.

1.5 Research Question

A limitation in respiratory studies is the use of rigid, mucous free and cilia free models. Fodil et al. [21] used simplified models to study the difference between a compliant and rigid model and stated that the difference in resistance in the nose is less than 20% if the pressure drop is less than $3\mathrm{cmH_2O}$. During NHFT, the pressure drop might surpass this pressure drop for higher flow rates. Doorly et al. [15] conducted several studies regarding human airflow and stated that direct comparisons of numerical simulations with experiments of the the same geometry are rare in the respiratory tract. Nishimura [69] stated in 2015 that the working mechanics and effects of NHFT are less known and basic criteria for NHFT are highly wanted. Haq et al. [27] showed an overview of several studies performed (up till 2014) regarding NHFT in infants. A research direction stated was the need for good quality studies of the airway flow to measure distending pressures generated by NHFT which includes the influences by factors such as mouth position, flow rate, relative nasal cannula size, patients age and weight and the type of respiratory pathology. In this way, by gaining more data, it might be possible to develop guidelines in the clinical application of NHFT. Recent studies show more insights into the working mechanics, but there are not enough studies to accurately quantify and compare this. One of the reasons is the variation in the nasal geometry between persons. It is believed that the geometry has influence on the wash-out effect, and a statistical analysis of the airway geometry is wanted [31]. Using an averaged geometry for modelling respiratory airflow turns out to be unhelpful [11]. Studying the effects of NHFT on different geometries can therefore add to understand the working mechanics and finding optimal patient settings.

The main research question that will be tried to answer during this thesis is:

How can Nasal High Flow Therapy be modelled using the Lattice Boltzmann method to help understanding the working mechanics and finding optimal patient settings of Nasal High Flow Therapy?

To help answer this research question, sub-questions have been drafted:

- *How does the Lattice Boltzmann method compare with more conventional CFD methods?*
- *What are the influences of the Lattice Boltzmann parameters?*
- *What are the limitations of the Lattice Boltzmann method in the scope of this research?*
- *How can unassisted breathing be modelled using the Lattice Boltzmann method?*

This research will not focus on the influence of a rigid model, but on the use of a new geometry with good quality simulations (either Large Eddy Simulations (LES) or Direct Numerical Simulations (DNS)). The Lattice Boltzmann method is very suitable for creating high quality simulations since it is very suitable for parallel computation and is therefore able to use an expensive turbulence model or DNS on a high resolution grid. Also transient simulations will be performed with a realistic breathing profile. On top of that, the research conducted is parallel to an experimental research that uses the same geometry, making it therefore possible to directly compare the results.

1.6 Thesis outline

The thesis consists of a main part and an appendix. In chapter 2, the theory of the Lattice Boltzmann method is described. The code that is used for the simulations is also highlighted. In chapter 3, a benchmark study of a 2D flow around a cylinder is simulated using the Lattice Boltzmann method and compared with results from literature and Ansys Fluent. Code performance and the influence of the relaxation time are also shortly briefed. A more complex case, that of a femoral artery bifurcation, is studied and compared with simulations performed in SimVascular, which uses the Finite Element Method, in chapter 4. Chapter 5 describes the main case of this thesis, that of the nasal airflow. The experimental set-up will also be briefly discussed in this chapter. The simulation results are presented and discussed in chapter 6. An overview of the challenges that come with simulating NHFT using LBM is discussed in chapter 7. Limitations of the research, recommendations and research directions for future research are stated in chapter 8. The conclusion of the research is stated in chapter 9. The appendix is mainly used to provide extra visualization via images and some extra explanation on less important subjects.
Figures, tables, sections and chapters that start with a letter are in the appendix. Tables and figures that are not in the appendix start with the number of the chapter it is in, followed by a dot and the cardinal numeral of the figure or table in that chapter. Mathematical letters that are bold indicate that it is a vector.

2 | Theory

2.1 The Boltzmann equation

The Boltzmann equation (or Boltzmann transport equation) is named after the Austrian physicist Ludwig Boltzmann. The basic concept of Boltzmann's work is that is it possible to describe interacting particles that are not in equilibrium by using a statistical viewpoint that takes the huge number of particles into account.
This means that the Boltzmann equation does not consider the position and momenta of each single particle, but it considers the chance that a particle has a certain position and velocity using a probability distribution function. It is proven that even though using simple mechanical laws, the Boltzmann equation can accurately describe fluid flows [90].

The Boltzmann equation describes the probability density function in the phase space. The phase space is the space of both the positions of all the particles (physical or configuration space) in the system and their velocities (momentum space). This means that it is six dimensional, containing three position components and three momentum components. It is possible to describe a distribution function:

$$f(\mathbf{x}, \mathbf{p}, t) \tag{2.1}$$

Consider a particle at a certain position $\mathbf{x}$ with momentum $\mathbf{p}$ at time t. The new position and momentum at $t + dt$ are then given by $\mathbf{x} + d\mathbf{x}$ and $\mathbf{p} + d\mathbf{p}$ respectively. This part of the Boltzmann equation is called the streaming process. It is however possible for particles to collide, who therefore either start at $(\mathbf{x}, \mathbf{p})$ but do not arrive at $(\mathbf{x} + d\mathbf{x}, \mathbf{p} + d\mathbf{p})$ or do arrive at $(\mathbf{x} + d\mathbf{x}, \mathbf{p} + d\mathbf{p})$ but not start at $(\mathbf{x}, \mathbf{p})$. The collision causes therefore a source term Γ in the Boltzmann equation, giving the total expression for the first order distribution over time as:

$$f(\mathbf{x} + d\mathbf{x}, \mathbf{p} + d\mathbf{p}, t + dt)d\mathbf{x}d\mathbf{p} = f(\mathbf{x}, \mathbf{p}, t)d\mathbf{x}d\mathbf{p} + \Gamma d\mathbf{x}d\mathbf{p}dt \tag{2.2}$$

Dividing by $d\mathbf{x}d\mathbf{p}$ and taking the first order Taylor series of the left hand side gives:

$$\begin{aligned} f(\mathbf{x} + d\mathbf{x}, \mathbf{p} + d\mathbf{p}, t + dt) \approx & f(\mathbf{x}, \mathbf{p}, t) + \frac{\partial f(\mathbf{x}, \mathbf{p}, t)}{\partial \mathbf{x}} \cdot (\mathbf{x} + d\mathbf{x} - \mathbf{x}) + ... \\ & \frac{\partial f(\mathbf{x}, \mathbf{p}, t)}{\partial \mathbf{p}} \cdot (\mathbf{p} + d\mathbf{p} - \mathbf{p}) + \frac{\partial f(\mathbf{x}, \mathbf{p}, t)}{\partial t} \cdot (t + dt - t) \end{aligned} \tag{2.3}$$

With the collision term and rewriting this becomes

$$\frac{\partial f(\mathbf{x}, \mathbf{p}, t)}{\partial \mathbf{x}} d\mathbf{x} + \frac{\partial f(\mathbf{x}, \mathbf{p}, t)}{\partial \mathbf{p}} d\mathbf{p} + \frac{\partial f(\mathbf{x}, \mathbf{p}, t)}{\partial t} dt = \Gamma dt \tag{2.4}$$

Dividing by dt gives the Boltzmann equation:

$$\frac{\partial f}{\partial t} + \frac{d\mathbf{x}}{dt} \cdot \frac{\partial f}{\partial \mathbf{x}} + \frac{d\mathbf{p}}{dt} \cdot \frac{\partial f}{\partial \mathbf{p}} = \Gamma \tag{2.5}$$

This equation is often rewritten to another form by using Newton's second law $\frac{d\mathbf{x}}{dt} = \frac{\mathbf{p}}{m}$ and $\frac{d\mathbf{p}}{dt} = \frac{d\mathbf{u}}{dt} \cdot m = \mathbf{F}$

$$\frac{\partial f}{\partial t} + \frac{\mathbf{p}}{m} \cdot \frac{\partial f}{\partial \mathbf{x}} + \mathbf{F} \cdot \frac{\partial f}{\partial \mathbf{p}} = \Gamma \tag{2.6}$$

This still uses a unknown source term Γ to take the collisions into account. When the collision operator is written more explicitly, the Boltzmann equation becomes a nonlinear integral differential equation [86]. Solving the equation is therefore very difficult, and attempts have been made to simplify the collision term by Chapman - Enskog expansion. It can be shown that, without the collision term, the Boltzmann equations can be rewritten to conservation equations by assuming local equilibrium. The Chapman - Enskog theory obtains the Euler equations with dissipation terms by expressing some deviation from the local equilibrium. By using the first order Chapman - Enskog expansion, the Navier-Stokes equations can be obtained. The second order expansion gives the Burnett equations and the third order give the super Burnett equations. The derivation is regarded beyond the scope of this master thesis, but some knowledge of this method is needed in upcoming sections of this thesis.

2.2 Lattice Gas Cellular Automata

The transition from the Boltzmann equations to the Lattice Boltzmann equations can be explained in various ways. It is possible to discretize the Boltzmann equations, and by using the Chapman - Enskog theory one can obtain the Lattice Boltzmann method. However, another more intuitive way to explain the Lattice Boltzmann method is to start with the Lattice Gas Cellular Automaton model, since these models were the forerunners of the Lattice Boltzmann method. A cellular automaton is an algorithm that, in general, examines its own state and the state of some numbers of its neighbouring cells to obtain its next state at the next time step. The next state is often determined by a simple rule [90]. Imposing an initial condition and boundary conditions on the cells combining with the evolution rules will therefore uniquely determine the cellular evolution in time.
This concept can best be understood when looking at a simple version. Consider a one dimensional line with cells that can either be state 0 or state 1 and base their state with their left and right direct neighbour. The state of a cell s_i can then be determined by:

$$s_{i,t+1} = \Phi(s_{i-1,t}, s_{i,t}, s_{i+1,t}) \tag{2.7}$$

with Φ the update function and t a given time step. When considering the states of a cell s_i and their two neighbours, there are 8 different possible states. Since the new state is either 0 or 1, there are $2^8 = 256$ possible update functions. These update functions can be described using binary numbers, which is explained in appendix A.

2.2.1 Lattice Gas Cellular Automata in fluid flows

Despite its simplistic nature, Lattice Gas Cellular Automata can be used to describe fluid flows. Frish, Hasslacher and Pomeau provided a 2D Lattice Gas Model that can solve the Navier-Stokes equations of fluid motion, which is often referred to as the FHP model [22]. The FHP model is an equilateral triangular lattice model, where the lattice points are separated by 1 lattice unit (lu) and the velocity of all particles are identical with 1 lattice unit per time step (lu/ts). Due to its triangular model, there are 6 lines connecting each node. This means that there are six possible directions of the particles moving. The unit velocity vectors are defined as $\mathbf{e_i} = (cos(\pi i/3), sin(\pi i/3))$. The subscripts for i at a node can be seen in figure 2.1. Similar to the Boltzmann equation, the time evolution is determined by a streaming process and a collision process. At the collision process, conservation of mass and momentum should be satisfied. Since all particles have the same mass and velocity, the momentum conservation can be simplified to the vector sum of the velocities. The collision rules must be described in such a way that the momentum before and after collision does not change, which gives the only possible collisions as in figure 2.2. Notice that the head on head collision with two particles can give two different post-collision options. It is therefore needed to choose randomly between both post-collision options, causing a great deal of noise into the simulations. This noise is needed for the model to be able to simulate hydrodynamics, but requires temporal and/or spatial averaging to obtain smooth fluid flows [90].

2.3 Lattice Boltzmann Method

It is possible to use the same methods as in the Lattice Gas Cellular Automata at the Boltzmann equations, giving the Lattice Boltzmann model. The Lattice Boltzmann model simplifies the Boltzmann equation by confining the particle positions to the nodes of the lattice, therefore reducing the number of possible particle spatial positions. Several models are possible as long as it obeys rotational symmetry, but the D2Q9 (two dimensional with nine possible velocity vectors) is discussed here. A schematic overview of the D2Q9 model can be seen figure 2.3.
Particle mass is regarded uniform (1 mass unit). The velocity magnitude (lattice velocity) is often chosen to be $1\mathrm{lu/ts}$ for $\mathbf{e_1}...\mathbf{e_4}$ and therefore by Pythagoras's theorem $\sqrt{2}\mathrm{lu/ts}$ for $\mathbf{e_5}...\mathbf{e_8}$. The distribution f_i is now confined to the possible particle directions and represents the direction specific probability density function, a kind of rate of occurrence.

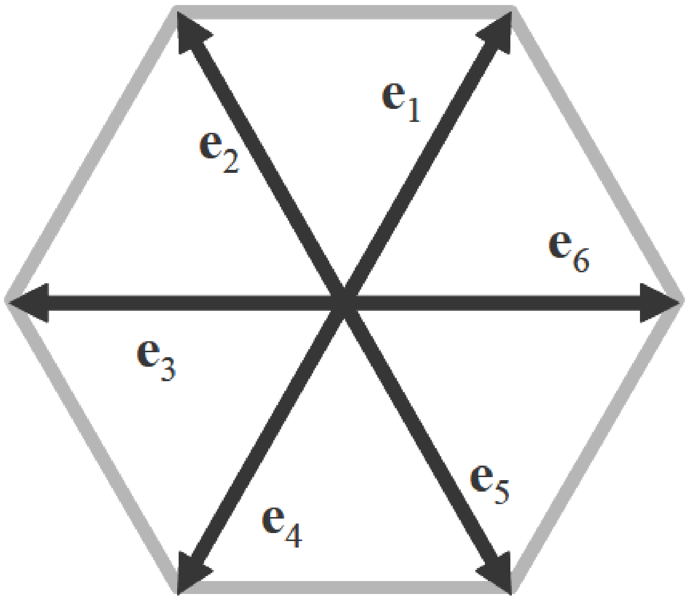

Figure 2.1: The unit velocity vectors of the FHP model [90].

The macroscopic density can be given as:

$$\rho = \sum_{i=0}^{8} f_i \tag{2.8}$$

The dimensionless macroscopic velocity is given as the average of the microscopic velocities with their directional density as a weight factor, following from the momentum density relation:

$$\mathbf{u} = \frac{1}{\rho} \sum_{i=0}^{8} f_i \mathbf{e_i} \tag{2.9}$$

As mentioned in section 2.1, the collision term can be simplified by regarding a deviation from the local equilibrium.
In similar manner, the collision term can be simplified in the Lattice Boltzmann method by the Bhatnagar, Gross and Krook (BGK) single relaxation method [7, 89]. The basic form of Lattice Boltzmann can be given as:

$$f_i(\mathbf{x} + \mathbf{e_i}\Delta t, t + \Delta t) = f_i(\mathbf{x}, t) + \Omega_{ij} \tag{2.10}$$

Which can be interpreted as a discretized version of equation 2.2, or, the Boltzmann equation discretized in velocity space, physical space, and time space [41]. The streaming part is given by $f_i(\mathbf{x} + \mathbf{e_i}\Delta t, t + \Delta t) = f_i(\mathbf{x}, t)$ while the collision operator is given by Ω_{ij}.
The exact derivation of the BGK method is regarded beyond the scope of this thesis, but the main steps are discussed here. First a deviation from equilibrium is introduced by Chapman-Enskog expansion (function parameters are left out for clarity):

$$f_i = f_i^{eq} + f_i^{neq} = f_i^{eq} + \epsilon f_i^{(1)} + \epsilon^2 f_i^{(2)} + ... \tag{2.11}$$

In this equation, $f_i^{eq}(\mathbf{x}, t)$ (also often notated as $f_i^0(\mathbf{x}, t)$) is the local equilibrium function and ϵ is a dimensional representative of the Knudsen number [41, 97]. By performing the second order Taylor series on the collision operator and performing the expansion on the equilibrium function, the linearized collision operator can be written as the multiplication of a collision matrix and the deviation from equilibrium in the distribution function. This can be simplified even more by assuming one dominant eigenvalue τ in the collision matrix, giving the new relation for Ω_i [101]:

$$\Omega_{ij} = -\frac{f_i(\mathbf{x}, t) - f_i^{eq}(\mathbf{x}, t)}{\tau} \tag{2.12}$$

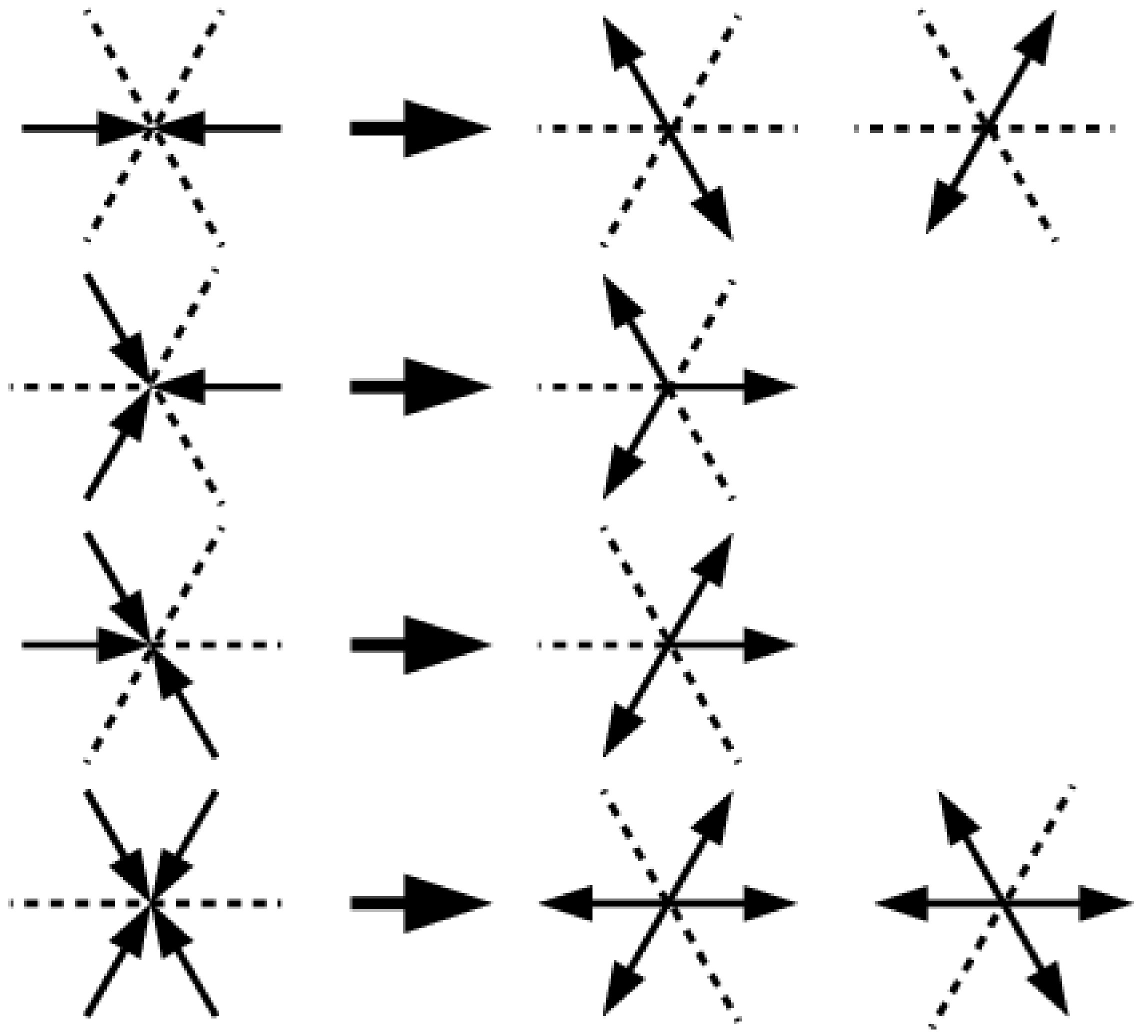

Figure 2.2: The collision rules of the FHP Lattice Gas Cellular Automata [38]. The original FHP model only considers 2 and 3 particle collisions.

Applying the BGK method, the Lattice Boltzmann equation becomes:

$$f_i(\mathbf{x} + \mathbf{e_i}\Delta t, t + \Delta t) = f_i(\mathbf{x}, t) - \frac{f_i(\mathbf{x}, t) - f_i^{eq}(\mathbf{x}, t)}{\tau} \tag{2.13}$$

With the parameter τ defined as the (non-dimensional) relaxation time. The exact derivation is beyond the scope of this thesis, but the equilibrium distribution function f_{eq} is obtained by Chapman - Enskog expansion and by approximating a form of the Maxwellian distribution with constant-temperature and a low Mach number [71]. The derived Maxwellian-distribution function is then approximated by second order Taylor series and is given in the BGK method is given as:

$$f_i^{eq}(\mathbf{x}) = w_i \rho(\mathbf{x}) \left(1 + \frac{3\mathbf{e_i} \cdot \mathbf{u}}{c_s^2} + \frac{9}{2}\frac{(\mathbf{e_i} \cdot \mathbf{u})^2}{c_s^4} - \frac{3\mathbf{u}^2}{2c_s^2}\right) + \mathcal{O}\left(\mathbf{u}^3\right) \tag{2.14}$$

with w the weighting factor, which is $4/9$ for $a = 0$, $1/9$ for $a = 1...4$ and $1/36$ for $a = 5...8$ for a D2Q9 lattice. The total weight of the weighting factors should equal 1 for all stencils. Other parameters are the macroscopic velocity $\mathbf{u}$ and the speed of sound on the lattice c_s . Note that this is not the physical speed of sound, but rather some pseudo compressibility parameter that allows relaxation to the incompressible viscous solution [71]. Both the weight factors and the speed of sound are dependent on the type of lattice used, but it is calculated by ensuring that the Chapman - Enskog expansion recover mass conservation, momentum conservation and a viscous stress tensor [56, 71]. For the D2Q9 and D3Q15 models, the speed of sound is given as $\frac{1}{\sqrt{3}}$. The equilibrium function reduces to the weights times the fluid density if the macroscopic velocity is 0. The equilibrium distribution function uses the macroscopic velocity in the new state.

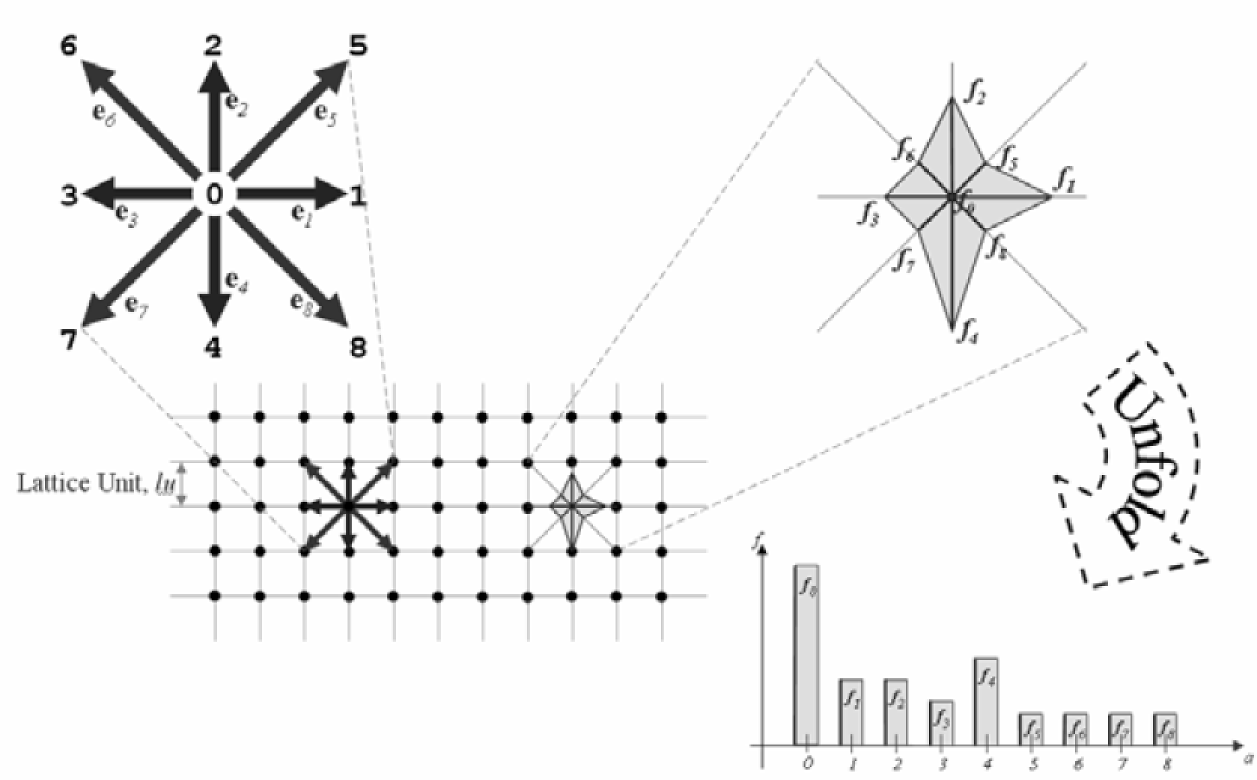

Figure 2.3: Schematic overview of the D2Q9 model, with the probability density function [90].

When there are zero forces, the velocity in new state is equal to the velocity in the old state. When there are external forces, the velocity in the new state is calculated by using Newton's second law:

$$\mathbf{F} = m\frac{d\mathbf{u}}{dt} \tag{2.15}$$

This can be rewritten in terms of the mass density. Note that in LBM, not the actual force is needed but the force density. The force density is proportional to the mass and by using the relaxation time as the characteristic time [41, 90]:

$$\Delta u = \frac{\tau \mathbf{F}_\rho}{\rho} \tag{2.16}$$

Using this relation, the new state velocity is given as:

$$\mathbf{u_{eq}} = \mathbf{u} + \Delta\mathbf{u} = \mathbf{u} + \frac{\tau \mathbf{F}_\rho}{\rho} \tag{2.17}$$

With the BGK model, the new lattice state is calculated in two steps, first the collision step and then the streaming step [107].

$$\widetilde{f}_i(\mathbf{x}, t+\Delta t) = (1-\frac{1}{\tau})f_i(\mathbf{x}, t) + \frac{f_i^{\text{eq}}(\mathbf{x}, t)}{\tau} \qquad \textbf{Collosion} \tag{2.18}$$

$$f_i\left(\mathbf{x} + \mathbf{e}_i\Delta t, t+\Delta t\right) = \widetilde{f}_i(\mathbf{x}, t+\Delta t) \qquad \textbf{Streaming} \tag{2.19}$$

Where $\widetilde{f}_i$ denotes the particle density distribution function in the post collision state.

2.3.1 Lattice parameters

To convert a problem in lattice parameters, a unit conversion is needed between lattice units and the physical units. In the (Lattice) Boltzmann equations, the density distribution functions f_i and the relaxation parameter τ are non-dimensional and do therefore need no conversion. However, since the Lattice Boltzmann should represent an actual physical system, the choice of lattice variables is important [44]. One should always ensure that the non-dimensional parameters in the

physical world and on the lattice are the same.
It is often chosen that the lattice velocity C is 1 lu/ts in lattice units. Meaning that a particle can move to one neighbouring node in one time step.

$$C \equiv \frac{h}{\Delta t} \equiv \frac{\Delta x}{\Delta t} \tag{2.20}$$

With Δx or h the grid spacing in meters and Δt the time step in seconds in physical units, or lu and ts in lattice units. The relation between the physical fluid velocity and the lattice fluid velocity is then given by:

$$v_{lat} = v_{phy}\frac{\Delta t}{\Delta x} = \frac{v_{phy}}{C} \tag{2.21}$$

The lattice density is defined by:

$$\rho_{lat} = \frac{\rho}{\rho_0} \tag{2.22}$$

with ρ_0 the 'true fluid density'. The lattice density value will be very close to unity, but can differ slightly since incompressibility is not satisfied exactly in the Lattice Boltzmann model: $\rho = \rho_0 + \mathcal{O}\left(\mathrm{Ma}^2\right)$ [13, 19].
The physical speed of sound in isotropic conditions is described as:

$$c = \sqrt{\left(\frac{\delta p}{\delta \rho}\right)_s} \tag{2.23}$$

This equation of state relates the pressure and the density with the speed of sound in Lattice Boltzmann:

$$P = c_s^2 \rho \tag{2.24}$$

This can be seen as having the physical equation of state with the heat capacity ratio $\gamma = 1$ [97]. The lattice speed of sound is related to the lattice velocity dependent on the model, but for the most common D2Q9 and D2Q15 models, the isothermal relation is given by

$$c_s = \frac{C}{\sqrt{3}} \tag{2.25}$$

The lattice viscosity is directly related with the relaxation time:

$$\nu_{lat} = c_s^2\left(\tau - \frac{1}{2}\right) = \frac{\tau - \frac{1}{2}}{3} \tag{2.26}$$

The physical viscosity is obtained by scaling the lattice viscosity:

$$\nu = c_s^2\left(\tau - \frac{1}{2}\right)\Delta t = \frac{\left(\tau - \frac{1}{2}\right)}{3}\frac{\Delta x^2}{\Delta t} \tag{2.27}$$

If LES turbulence model is implemented, the viscosity therm is extended with a turbulent viscosity term [75, 85, 103]:

$$\nu^* = \nu + \nu_T \tag{2.28}$$

Where the turbulent viscosity ν_T is defined according to the Smagorinsky–Lilly model as:

$$\nu_T = \left(C_s \Delta_g\right)^2 \sqrt{2\mathbf{S_{ij}}\mathbf{S_{ij}}} \tag{2.29}$$

With C_s the model coefficient, Δ_g the characteristic length (taken as the cube root of the cell its volume) and $\mathbf{S_{ij}}$ the rate-of-strain tensor in $(1/\mathrm{s})$ defined as:

$$\mathbf{S_{ij}} = \frac{1}{2}\left(\frac{\partial \mathbf{u_i}}{\partial \mathbf{x_j}} + \frac{\partial \mathbf{u_j}}{\partial \mathbf{x_i}}\right) \tag{2.30}$$

The rate-of-strain tensor can be calculated using a finite difference scheme or directly via the distribution functions [19, 75, 85]. The latter option is extremely valuable, since it does not change the Lattice Boltzmann equation self, but only changes the viscosity term [19]. Note that, even for laminar flow, if the velocity gradient is non zero, the turbulent viscosity term ν_T is bigger than 0.

2.3.2 Choosing the parameters

Choosing the lattice parameters is not trivial and can cause inaccuracies or instabilities if chosen wrong. Therefore some parameter ranges and relations are discussed in this section.
The Lattice Boltzmann method represent the second order Navier-Stokes equations for low (lattice) Mach numbers, where the lattice Mach number is given as the fraction between the macroscopic fluid velocity and the lattice velocity:

$$\mathrm{Ma} = \frac{v_{max}}{C} << 1 \tag{2.31}$$

Note that this equation reduces to the velocity in lattice units and should give the same value in physical and lattice units. Due to the origin of the linearized BGK model, where low Mach numbers were assumed, the Mach number should be far less than 1 to obtain accurate results. The upper limit of the Mach number should ideally be 0.1 [19]. In any case it should satisfy incompressible flow, giving that $Ma < 0.3$. It can be shown that the convergence of the incompressible Navier-Stokes equations are of $\mathcal{O}\left(Ma^2\right)$. This is due to the fact that Lattice Boltzmann is a quasi-compressible solver. When solving the pressure equation it enters a small compressible regime where compressibility effects impact the numerical accuracy [19, 26, 44, 56]. Since the Mach number is directly related to $\sim \frac{\Delta t}{\Delta x}$, the compressibility error is in $\mathcal{O}\left(\frac{\Delta t^2}{\Delta x^2}\right)$.
The error of the Lattice Boltzmann method are in order $\mathcal{O}\left(\Delta x^2\right)$ since it is second order accurate [44]. To increase the accuracy by reducing the grid spacing h (or Δx), the error will only reduce if the compressibility error does not take over the order of error. By this reasoning, the time step size should be scaled according to:

$$\Delta t \sim \Delta x^2 \tag{2.32}$$

This is called **diffusive scaling**. Another constraint turns up when looking at the relaxation parameter τ. It can be seen from equation 2.26 that τ is needed to be larger than 0.5 to obtain a positive viscosity. In general, a relaxation parameter larger than 1 describes an overrelaxation, while choosing a $\tau < 1$ would described underrelaxation. At all times an under-relaxated case should be chosen with $\frac{1}{2} < \tau < 1$. A large value for τ represents a more stable solution since the flow is more viscous. A small value for τ is less viscous and therefore easier the subject of numerical instabilities [19, 45]. Therefore, the relaxation coefficient can affect the numerical stability in the vicinity of $\tau \to \frac{1}{2}$. At very low relaxation parameters, the distribution functions decay very slowly to the equilibrium. This happens in a oscillatory manner. Due to these oscillations combined with the streaming of the particles, the value of $f_i(\mathbf{x}, t)$ can differ so much from its equilibrium that it can become negative. When several of these effect occur and are streamed into the same node, a very small or negative density can arise which explodes the simulation [97].
Using the constraints mentioned for $\Delta t, \tau$ and the Mach number, one possible method for obtaining the lattice parameters can be constructed as follows. First a grid spacing size h is chosen. Then a value for the relaxation time τ is chosen within its limits. By using equation 2.26 the lattice viscosity can be calculated. By rewriting 2.27, the time step size can be obtained:

$$\Delta t = \frac{\nu_{lat} h^2}{\nu_{phy}} \tag{2.33}$$

This relation satisfies the relation in equation 2.32. Finally, since h and Δt are known, the Mach number can be calculated as in equation 5.3. If the Mach number turns out to be too big to obtain accurate results, either h or τ should be chosen smaller.

2.3.3 Boundary conditions

Boundary conditions in Lattice Boltzmann simulations are a little bit different than boundary conditions in the more common CFD methods, and there are many different possibilities in implementing the boundary conditions. When trying to solve the Navier-Stokes equations, the task is to find consistent Lattice Boltzmann boundary equations that correspond to the macroscopic boundary conditions such as no-slip condition or normal stress condition. A common problem is that the Lattice Boltzmann boundary conditions require more information than the Navier-Stokes equations. The additional conditions have to be chosen keeping in mind that they do not conflict with the boundary conditions of the Navier-Stokes in macroscopic level [39]. Often the macroscopic properties are known at the boundary, but the distribution functions are not. Since there are many ways of implementing the boundary conditions in Lattice Boltzmann, only the most important boundary conditions and the ones that will be used in this thesis will be discussed in this section.

Bounce-back boundary conditions

One of the more simpler boundary conditions is the bounce-back boundary condition, which satisfies the no-slip condition [10]. In the bounce-back boundary condition, the densities are temporarily stored inside the solid elements and enter the

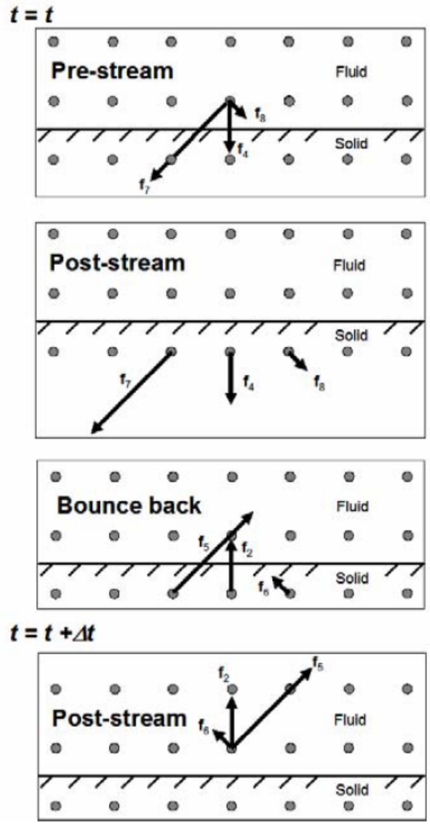

Figure 2.4: Representation of the bounce-back boundary condition, with a mid plane wall [90].

domain in the next time step or two time steps later for respectively half-way bounce-back and a full bounce-back method [41, 90]. This is represented in figure 2.4. The reflection of the particles guarantees that both tangential and normal components of the wall fluid velocity disappear, hence a no-slip condition.
Although the bounce-back boundary condition can provide good results, there is another trick that can increase the efficiency without refining the elements at the boundary, which is called linear wall interpolation and proposed by Bouzidi et al. [10] A representation of the linear wall interpolation can be seen in figure 2.5. The fluid node closest to the wall is A and the first solid node is B. Let q be the position of the wall, which is defined as $q = \frac{AC}{AB}$. Two different situations can be distinguished, $q < \frac{1}{2}$ and $q \geq \frac{1}{2}$. When the fluid particle leaves A and bounces back on the wall, it will not reach another fluid node when the lattice velocity is 1. In the case of the figure, this means that the density at A for particles with a velocity of -1 is unknown. By interpolating , it is possible to estimate the unknown quantities at A. Linear wall interpolation introduces the ghost node D. If $q < \frac{1}{2}$, it is possible to estimate the properties at A by examining the fluid properties at D which bounce back to A. If $q \geq \frac{1}{2}$, the situations in the nodes E and F and the properties of the fluid at D will be used to estimate the properties at A.

On Von Neumann and Dirichlet boundaries

Von Neumann boundaries are boundaries in which a flux is described, such as a velocity inlet boundary. Prescribing the boundary condition in Lattice Boltzmann is less straightforward than one might think. The macroscopic density and velocity at the boundaries are described by equations 2.8 and 2.9. These can be regarded as the summation over the individual directions. For this example a D2Q9 stencil is taken with a velocity boundary at a horizontal plane, given as:

$$\mathbf{u}_o = \begin{bmatrix} 0 \\ -v_0 \end{bmatrix} \tag{2.34}$$

A schematic overview can be seen in figure 2.6. The particle densities in the directions 4, 7 and 8 are unknown, as well as the macroscopic density/pressure. This means that four equations are needed. The macroscopic velocity equation 2.9 provides an equation in each dimension. This means that in 2D two more equations are needed. The macroscopic density equation 2.8 provides the third equation. There are several methods of providing the last equation.

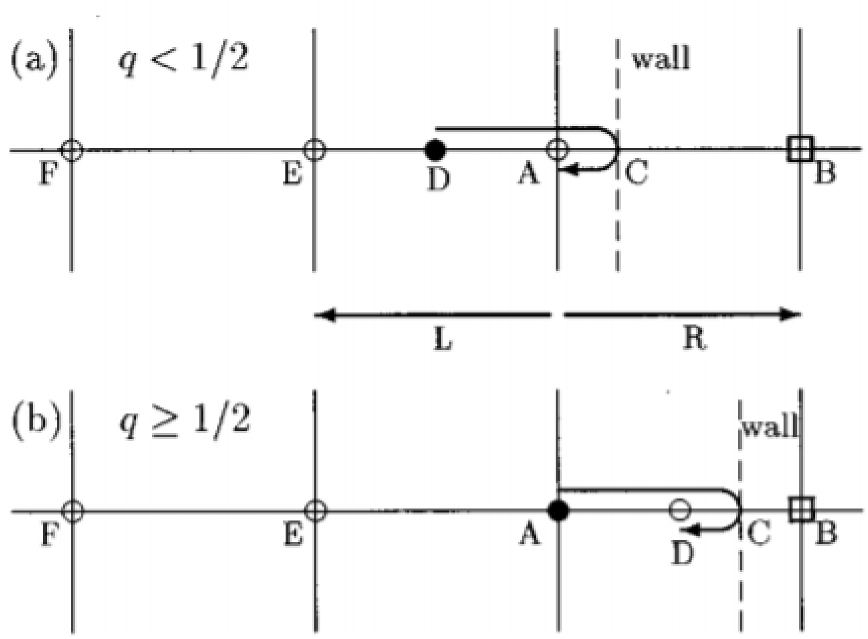

Figure 2.5: Representation of the Linear wall interpolation method, as proposed and taken by Bouzidi et al. [10].

One well known boundary method is the one proposed by Zou and He [90, 111], which uses the bounce-back condition $f_2 - f_2^{eq} = f_4 - f_4^{eq}$ as the last equation. With other words, the bounce-back condition is satisfied in the normal direction of the boundary. Solving for the four equations then prescribes the boundary condition.
Similarly one can describe a Dirichlet boundary condition. A Dirichlet boundary condition is a boundary condition that prescribes a constant value. An example of a Dirichlet boundary condition is a pressure outlet. The description of a Dirichlet boundary in Lattice Boltzmann is very similar to the description of the Von Neumann boundary condition. In a pressure outlet, a density is prescribed since the two parameters are related according to the equation of state as described in equation 2.24. Similar to the Von Neumann case, there are four unknowns at the boundary. In the case of a pressure outlet in a horizontal plane, as seen earlier in figure 2.6, the unknowns are f_7, f_4, f_8 and the velocity v. The same equations as in the Von Neumann boundary condition are used to prescribe the Dirichlet boundary condition [90, 111]. Other configurations of boundary conditions work similar due to symmetry.

Equilibrium boundary condition

A simple way of prescribing the densities at a boundary can be done by equalling them to their equilibrium condition, as given in equation 2.14 [41]. Since the equilibrium condition is only dependent on its macroscopic quantities, it can be straightforward implemented, hence:

$$f_i(\mathbf{x}, t) = w_i \rho(\mathbf{x}) \left(1 + \frac{\mathbf{e_i} \cdot \mathbf{u_{eq}}}{c_s^2} + \frac{1}{2}\frac{(\mathbf{e_i} \cdot \mathbf{u_{eq}})^2}{c_s^4} - \frac{\mathbf{u_{eq}}^2}{2c_s^2}\right) \tag{2.35}$$

The equilibrium boundary condition has however one major drawback. The scheme is only second order accurate if $\tau = \Delta t$, any other choice of τ decreases the accuracy to first order. Note that the equilibrium boundary condition replaces all boundary distributions, and not only the unknowns.

Extrapolation method in Dirichlet and Neumann boundaries

Another method , which serves as an alternative of equilibrium condition is the extrapolation method [39, 110]. In this method, the unknown distribution function at the boundary nodes are extrapolated from the non-equilibrium part of the distributions from one or two of its neighbours. Recall the Lattice Boltzmann equation post collision, but described at the boundary node $\mathbf{x_b}$, which is denoted as 0 in figure 2.6:

$$\tilde{f}_0(\mathbf{x_b}, t + \Delta t) = (1 - \frac{1}{\tau}) f_0^{neq}(\mathbf{x_b}, t) + \frac{f_0^{\mathrm{eq}}(\mathbf{x_b}, t)}{\tau} \tag{2.36}$$

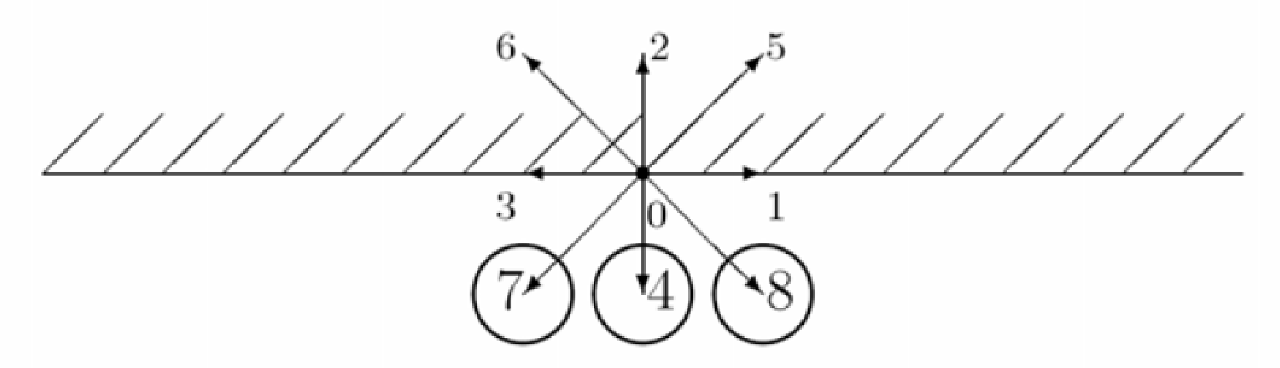

Figure 2.6: Schematic overview of a Von Neumann or Dirichlet boundary condition in a horizontal plane, unknown are the particle densities in the directions 4, 7 and 8 [90].

The non-equilibrium part can be related, without going in to much depth, by using Chapman - Enskog analysis to its neighbouring node 4:

$$f_0^{neq}(\mathbf{x_b}, t + \Delta t) = f_4(\mathbf{x_b}, t) - f_4^{eq}(\mathbf{x_b}, t) + \mathcal{O}\left(\epsilon^2\right) \tag{2.37}$$

The equilibrium part is then described by an adjusted version of equation 2.14, which is different for pressure and velocity boundaries. The final statement becomes:

$$\tilde{f}_0(\mathbf{x_b}, t + \Delta t) = (1 - \frac{1}{\tau})(f_4(\mathbf{x_b}, t) - f_4^{eq}(\mathbf{x_b}, t)) + f_0^{\hat{eq}}(\mathbf{x_b}, t) \tag{2.38}$$

With $f_0^{\hat{eq}}$ the adjusted equilibrium equation. Similarly, the extrapolation can be done with 2 neighbouring nodes. This increases the order of error, but is more vulnerable to numerical instabilities [110].

Pressure anti-bounce back

The pressure anti-bounce back method uses almost the same condition as the bounce back boundary condition, but the sign changes on bounced back distribution functions. At the boundary the equation is given as:

$$f_i\left(\mathbf{x_b}, t + \Delta t\right) = -f_i\left(\mathbf{x_b}, t\right) + 2w_i\rho_{eq}\left[1 + \frac{\left(\mathbf{e_i} \cdot \mathbf{u_{eq}}\right)^2}{2c_s^4} - \frac{\mathbf{u_{eq}}^2}{2c_s^2}\right] \tag{2.39}$$

The only unknown is the velocity $\mathbf{u_{eq}}$, which is often obtained by extrapolation from its neighbouring nodes. Note that equation 2.39 only has terms in the order of the macroscopic velocity squared, which causes estimation errors in $\mathbf{u_{eq}}$ to be less significant.

2.4 APES

In the remainder of the thesis, APES (Adaptable Poly-Engineering Simulator) will be used to obtain meshes and simulate the flow using the Lattice Boltzmann method [40, 83]. APES is a suite of solvers that is developed for use on parallel computers and with a high parallel efficiency [40, 77]. APES consists of individual components, each for a different purpose. The components that will be used are Seeder for mesh generation and Musubi as the Lattice Boltzmann solver. Harvester is the module that is used to obtain VTK files, Aotus is a module that is used in APES for the configuration and TreELM is used by APES as a library providing the mechanisms to work with the mesh. An overview of the interaction between each component in the APES suite can be seen in figure 2.7.

2.4.1 Seeder

Lattice Boltzmann uses a structured grid, which will be provided in this thesis by the module Seeder. The mesh is generated by a octree data structure, starting from a bounding box and recursively refines in each spatial direction [83]. The actual geometry is described by triangles and the bounding cube is refined towards the geometry. Every intersection with a triangle is marked.The fluid domain is determined by a flooding mechanics. A seed has to be placed in the fluid domain and from there the fluid space is created. First the neighbouring cells which are not identified as walls are given

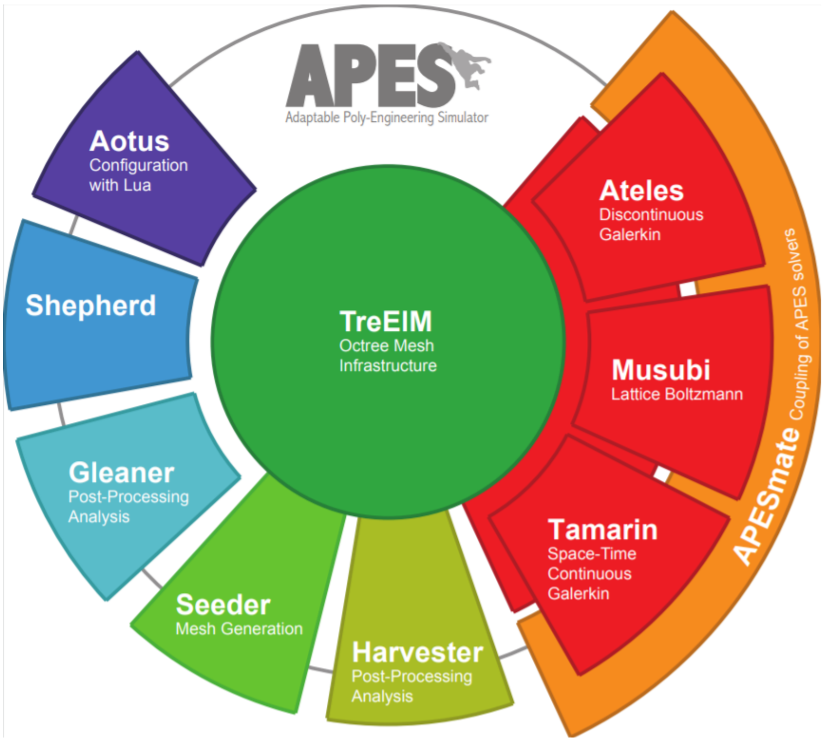

Figure 2.7: Overview of the end-to-end parallel tool-chain APES [40].

the fluid identifier. This procedure is then performed over and over again until all elements are identified as either fluid or solid.

2.4.2 Musubi

Musubi will be used as the solver for the Lattice Boltzmann equations. It is shown that is can solve complex problems [29]. The solver works by mapping the fluid elements in a one-dimensional array [83]. The elements are linked with their neighbours by an additional connectivity array. This array ensures that there are as few links as possible. Research in the performance of Musubi showed that it is at most efficient if the amount of elements per core is somewhere between 1 million and 2000 [40, 77]. Many different boundary conditions are already implemented in Musubi. Pressure outlets with the pressure anti-bounce-back method, the equilibrium method and the the extrapolation method are easily implementable. Velocity boundary conditions that are already in the code implemented are among others the equilibrium method and the bounce-back method. Advanced options are also possible in Musubi, such as passive scalar transport, grid refinement, immersed boundary method and multi-species flow [36].

2.4.3 Execution of the code

APES was installed and executed at two instances: a local cluster at the faculty of Thermal Fluid Engineering of the University of Twente and the Dutch supercomputer Cartesius, part of ICT cooperation organisation of educational and research institutions SURF. Performance of the cluster at the University of Twente is heavily influenced by the amount of users present at that certain moment. Cartesius works with Slurm Workload Manager and does not have this problem. The maximum amount of cores used at cartesius is 7200, while the absolute maximum amount of cores that can be used at the cluster at the University is 480.

3 | Comparison of Lattice Boltzmann method with the Finite Volume Method

To gain a more in depth knowledge of the performance of the Lattice Boltzmann method, APES and Musubi, a benchmark problem study is performed on laminar flow around a cylinder as described in Benchmark Computations of Laminar Flow Around a Cylinder by M. Schäfer and S. Turek [84]. In this paper, ten groups participated in a study, using different kind of solving methods such as the Finite Difference Method, the Finite Volume Method and the Finite Element Method. The Lattice Boltzmann method differs fundamentally from the more established methods and software such as the Finite Volume Method used by Ansys, which solves the Navier-Stokes equations. The results and performance of the Lattice Boltzmann method are therefore compared with Ansys Fluent. Additionally, the influence of the relaxation time τ, and therefore (due to the parameter coupling) the time step size is studied.

3.1 Benchmark case description

The flow around a circular cylinder is studied in 2D. The geometry of the case can be seen in figure 3.1. The fluid is considered to be Newtonian and incompressible, with a kinematic viscosity of $\nu = 1.0 \cdot 10^{-3}\ \mathrm{m^2/s}$ and a density of $\rho = 1.0\ \mathrm{kg/m^3}$. The equations for the conservation of mass and momentum can then respectively be given as:

$$\frac{\partial \mathbf{u_i}}{\partial \mathbf{x_i}} = 0 \tag{3.1}$$

$$\rho\frac{\partial \mathbf{u_i}}{\partial t} + \rho\frac{\partial}{\partial \mathbf{x_j}}\left(\mathbf{u_j}\mathbf{u_i}\right) = \rho\nu\frac{\partial}{\partial \mathbf{x_j}}\left(\frac{\partial \mathbf{u_i}}{\partial \mathbf{x_j}} + \frac{\partial \mathbf{u_j}}{\partial \mathbf{x_i}}\right) - \frac{\partial P}{\partial \mathbf{x_i}} \tag{3.2}$$

The inflow condition is determined to be:

$$u(0,y,t) = 4U_m y\left(H-y\right)/H^2 \quad , \quad v = 0 \quad \text{and} \quad U_m = 1.5 \tag{3.3}$$

With H the height of the inlet and U_m the maximum inflow velocity magnitude in $\mathrm{m/s}$. The Reynolds number is calculated using the cylinder diameter and the average inlet velocity $\bar{U} = 2u(0, H/2, t)/3$ as $\mathrm{Re} = \frac{\bar{U}D}{\nu} = 100$. The parameters that are monitored are the lift coefficient (C_L) , the drag coefficient (C_D), the Strouhal number (Str) and the pressure drop over the cylinder (ΔP), which are given as:

$$C_L = \frac{2D}{\rho\bar{U}^2 D} \quad , \quad C_D = \frac{2L}{\rho\bar{U}^2 D} \quad , \quad Str = \frac{fL}{\bar{U}}, \quad , \quad \Delta P = P(0.15, 0.2, t) - P(0.25, 0.2, t) \tag{3.4}$$

The Strouhal number is of interest since it is showed that with these flow specifications, a von Kármán vortex street is observed. This is a behaviour that is characterised by a frequent vortex shedding flow behind an object. The lattice parameters are calculated as described in section section 2.3.2: The grid spacing size h or dx and the relaxation parameter τ are chosen. All other parameters are calculated by these two values. Linear wall interpolation is used to obtain higher resolution calculations for the drag and lift coefficient. There is a significant difference in lift and drag coefficients obtained when linear wall interpolation is used or not used. The same benchmark case was also investigated by Beigzadeh-Abbassi et al. [5], who conducted a research on the different boundary conditions at the walls using Lattice Boltzmann.

3.2 Kármán vortex street: Results and performance of LBM

A snapshot of the velocity magnitude in which the von Kármán vortex street is visible can be seen in figure 3.2.

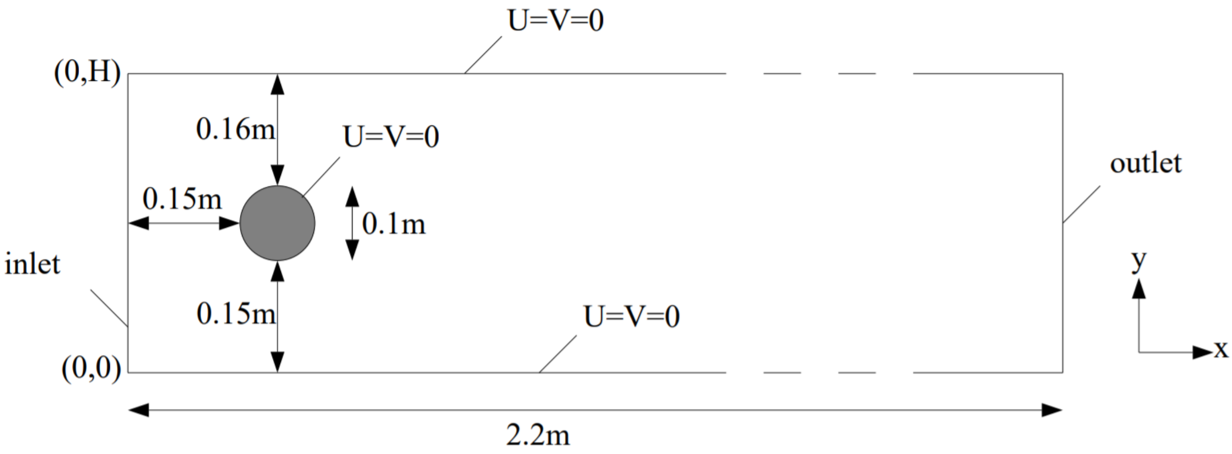

Figure 3.1: Overview of the benchmark case study [84].

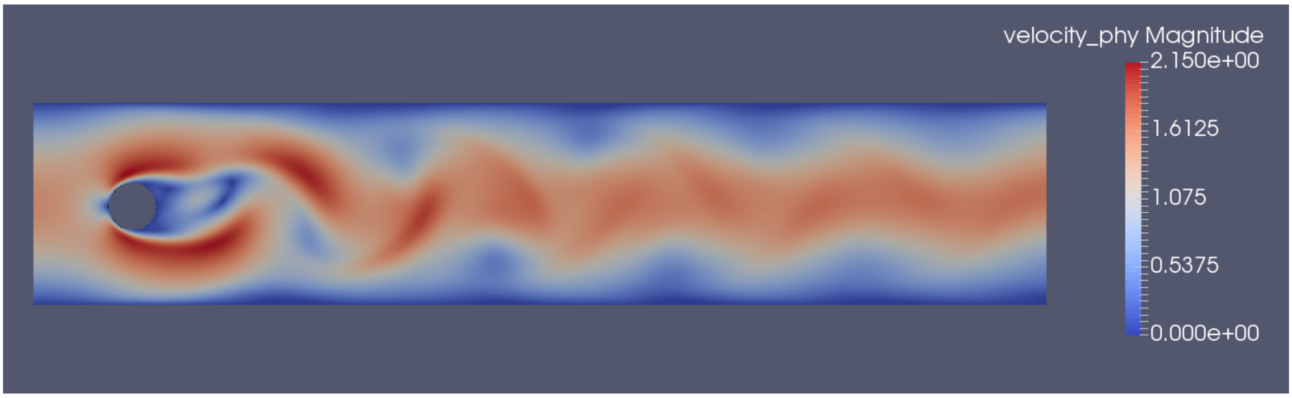

Figure 3.2: Snapshot of the velocity magnitude $\mathrm{m/s}$ at t=3.6 s, h = 0.0032 m.

A grid convergence study is performed while monitoring the lift and drag coefficient and the Strouhal number. The coarsest grid has a mesh size with $h = 0.0064$ m and the finest grid corresponds with $h = 0.0008$ m.
The values are based on the amount of elements in the $y-$ direction, which are 64 and 512 elements respectively. An overview of the cases can be seen in table 3.1. The pressure outlet is set to be of type extrapolation as described in paragraph 2.3.3 and the velocity inlet has a bounce-back condition. The relaxation parameter τ is chosen to be $0.526 = \frac{1}{1.9}$.
For $h = 0.0032$ m (or 128 elements in $y-$ direction) the computation time is monitored with a different number of cores. This is the so called strong scaling behaviour, as the number of processors increase for a problem of constant size. The results are projected in figure 3.3. It can be seen that computing with twice as many cores reduces the computation time by less than 2. Ideally, in theory, the computation time should reduce by a factor 2 when using twice as many cores and regarding a perfectly divided workload and no shared resources and communication between the cores. However, by Amdahl's law, the reduction in computation time is in practice always lower than 2.
The ratios between the cores going from the lowest amount of cores and increasing are 1.81, 1.84 , 1.81 and 1.53 respectively. The transition from 8 to 16 cores reduces the computation time only by a factor 1.53. This is probably due to the

Table 3.1: Overview of the different meshes and its corresponding time step. The pressure outlet is set to be of type extrapolation and the velocity inlet has a bounce back condition. Relaxation parameter τ = 0.526.

h (m)	meshsize	Δt (s)
0.0064	21792	3.60e-4
0.0032	87233	9.00e-5
0.0016	348805	2.250e-5
0.0008	1394467	5.625e-6

cores interacting with each other which also cost time and some parts of the computation that can or are not performed parallel. It is worth mentioning that all simulations are run on the shared Thermal Fluid Engineering cluster of the University of Twente, which performance is influenced by the amount of people using the cluster at the same time. Deviations in simulation time for the same simulations are experienced, but the complete influence on the performance is not explored. The parallel efficiency of Musubi is also investigated in a paper by Roller et al. [83]. It is shown that the parallel efficiency is very close to 1 for simulations on 16 cores, which was the lowest amount of cores investigated by Roller et al. [83].
The computation time on 16 cores is also monitored for the different grid sizes. An overview can be seen in figure 3.4. In this case, increasing h by a factor of 2 would theoretically result in an increase in computation time of $(2*2)^2$ when parallel computation is used optimal. The ratios between the computation time and the amount of elements going from the least amount and increasing are 30.2 , 15.7 and 15.2 respectively.
An overview of the grid comparison study with the flow parameters can be found in table 3.2. From the study, it can be seen that the flow parameters converge towards the proposed value by M. Schäfer et al. [84]. The solution may be regarded converged at $h = 0.0016$ m, since the maximum deviation between $h = 0.0016$ m and $h = 0.0008$ m is 1% for the maximum drag coefficient and less for the other coefficients and numbers. An overview of the results with different relaxation parameter values (τ) on the $h = 0.0032$ m cell grid can be found in table 3.3. From the coupling, a higher value of τ gives a bigger time step size. From the results it can be seen that smaller time steps provide results that are more in line with the proposed value. The ratio between the highest τ value and the lowest τ value is 1.26. It can be seen that increasing the value for τ with 26 % causes an increase in $C_{D,max}$, $C_{L,max}$ and ΔP of 15%, 4.4% and 2.9% respectively. It seems that a higher value of τ overestimates the flow parameters, with exception of $\tau = \frac{1}{1.85}$. No real conclusions can be drawn from this data, but from a starting point of view τ should possibly be chosen somewhere between $\tau = \frac{1}{1.80}$ and $\tau = \frac{1}{1.95}$.

Table 3.2: Comparison on different flow parameters as described in section 3.1 with different mesh sizes. All simulations have a τ value of 0.5263. The proposed value is the average of the lower and upper bound value as proposed by M. Schäfer et al.[84].

h (m)	Mesh size	$C_{D,max}$	$C_{L,max}$	Str	ΔP (Pa)
0.0064	21792	2.9700	0.9490	0.3100	2.3470
0.0032	87233	3.2576	1.0791	0.3000	2.4721
0.0016	348805	3.2183	1.0019	0.3000	2.5253
0.0008	1394467	3.2244	1.0025	0.3000	2.5187
Proposed value	-	3.2300	1.0000	0.3000	2.4800

Table 3.3: Comparison on different flow parameters as described in section 3.1 with different values of τ. All simulations have the same mesh size of 87233 cells. The proposed value is the average of the lower and upper bound value as proposed by M. Schäfer et al. [84].

τ	$C_{D,max}$	$C_{L,max}$	Str	ΔP (Pa)	Δt(s)	CPU time (s)
$\frac{1}{1.95}$	3.2277	1.0782	0.3000	2.4853	4.3840e-05	164.19
$\frac{1}{1.85}$	3.2137	1.0765	0.3000	2.5216	1.3865e-04	64.76
$\frac{1}{1.75}$	3.2469	1.1036	0.3000	2.5264	2.4429e-04	44.06
$\frac{1}{1.65}$	3.2538	1.1803	0.3000	2.5835	3.6273e-04	34.30
$\frac{1}{1.55}$	3.3704	1.2624	0.2899	2.5600	4.9645e-04	29.22
Proposed value	3.2300	1.0000	0.3000	2.4800		

3.3 Comparison with Ansys Fluent

To compare the results of the Lattice Boltzmann method with a Finite Volume Method, Ansys Fluent 2019 is used. The software provides two different solvers, a pressure-based solver and a density based solver [34]. The pressure based solver was used, since this solver is most suitable for incompressible flows. To compare the results with Ansys Fluent, the same parameters as mentioned in section 3.1 are monitored. Additionally, the velocity profiles are obtained at the following positions;
$x = [0, 0.05, 0.10, 0.14, 0.2, 0.26, 0.3, 0.5, 0.7, 0.9, 1, 1.2, 1.4, 1.5, 1.6, 2, 2.2]$ with $0 \leq y \leq 0.41$ m and $y = [0.35, 0.205]$ with $0 \leq x \leq 2.2$ m and at the point $P_0 = [1.1, 0.21]$ m. A linear ramping function for the velocity inflow condition was set to be 1 s long. A mesh was generated with 410543 nodes for the Fluent simulations, as smaller mesh resolutions (100K) showed insufficiently accurate results.

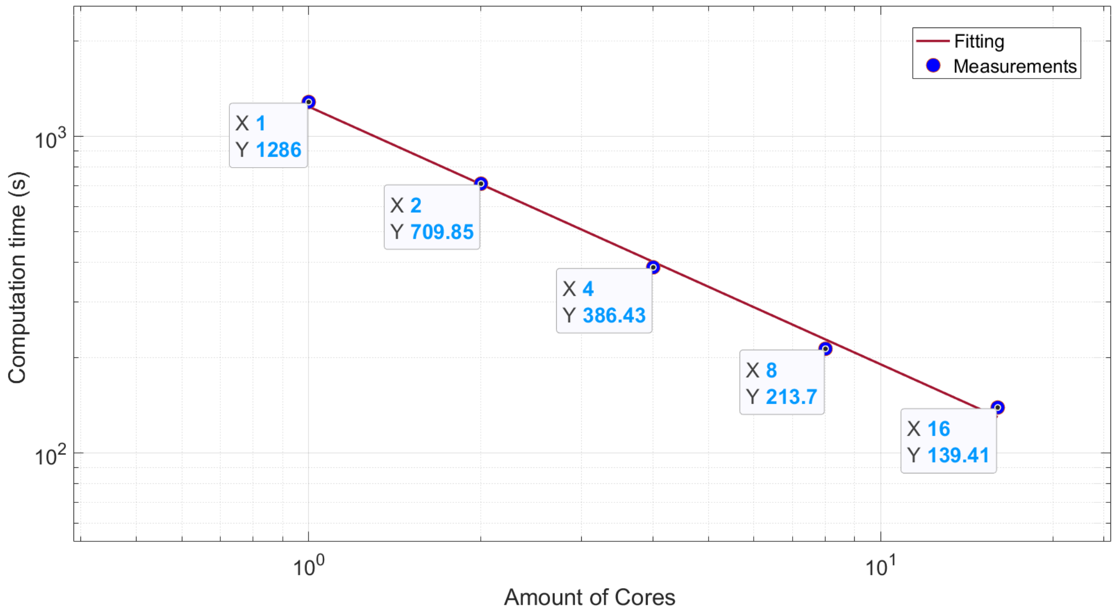

Figure 3.3: Computation time against the amount of cores used, for $h = 0.0032$ m.

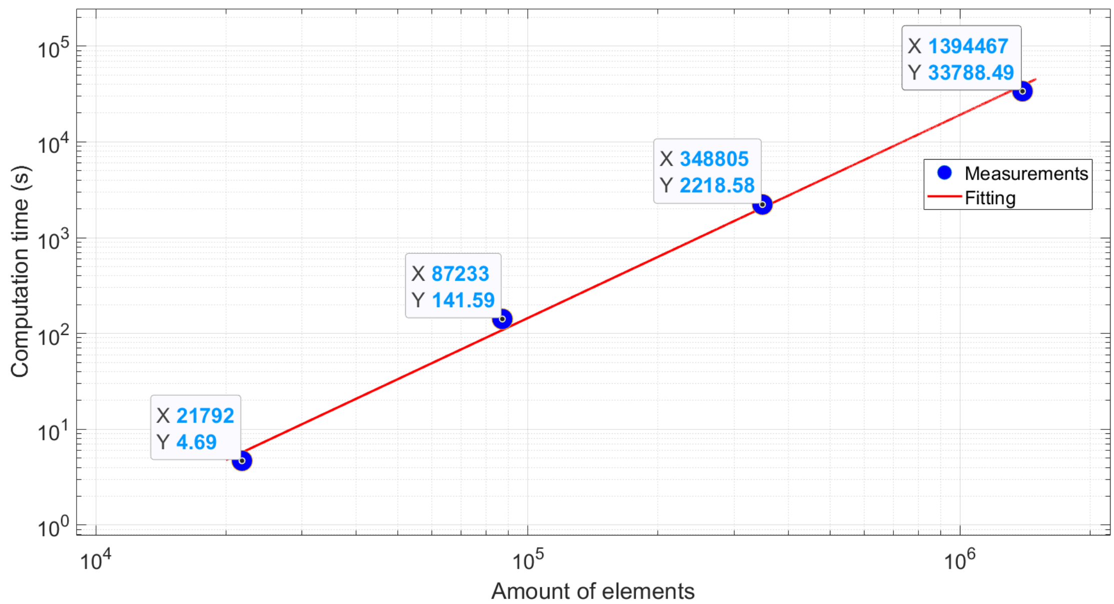

Figure 3.4: Computation time against amount of elements, running at 16 cores.

A close up of the mesh in the vicinity of the cylinder can be seen in figure 3.5. A transient pressure-based simulation was chosen with the PISO pressure-velocity coupling. Spatial gradient discretization was done by using the Least Squares Cell Based method and the pressure and momentum discretization was done by PRESTO! and QUICK methods respectively. Transient simulations were performed by using a second order implicit scheme. A $5e$-04 s time step size was chosen and convergence per time step was set if all absolute residuals were beneath $1e$-05 s.
The Lattice Boltzmann mesh used for comparison consists of 348805 elements, which corresponds with h of 0.0016 m, since the solution is regarded converged with this resolution. Both LBM and Fluent simulations were run for 10 s.

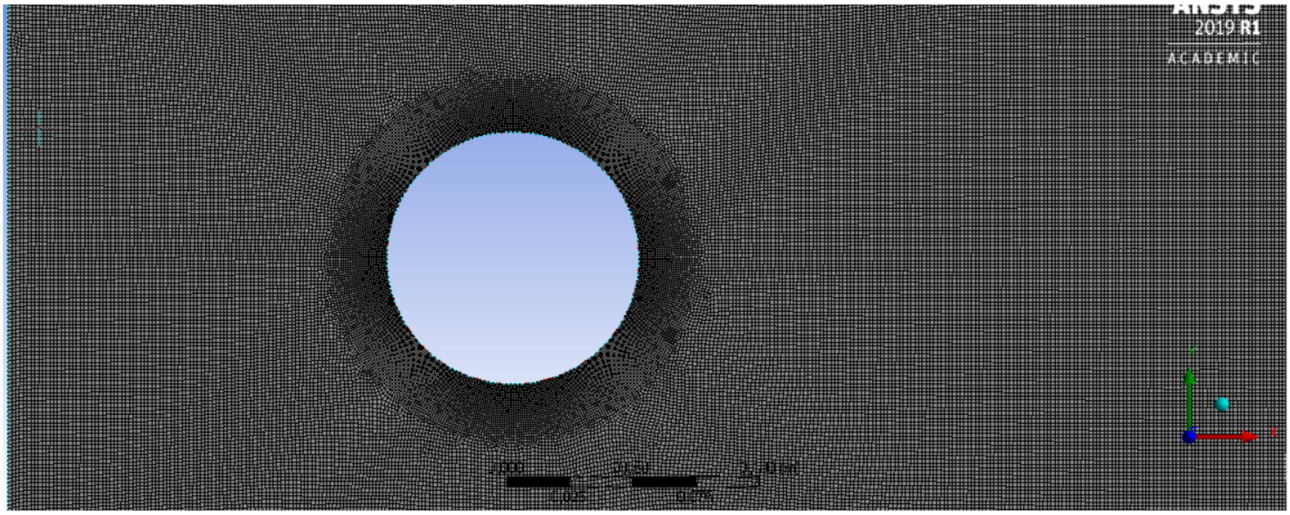

Figure 3.5: Close up of the 410543 mesh in the vicinity of the cylinder.

3.3.1 Flow physics comparison

Both the Fluent and the LBM simulation give results in good agreement with the values from the paper by M. Schäfer and S. Turek [84]. The Fluent simulation took 35520 seconds to finish, while the LBM simulation took 22843 seconds on the same amount of cores. A comparison of the characteristic flow parameters can be found in table 3.4. The lift coefficient as function of time is shown in figure 3.6.

Table 3.4: Comparison on different flow parameters as described in section 3.1, the proposed value is the average of the lower bound and upper bound value as proposed by M. Schäfer et al. [84].

	$C_{D,max}$	$C_{L,max}$	Str	ΔP (Pa)
LBM	3.2244	1.0025	0.3000	2.5253
Fluent	3.2780	0.9907	0.3047	2.4661
Proposed value	3.2300	1.0000	0.3000	2.4800

The difference in the calculated lift coefficient between the two simulation methods can be seen in figure 3.7. It can be seen from figure 3.7 that the difference is quite high, though this is mainly due to a combination of a high rate of change in the lift coefficient over time and a slight phase change between both simulation methods.
The L_1 error norm (mean absolute deviation) and the L_2 error norms are calculated for the $x-$ and $y-$velocity at $P_0 = [1.1, 0.21]$ m (halfway the geometry) and the lift and drag coefficients, where the norms are defined as :

$$L_1 = \frac{1}{n}\sum_{i=1}^{n} |\lambda_{LBM}(i) - \lambda_{Fluent}(i)| \qquad and \qquad L_2 = \frac{1}{n}\sum_{i=1}^{n} (\lambda_{LBM}(i) - \lambda_{Fluent}(i))^2 \tag{3.5}$$

In these equations, n is the number of data points and $\lambda(i)$ the value of the flow parameter at (i). The values are listed in table 3.5.

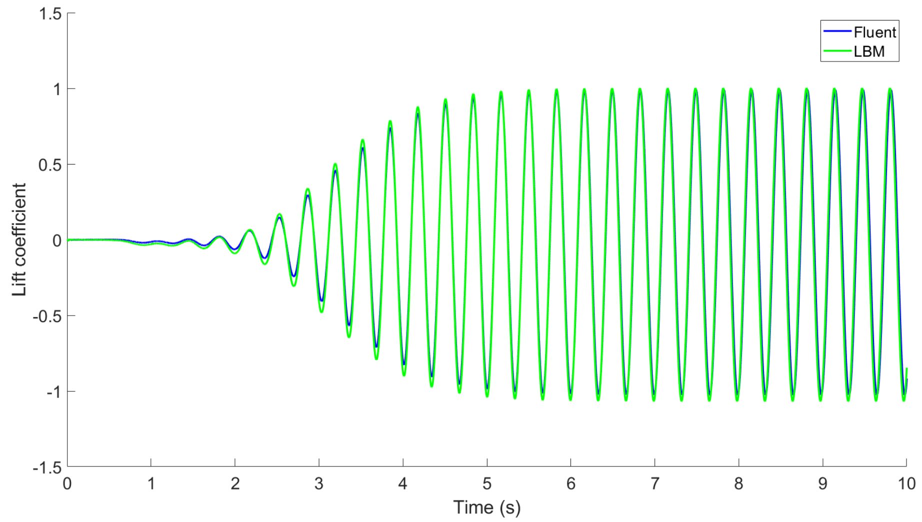

Figure 3.6: Comparison of the lift coefficient of the cylinder between Fluent and Lattice Boltzmann.

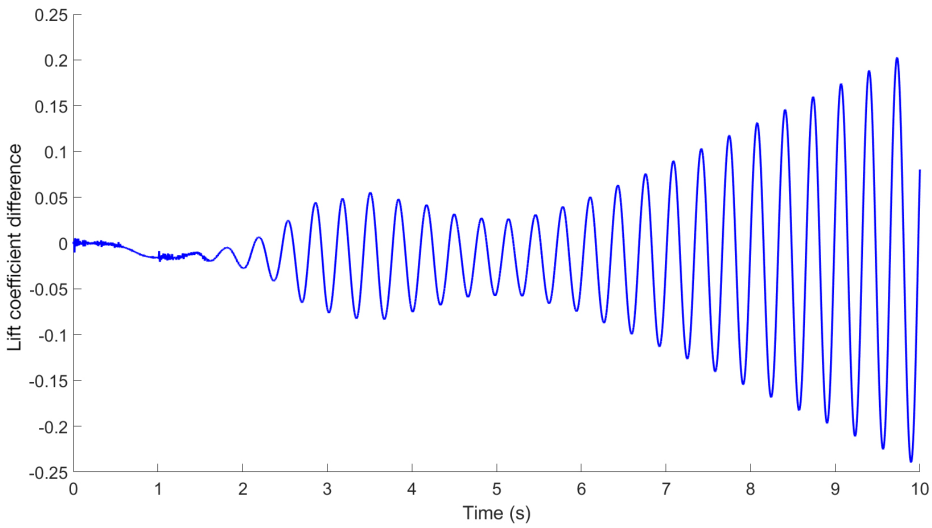

Figure 3.7: Difference (LBM - Fluent) of the lift coefficient of the cylinder between Fluent and Lattice Boltzmann over time.

Table 3.5: List of the Maximum absolute difference, the L_1 norm and the L_2 norm for different flow parameters ($P_0 = [1.1, 0.21]$) m.

	C_D	C_L	$x-$velocity at P_0 (m/s)	$y-$velocity at P_0 (m/s)	ΔP (Pa)
Maximum absolute difference	0.48	0.239	0.194	0.242	0.334
L_1	0.038	0.052	0.019	0.030	0.025
L_2	2.2e-3	5.4e-3	8.7e-4	2.1e-3	1.0e-3

3.3.2 Velocity profiles

The velocity profiles in $x-$direction and $y-$direction are obtained for both Fluent and Lattice Boltzmann at the positions mentioned in section 3.3. The time averaged velocity profiles in $x-$direction can be seen in figure 3.8, and a close up in the vicinity of the cylinder can be seen in figure 3.9. The time averaged velocity magnitude in $x-$ and $y-$direction at the center line ($y = 0.205$ m) can be seen in figure 3.10. Figure 3.11 is added to show that the profiles also match at each time step. From the velocity profiles and the flow parameters it can be concluded that the Lattice Boltzmann method shows results similar to Ansys Fluent and to the results from the benchmark paper.

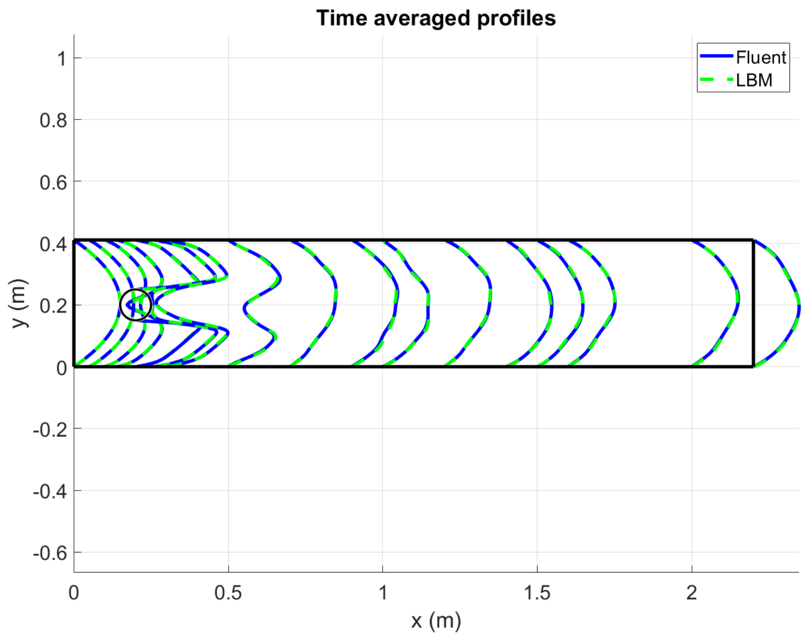

Figure 3.8: Time averaged velocity profiles in x-direction. Note that the velocity lines through the cylinders do not represent flow through the cylinders but is a result of the scaling of the velocity profiles

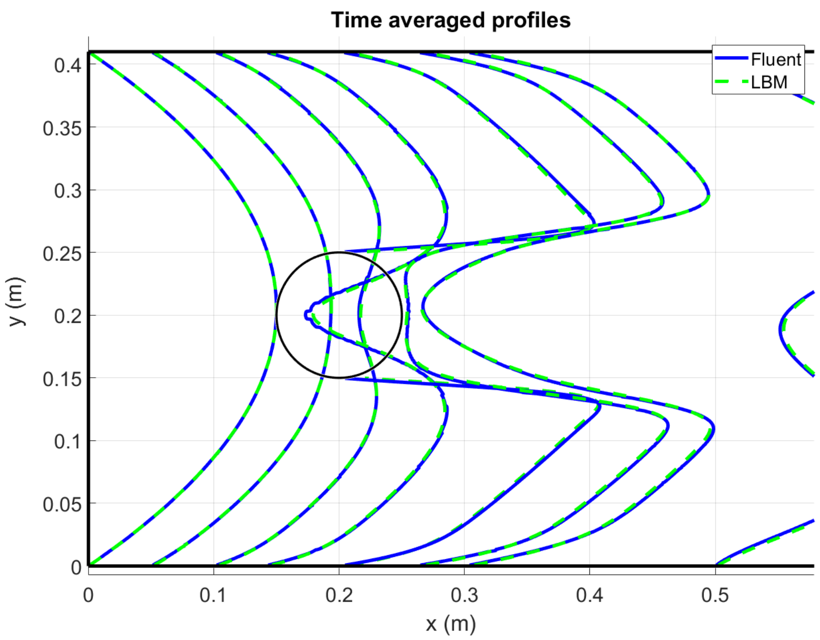

Figure 3.9: Close up of the time averaged velocity profiles in x-direction in the vicinity of the cylinder. Note that the velocity lines through the cylinders do not represent flow through the cylinders but is a result of the scaling of the velocity profiles.

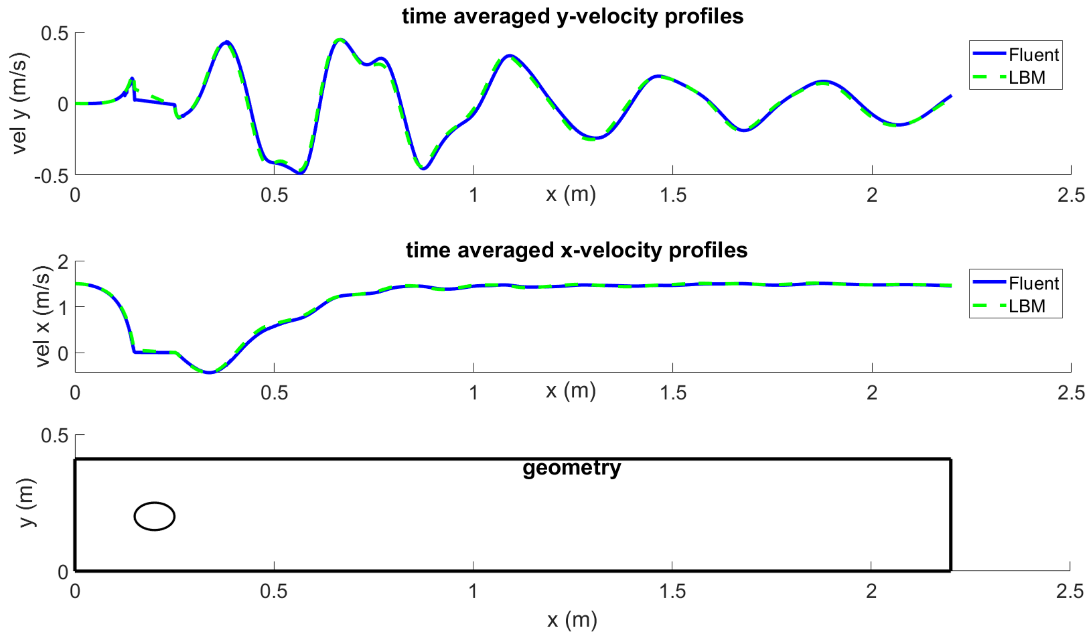

Figure 3.10: The time averaged velocity magnitude $\mathrm{m/s}$ in $x-$ and $y-$direction at the center line ($y = 0.205$ m). Geometry plot included for reference.

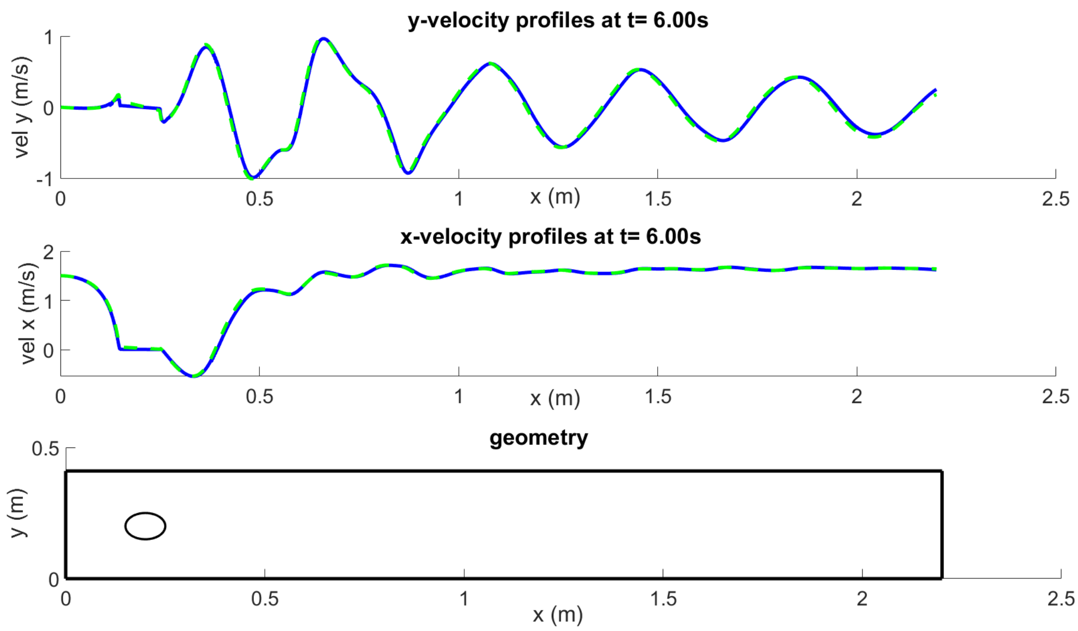

Figure 3.11: Velocity magnitude $\mathrm{m/s}$ in $x-$ and $y-$direction at the center line ($y = 0.205$ m). Geometry plot included for reference.

4 | Flow in a femoral artery bifurcation: A comparison of Lattice Boltzmann and the Finite Element method

In chapter 3, the convergence and the performance of the code was studied in a 2D benchmark case of flow around a cylinder. In this chapter, the 3D flow of blood in a femoral artery will be simulated and compared with results calculated with the software SimVascular by a colleague. SimVascular is an open source simulation program specialised in cardiovascular simulations, providing a complete package, from medical image data segmentation to patient-specific blood flow simulation and analysis based on the finite element method [95].

4.1 Case description

The case is based on the femoral artery bifurcation study in SimVascular by Van de Velde [96]. The comparison of Lattice Boltzmann and SimVascular was made with the author's collaboration. Only the steady state solution is compared. Van de Velde segmented the patient anatomy by VMTKlab to obtain a 3D model that was also used in the Lattice Boltzmann simulations. An extended inlet with an inlet radius of 4.86 mm was created in the artery to ensure fully developed flow at the inlet of the actual artery geometry. The diameter of the Arteria Femoralis Profunda (AFP) outlet is 4.89 mm and the diameter of the Arteria Femoralis Superficialis (AFS) outlet is 4.95 mm. Boundary conditions for SimVascular were obtained by using duplex ultrasound and the boundary condition at the outflow was prescribed by a three-element (RCR) Windkessel model. This model works similar to an electric resistor–capacitor-resistor circuit. In the case of the femoral artery represents R_1 the characteristic resistance, R_2 the peripheral resistance, C the ratio of blood volume to blood pressure and the pressure over time has the same role as electric potential in the equivalent RCR-circuit. For steady state, the model reduces to a single R value. In the Lattice Boltzmann simulations, the outflow was not prescribed by this RCR-model, but the solution to the outflow pressure obtained by the steady state simulations from SimVascular are prescribed. Therefore, pressure outlets with a constant pressure of 13.86 mPa in the AFS and 13.98 mPa in the AFP were prescribed. A steady inlet flow of 12400 $\mathrm{mm^3/s}$ was applied with a parabolic velocity inlet profile, which corresponds with a maximum inlet velocity of 334.70 $\mathrm{mm/s}$. The wall was assumed to be rigid. The Reynolds number at the inlet is calculated by using the inlet diameter D (mm) as:

$$Re = \frac{\rho U D}{\mu} = 492.75 \tag{4.1}$$

In the compared case, the density (ρ) of the fluid was assumed to be $1.06 \cdot 10^{-6}\ \mathrm{kg/mm^3}$ and the blood was assumed to be Newtonian with a dynamic viscosity (μ) of $3.45 \cdot 10^{-6}\ \mathrm{kg/mm \cdot s}$. Although blood is a non-Newtonian fluid, studies show that velocity and pressure distributions are similar in simulations whether non-Newtonian or Newtonian fluid is assumed. Non-Newtonian fluid does however significantly increase the wall shear stress value [42]. Other studies compares the use of non-Newtonian and Newtonian blood in a bifurcation and found the biggest difference in velocity was obtained near the walls, up to a maximum deviation of 8% [23]. Non-Newtonian effects of blood are however less observed in larger blood vessels such as in this study [42]. Modelling with Newtonian fluid is therefore sufficient for this case study.

Several meshes for the Lattice Boltzmann simulations were created with Seeder. The mesh created for SimVascular simulations was created with the mesh creation tools in SimVascular and performed by Van de Velde [96]. A mesh composed of tetrahedral cells was created, with a refinement at the femoral bifurcation. The mesh for SimVascular simulations has 755664 cells. Simulations were performed with a time step size of $1.00 \cdot 10^{-4}$ s. A mesh convergence study was performed by van de Velde [96]. The mesh was considered converged if the the area-averaged wall shear stress at the first 50 mm of the AFS did not change more than 5% when doubling the mesh size. All Lattice Boltzmann simulation cases are listed in table 4.1. The lattice parameters are calculated as described in section 2.3.2 with the single-relaxation

Table 4.1: List of the simulation cases. All simulations were run on 32 cores. Parameters are calculated as described in section 2.3.2. The single relaxation time was set to be 0.5195 for all cases. *SimVascular simulations were run on 64 cores opposed to the 32 cores of the Lattice Boltzmann simulations.

Label	h (m)	mesh size (cells)	Pressure outlet type	time step size s	CPU till t = 0.4 s (min)
1	0.105	7186282	Expol	2.19e-05	28
2	0.10	8314471	Expol	1.99e-05	37
2 PAB	0.10	8314471	PAB	1.99e-05	59
2 EQ	0.10	8314471	EQ	1.99e-05	59
3	0.09	11399546	Expol	1.61e-05	67
4	0.08	16231326	Expol	1.27e-05	133
5	0.07	24232987	Expol	9.74e-06	287
6	0.0625	34042048	Expol	7.76e-06	465
SimVascular	-	755664	RCR	1.00e-04	132*

parameter chosen to be 0.5195. Six different grid sizes are compared. To study the influence of the different pressure outlet descriptions available in Musubsi, the case with 8314471 cells has been run for all three different pressure cases and its results compared. On all cases that do not have a subname, the extrapolation pressure method is used as described in 2.3.3: Extrapolation method in Dirichlet and Neumann boundaries.
The PAB subname indicates a pressure anti-bounce-back condition and the EQ subname indicates the equilibrium boundary condition. Both of them are also described in section 2.3.3.
The flow data has been monitored over three different lines. Line 1 consists of a straight line going from $1\text{A} = [0, 0, 1]$ mm to the constriction at $1\text{B} = [0, 0, 51]$ mm and a straight line going from 1B to the stagnation points at the bifurcation $1\text{C} = [-30, 0, 87]$ mm. Line 2 also consists of two separate lines which go through $2\text{A} = [-14, 1, 70]$ mm , $2\text{B} = [-44, 6, 103]$ mm and $2\text{C} = [-66, 9, 120]$ mm, which is at the outlet of the AFP. Line 3 is a horizontal line in the vicinity of the bifurcation between the points $3\text{A} = [-34, -6, 83]$ mm and $3\text{B} = [-27, -6, 90]$ mm. The placement of the lines in the geometry with its corresponding pressure and velocity plots can be seen in figure 4.1, 4.2 and figure 4.3
The computation time until the simulation reaches 0.4 s is compared, since this is the only known computation time obtained from SimVascular. Note that the SimVascular simulation has been performed on 64 cores, while the Lattice Boltzmann simulations were run on 32 cores. All Lattice Boltzmann simulations were run on the same cluster, but its performance varies by the workload and the heavy usage of the cluster by others.

4.2 Results

The simulation with the converged mesh in SimVascular was run to 1.0 seconds and the Lattice Boltzmann simulations were run to 1.5 seconds to ensure a steady-state. The percentage difference between the mean and maximum values of the pressure, wall shear stress and velocity magnitude all differ less than 0.02% with its values from the previous time step 0.1 second before, indicating that a steady-state has been reached. The SimVascular results at 1.0 seconds differ less than 0.06% from its previous time step, which is at $t = 0.95$ s.
The main flow parameters that are of interest are the wall shear stress, the pressure profiles and the velocity profiles. The mean and maximum values over the whole geometry are obtained, as well as the mean and maximum value of the shear stress at the walls. In table 4.2 the values of these flow parameters can be found. Plots of the pressure and velocity magnitude along lines in the geometry have been made, and can be seen in figures 4.1, 4.2 and 4.3. The three different pressure boundary conditions that are compared for the grid with $h = 0.10$ mm are also evaluated over the three different lines. The velocity and pressure contours of these cases are plotted in figure 4.4. The averages and maximum values over these lines are listed in table 4.4. Reynolds numbers are calculated at the outlet of the AFP and AFS and are only slightly mesh dependent, therefore determined to be approximately $Re_{AFP} \approx 413$ and $Re_{AFS} \approx 597$. The lattice Mach numbers are highly dependent on the grid spacing and can be seen in table 4.3

4.3 Discussion

It can be seen that there is some deviation in the numerical flow quantities obtained by Lattice Boltzmann when compared to the results by SimVascular, but there is little deviation in numerical results for the different cases in the LBM simulations. Based on the numerical values in table 4.2, it looks like the mesh is already resolved at the lowest grid size. Some of the maximum Mach numbers exceeded the ideal limit of 0.1, but this is only at places with high velocity.

Table 4.2: Lattice Boltzmann steady state results for the pressure, wall shear stress and velocity magnitude of the different cases compared with the steady state results from SimVascular.

Label number	Pressure (mPa)	Velocity Magnitude (mm/s)	Wall Shear stress ($\mathrm{kg/mm^2s}$)
Maximum values			
1	14.170	688.219	1.602e-2
2	14.236	688.333	1.635e-2
2 PAB	14.203	688.469	1.438e-2
2 EQ	14.161	688.207	1.595e-2
3	14.238	688.398	1.594e-2
4	14.236	688.456	1.701e-2
5	14.232	688.479	1.838e-2
6	14.229	688.505	1.898e-2
SimVascular	14.158	723.048	1.098e-2
Mean value			
1	14.100	226.673	1.644e-3
2	14.133	226.600	1.644e-3
2 PAB	14.058	226.598	1.644e-3
2 EQ	14.067	226.614	1.643e-3
3	14.133	226.737	1.658e-3
4	14.132	226.778	1.674e-3
5	14.127	226.781	1.687e-3
6	14.125	226.640	1.697e-3
SimVascular	14.046	162.272	1.822e-3

Table 4.3: Maximum Mach numbers obtained for the different grid sizes.

h (mm)	0.105	0.1	0.09	0.08	0.07	0.0625
$\mathrm{Ma_{max}}$	0.144	0.136	0.123	0.109	0.096	0.085

Table 4.4: Comparison of pressure and velocity mean and maximum values for the different pressure boundary conditions and SimVascular over the three lines.

		Mean		**Max**	
		Pressure (mPa)	Velocity magnitude (mm/s)	Pressure (mPa))	Velocity magnitude (mm/s)
Line 1	Expol	14.157	389.74	14.232	577.37
	PAB	14.083	389.52	14.158	577.34
	EQ	14.091	389.56	14.166	577.32
	SimVascular	14.082	387.37	14.157	553.27
Line 2	Expol	14.069	340.66	14.091	555.13
	PAB	13.993	346.82	14.016	555.19
	EQ	14.002	345.61	14.025	555.17
	SimVascular	13.989	273.33	14.007	551.76
Line 3	Expol	14.077	222.13	14.122	442.68
	PAB	14.003	221.85	14.046	445.94
	EQ	14.012	221.88	14.055	445.72
	SimVascular	13.998	194.99	14.043	508.42

When looking at the results for each case, it can be concluded that having a higher Mach number (0.144 for case 1) did not alter the global flow much when compared to the lowest Mach number.

More deviations are visible when comparing the LBM with SimVascular. It should be noted that Lattice Boltzmann and the SimVascular mesh are different and the SimVascular mesh is not structured, but uses layers at the wall. Meaning that there are relatively more cells at the wall than further inside the domain.

When calculating the mean values, no weighted mean was calculated but each cell contributed as much in the calculation. Therefore, the mean value of the SimVascular simulations are closer to the numerical values obtained at the wall than the Lattice Boltzmann mean values. Although the maximum values are different from the SimVascular simulations, calculating instead the 95 and 99 percentile give almost equal results. The n-th percentile is calculated by sorting all values for each cell and taking the value of the cell that has $n\%$ of the amount of cells with a lower value.
The 99th percentile of the velocity magnitude of case 2, case 6 and SimVascular are $589.05\ \mathrm{mm/s}$, $591.42\ \mathrm{mm/s}$, and $587.59\ \mathrm{mm/s}$ respectively. The 99th percentile of the wall shear stresses for these cases are 7.42e-02 $\mathrm{kg/mm \cdot s^2}$, 6.96e-02 $\mathrm{kg/mm \cdot s^2}$ and 7.23e-02 $\mathrm{kg/mm \cdot s^2}$.
The wall shear stress is of physiologic importance. In figure 4.8 it can be seen that the wall shear stress contours are very much a like. It can be seen from the pressure and velocity plot over the three lines that the pressure is very similar in behaviour, but that the amplitude differs for each case with SimVascular predicting the pressure lower than all the Lattice Boltzmann simulations with the extrapolated pressure outlet condition. However, from the different pressure outlet cases investigated can be seen that the extrapolation method predicts the highest pressure over the geometry, while the pressure anti-bounce-back method always predicts the lowest pressure which is very similar to the pressure predicted by SimVascular. The percentage difference between the mean and maximum pressure values over three lines are compared for the different pressure outlet cases with SimVascular and are listed in table 4.5.

Table 4.5: Percentage difference in pressure between SimVascular and Lattice Boltzmann simulations over Line 1, 2 and 3

		% difference in mean pressure	% difference in maximum pressure
Line 1	Expol	0.532	0.530
	PAB	0.002	0.007
	EQ	0.065	0.063
Line 2	Expol	0.570	0.600
	PAB	0.029	0.064
	EQ	0.094	0.129
Line 3	Expol	0.572	0.562
	PAB	0.042	0.021
	EQ	0.105	0.086

It can be concluded that the difference in pressure outlet boundaries does affect the pressure distribution over the geometry, but has only little to none effect on the velocity profiles. The velocity profiles of the Lattice Boltzmann simulations over line 1 and line 2 show many similarities with the profiles obtained from SimVascular, but the characteristics over line 3 are clearly different for both methods.

In figure 4.5 and figure 4.6 a comparison of the velocity profiles within the domain can be seen. Although the plots are very similar, some small differences can be spotted. If looked near the vicinity of the bifurcation, the Lattice Boltzmann simulations show some small vortices which are not detected in the simulation with SimVascular. The same can be observed when looking at several planes in the geometry, as in figure 4.7. Both Lattice Boltzmann and SimVascular did use direct numerical simulation and should therefore be able to capture vortices. The mesh in the SimVascular simulation is however much coarser, making it harder to capture the detailed vortex-like behaviour in the flow. This might also be the cause for the deviation in the numerical values along the lines as in figure 4.1, 4.2 and 4.3. Especially line 3 show great differences in simulations by Lattice Boltzmann and SimVascular. This is also a place where more turbulent behaviour occurs, therefore more deviation between fine and coarse grids are expected.

The differences between SimVascular and Lattice Boltzmann simulations are not delved into much detail due to the context of this thesis. Investigating the difference of LBM with a higher resolution SimVascular simulation might be interesting but SimVascular simulations are conducted in the past by a third party. Nevertheless, the comparison of LBM with the Finite Element Method in this chapter and the Finite Volume Method in chapter 3 shows that LBM is in good agreement with the Finite Volume and Finite Element Method, and is suitable for prediction macroscopic flow quantities in anatomical geometries at high resolutions.

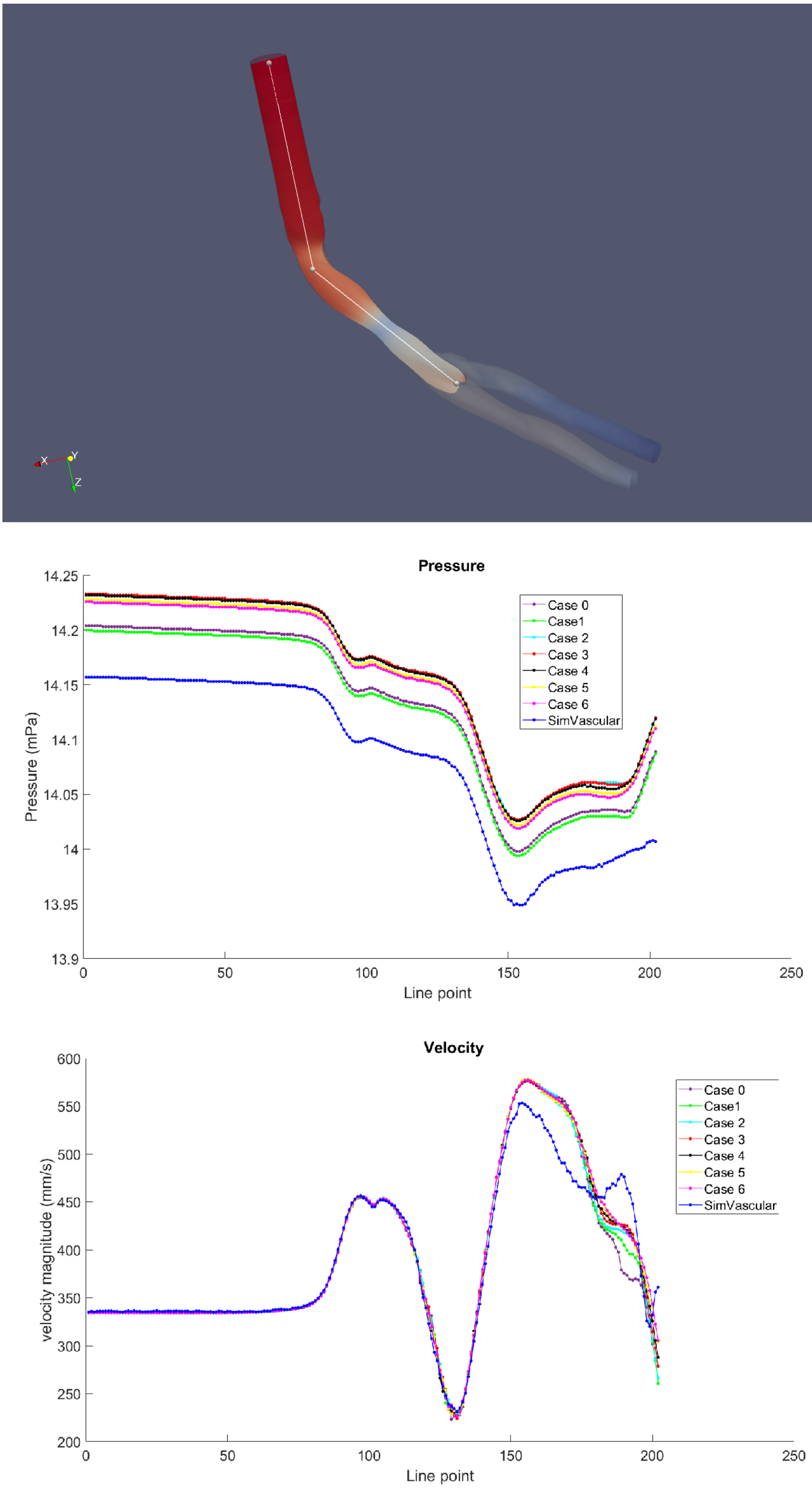

Figure 4.1: Top: depiction of the position of line 1 in the geometry. In the middle the pressure plot (mPa) and on the bottom the velocity magnitude $(\mathrm{mm/s})$ for the different cases.

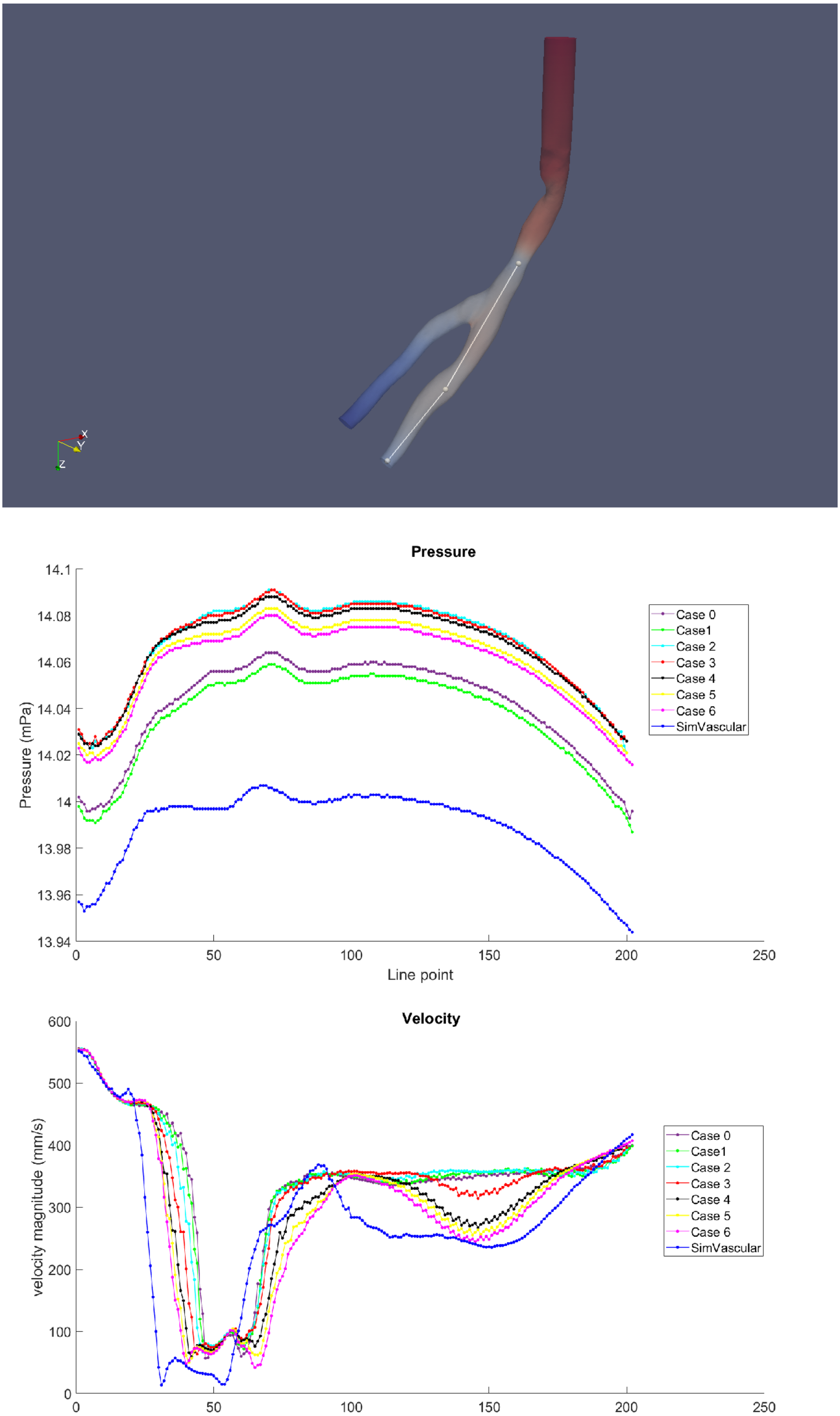

Figure 4.2: Top: depiction of the position of line 2 in the geometry. In the middle the pressure plot (mPa) and on the bottom the velocity magnitude ($\mathrm{mm/s}$) for the different cases.

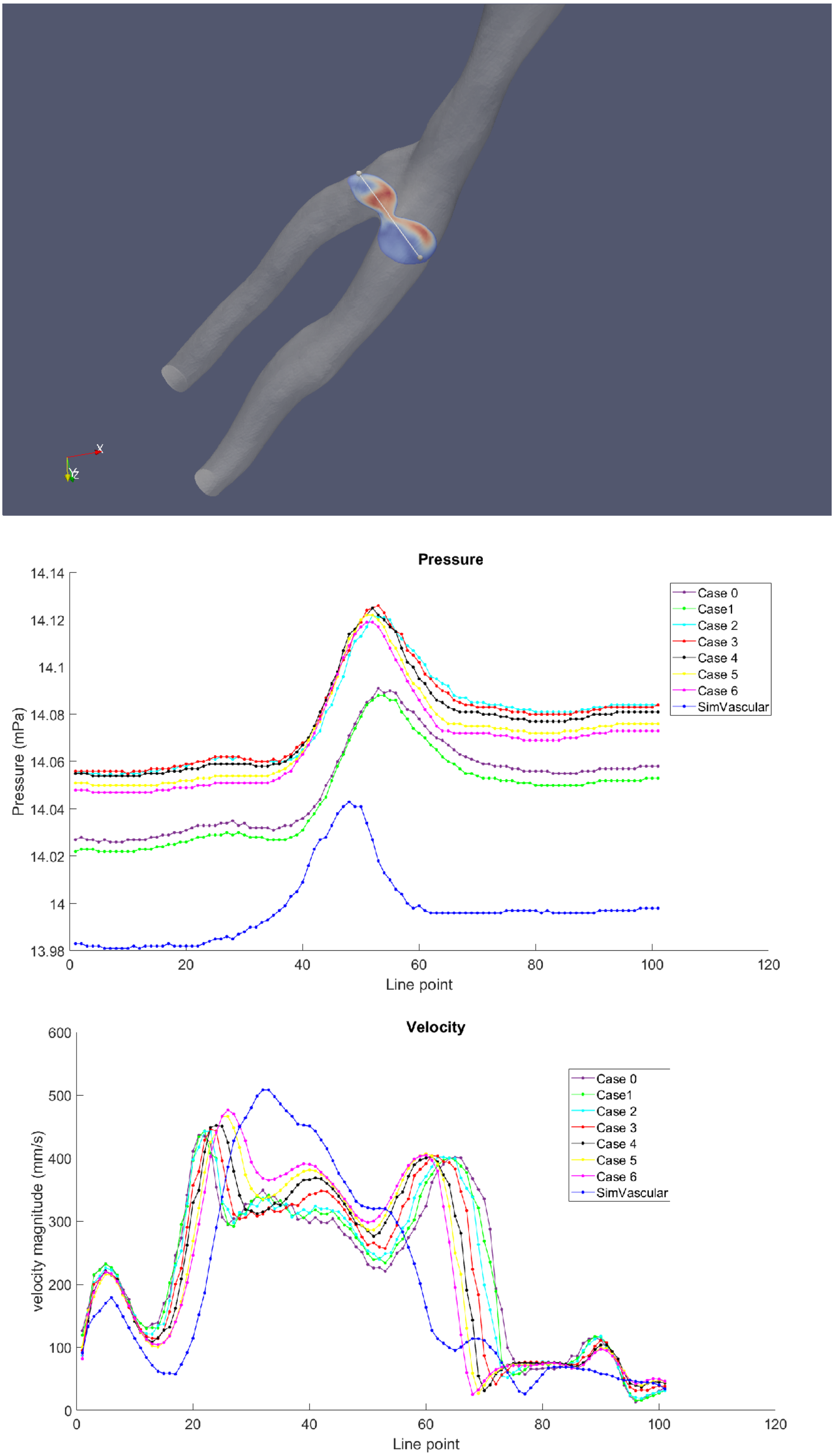

Figure 4.3: Top: depiction of the position of line 3 in the geometry. In the middle the pressure plot (mPa) and on the bottom the velocity magnitude $(\mathrm{mm/s})$ for the different cases.

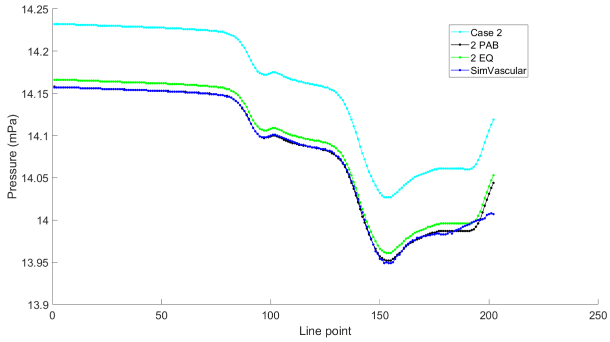

(a) Pressure line 1

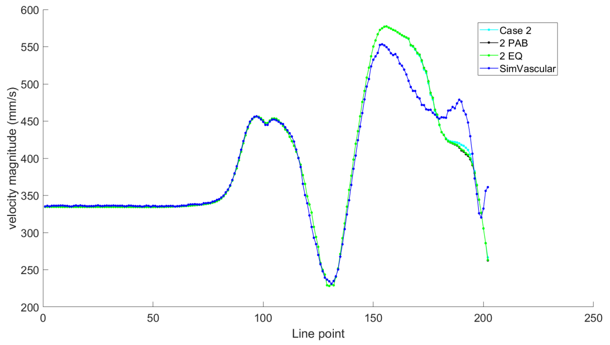

(b) Velocity line 1

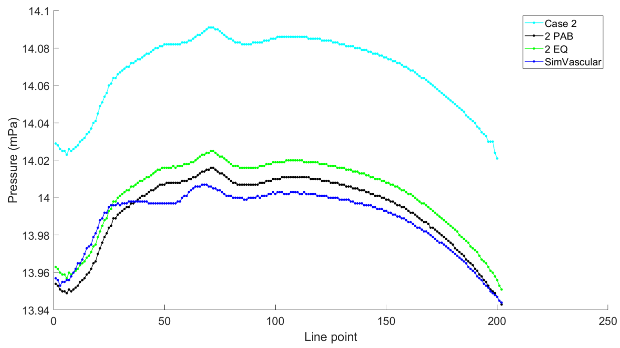

(c) Pressure line 2

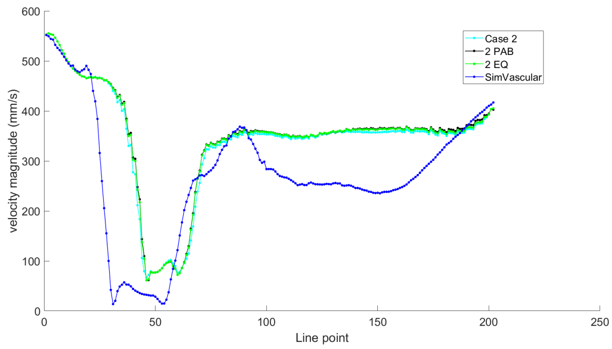

(d) Velocity line 2

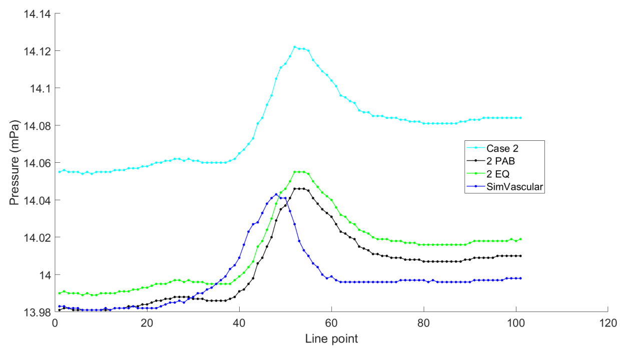

(e) Pressure line 3

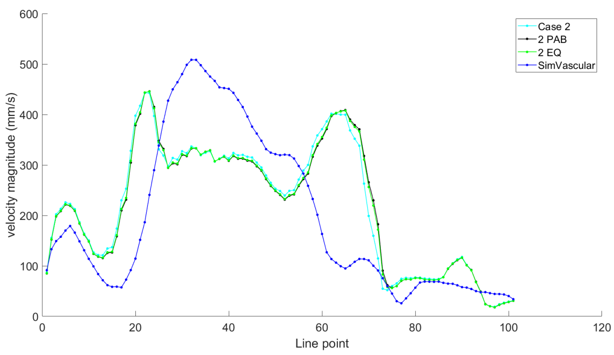

(f) Velocity line 3

Figure 4.4: Pressure (mPa) and velocity magnitude ($\mathrm{mm/s}$) plots of the three different pressure outlet cases compared with SimVascular over the three different lines

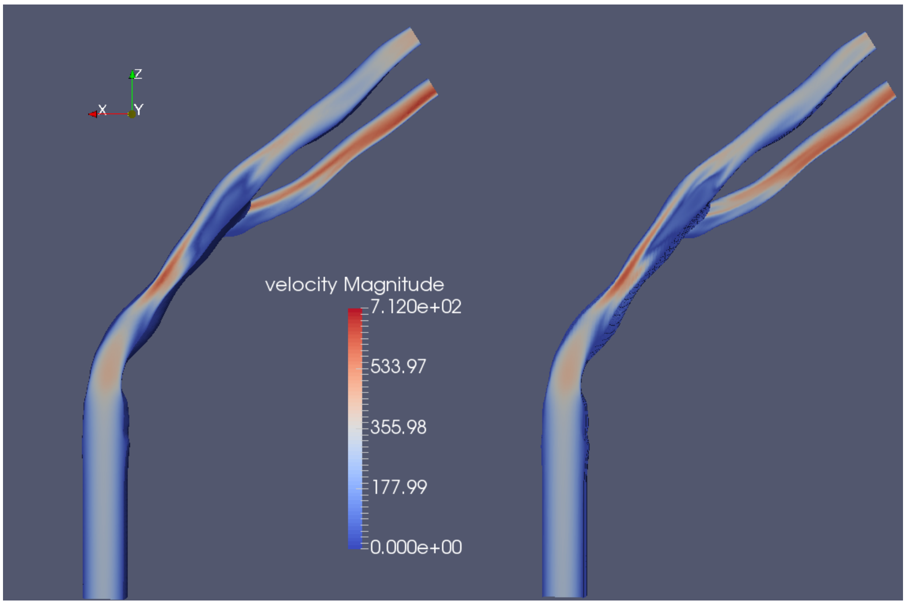

Figure 4.5: Left: a plot of the velocity magnitude $(\mathrm{mm/s})$ in bifurcation with results from SimVascular. Right: the same plot by LBM, case 4.

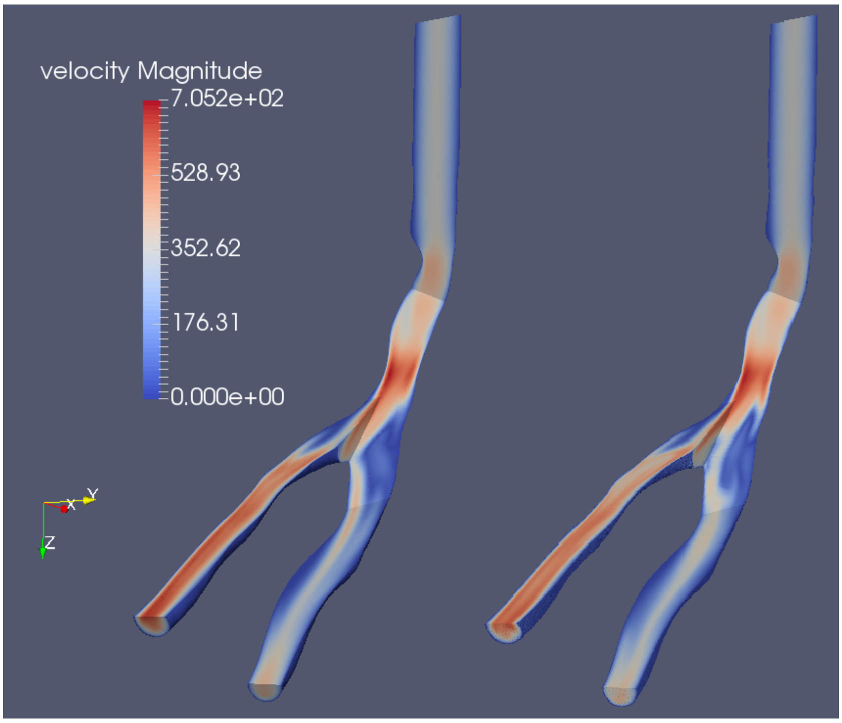

Figure 4.6: Left: a plot of the velocity magnitude $(\mathrm{mm/s})$ near the bifurcation with results from SimVascular. Right: the same plot by LBM, case 4.

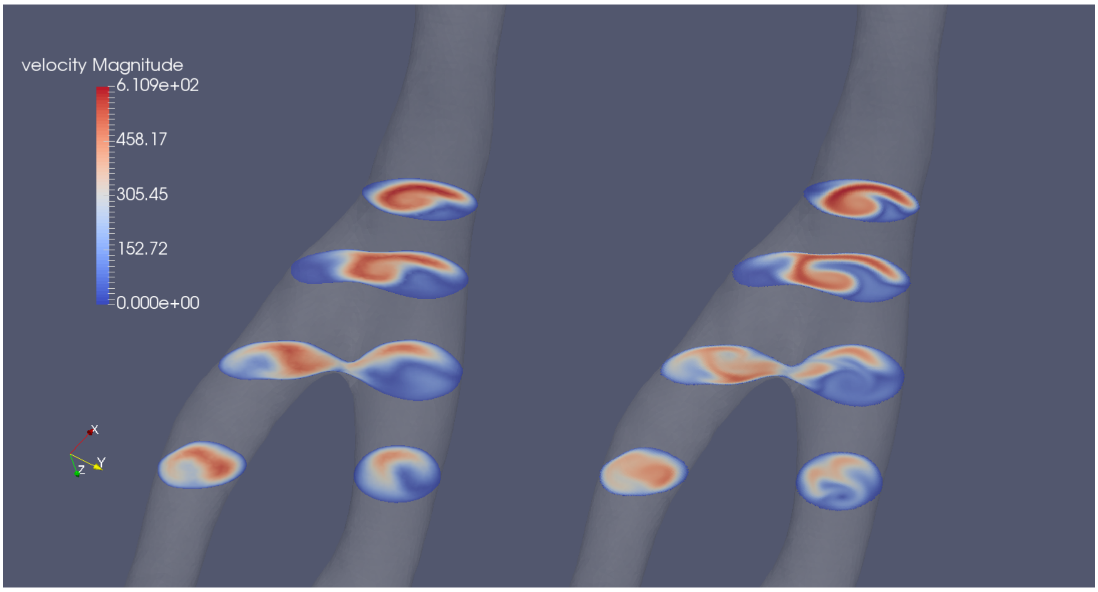

Figure 4.7: Left: a plot of the velocity magnitude $(\mathrm{mm/s})$ in two planes near the bifurcation with results from SimVascular. Right: the same plot by LBM, case 4.

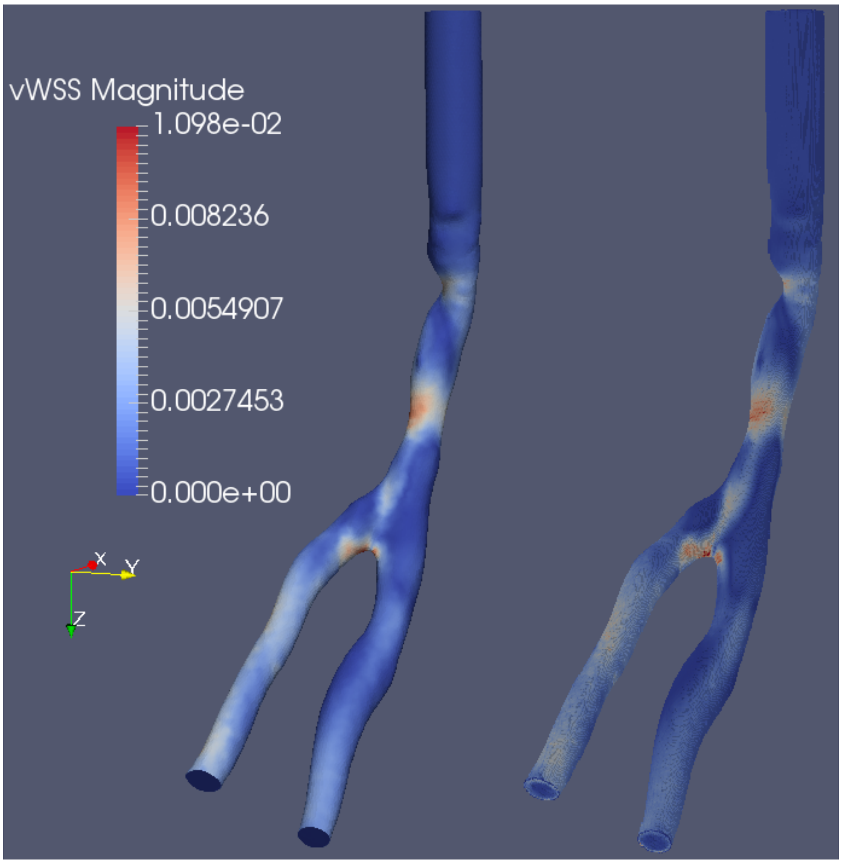

Figure 4.8: Left: a plot of the wall shear stress $(\mathrm{kg/mm \cdot s^2})$ by SimVascular. Right: the same plot by LBM, case 4.

5 | Unassisted breathing: Case description and methodology

Unassisted breathing is the case when there is no additional air supply. This chapter studies the case of unassisted tidal breathing, which is of interest since it can be used to study the influence of the nasal high flow therapy by comparing flows with and without therapy. It is useful to know how the air flows in the specific geometry used, since the air flow changes for every individual. Insight of the flow behaviour in the geometry is also helpful since NHFT experiments are also performed in this geometry.

5.1 Geometry

The geometry of the human nasal cavity is quite complex. The external nose, which is the visible part of the nose, is generally only a third of the entire nasal cavity [64]. The nasal cavity as a whole consists of two chambers which are approximately $50\ \mathrm{mm}$ high and $100\ \mathrm{mm}$ long, making up for a total surface area of approximately $15000\ \mathrm{mm}^2$ and a total volume of 15 ml. The nose is enclosed with sinuses, that under normal circumstances are filled with air that undergoes a full change every few hours [76]. The airflow in the nose is controlled mostly by the shape of the internal passages [92]. The geometry that was used in this thesis was obtained from Embodi3D [18]. The geometry itself is created from the CT-scan of an adult male with closed mouth. A stereo-lithographic file (STL) was send with permission to modify and use for non-commercial purposes. An overview of the geometry with some intersection planes can be seen in 5.1. The geometry of the nose is not symmetric. The right nostril has an area of 117.68 mm^2 and the left nostril has an area of 129.62 mm^2. The trachea boundary is regarded as an ellipse. Its area is 180.35 mm^2. Cross sectional areas of the intersections as shown in figure 5.1 are listed in table 5.1. It should be noted that it is not always possible to make a clear division between the nasal cavities and the sinuses. The table therefore lists the total area, as shown in the figure, and a detached total area which is estimated without some (or all) sinuses if possible. The detached area is then split in a left and right part.

Table 5.1: Areal information of the planes described in figure 5.1. An asterisk indicates that the detached area is the area without the ethmoid and or frontal sinuses and bold text indicates that the detached area is without the maxillary sinus

Plane	$V1$ *	$\mathbf{V2}$	$\mathbf{V3}$	$\mathbf{V4}$	$\mathbf{V5}$*	$V6$*	$V7$*	$V8$*	$V9$*	$V10$
Total cross sectional (mm^2)	766	832	2000	1985	1488	805	834	882	724	287
Detached cross sectional area (mm^2)	360	596	821	769	352	282	323	421	469	287
Cross sectional area Left cavity (mm^2)	184	275	392	352	200	150	172	222	-	-
Cross sectional area Right cavity (mm^2)	176	321	449	417	152	132	151	199	-	-

5.2 Experimental set-up

Numerical simulations are performed parallel to experiments. The geometry described in section 5.1 is also used in the experiments. The geometry is 3D-printed using Selective Laser Sintering (SLS) with PA 12 nylon. Afterwards, the model was impregnated to prevent air leakage. Airflow is generated by a lung simulator that is connected to the trachea. The simulator consists of a linear motor (LinMot PS01-37Sx120F-HP-N) rigidly connected to a pneumatic cylinder (Parker P1D-S063MS-0320). Cylinder position is monitored via a magnetic sensor (Parker P8SAGACHH). The flow rate is determined by calculating the cylinder position multiplied with the piston's cross-sectional area to time. Pressure was tracked at several tabs in the geometry. An overview of the pressure tabs can be seen in figure 5.2. Experimental pressures are measured at the wall location of the pressure taps using two pressure scanners (NetScanner 9116, capacity of $\pm 1\mathrm{psi}$

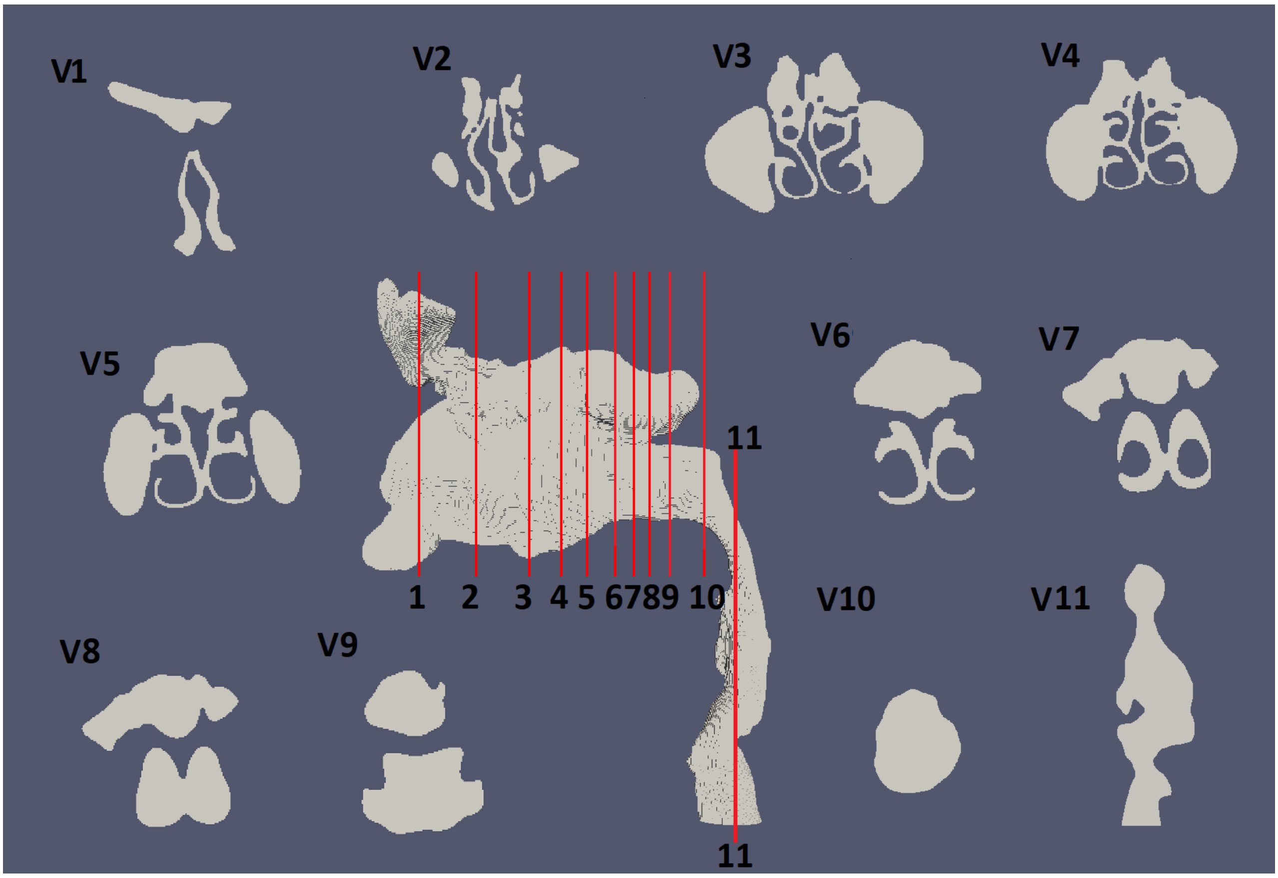

Figure 5.1: Several intersection planes in the nasal geometry, posterior view

and an accuracy of 0.05% FS, with the sampling frequency set to 167 Hz). Numerical pressures are measured in the middle of the geometry.

5.3 Breathing profile

The breathing of a human occurs in breathing cycles that consist of an inhalation and an exhalation part. This breathing profile differs per person. Factors of diversity are the inspiratory and expiratory duration, tidal volume and the flow profile [6]. A breathing profile (which can be found in figure 5.3) was obtained, consisting of 499 data points both in time and in volume flow rate. Similar profiles are used by Hove et al. [31] and Adams et al. [1]. The inhalation volume flow rate is depicted in blue and the exhalation volume rate in red. Notice that inhalation flow rate is regarded as a negative flow rate. The period of the breathing profile is 4 seconds. The tidal volume is 450 mL and the minute volume is 5.625 $\mathrm{L/min}$. Exhalation takes 2.216 seconds. The maximum volume flow during exhalation is 16 $\mathrm{L/min}$ which occurs at 1.168 seconds, the average volume flow during exhalation is 12.14 $\mathrm{L/min}$. Inhalation takes 1.784 seconds, with a maximum negative flow rate of -22.13 $\mathrm{L/min}$ at 0.98 seconds. The average volume flow rate during inhalation is -15.07 $\mathrm{L/min}$.
The breathing profile can be modelled by splitting it in an inhalation part and an exhalation part. The boundary conditions have to change corresponding to the type of breathing that occurs. There are four boundaries: the wall, the trachea and both nostrils. The wall of the geometry is regarded as a no slip boundary.

5.3.1 Expiration boundary conditions

During exhalation, the boundary conditions at the nostrils are set to a zero pressure outlet. The inflow is provided through the trachea. A prescribed velocity profile is needed at the trachea. Several studies on the velocity profiles in the trachea can be found in the literature. Elcner et al. [17] studied the velocity profiles in an idealized model of human respiratory tract. An experimental model was used as well as a numerical model. The velocity profiles that were obtained showed most resemblance with a fully developed flow, though turbulent behaviour was experienced. Xu et al. [106] investigated inhalation and exhalation flow patterns in a realistic human upper airway model by PIV experiments and CFD simulations. The velocity profiles of four planes in the tracheal area were investigated, and the flow behaviour showed very much

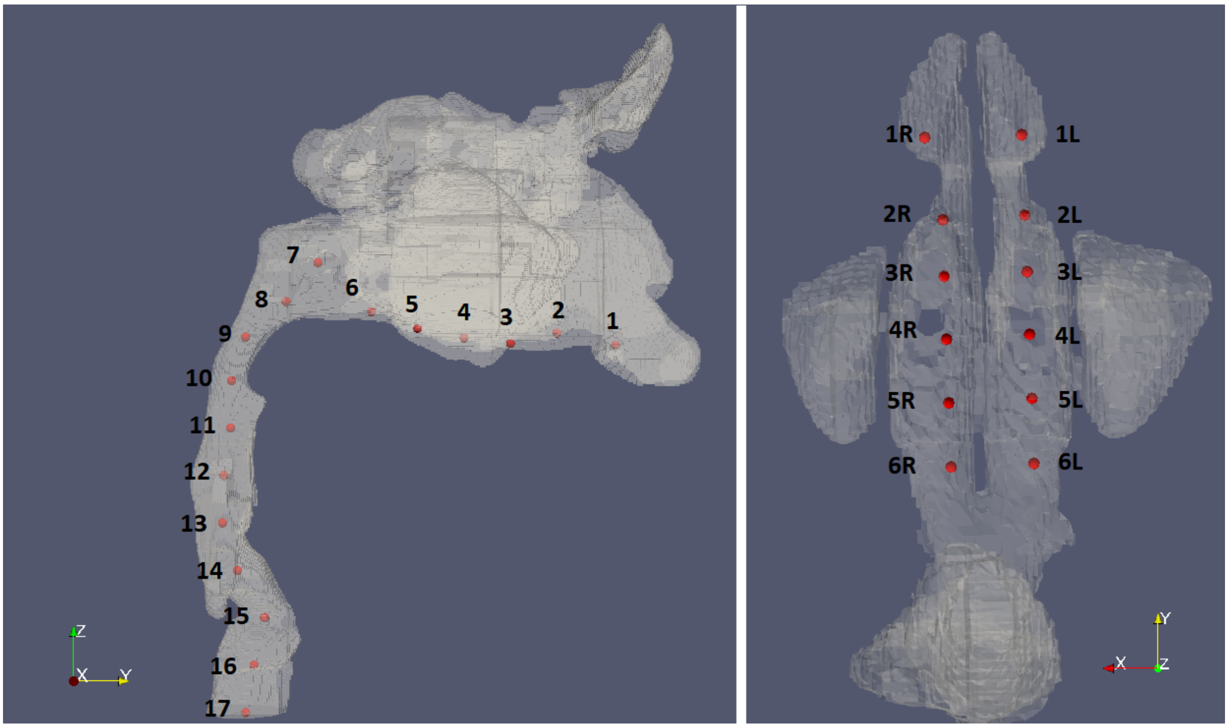

Figure 5.2: Overview of the pressure tabs in the geometry. The tabs with numbers 1-6 have a left and a right component.

resemblance with a developing flow. Though the velocity profile at the highest cut plane showed that the flow is not fully developed, the position of this plane is lower than the boundary in the model used in this work.
Since the air has to cover a relatively large distance after that from to the end of the trachea, it is decided that a fully developed flow profile is the most appropriate velocity boundary condition. Zero pressure outlets were prescribed at the nostrils.

5.3.2 Inspiration boundary conditions

Inhalation is harder to model than exhalation. Doorly et al. [14] found experimentally that the nostrils act as a sinkhole, drawing air uniformly towards the nostril. In numerical models of the inflow of the nose, several different methods are used. The most common inflow boundary conditions are compared by Taylor et al. [92]. Included in their study are a flat velocity profile inlet, a flat and parabolic profile at the entrance of a convergent pipe to the nostrils and a pressure boundary condition at the nostril that included the external face and environment allowing the flow to develop naturally towards the nostril. It was concluded that the use of different boundary conditions affect the flow through the nasal cavity, but the level of sensitivity is low for qualitative flow patterns and gross flow measures. Therefore, a uniform velocity profile at the nostrils is used as a boundary condition at the inlets, and a zero pressure outlet is used at the outlet. Both the inlet and outlet were extended to prevent numerical difficulties, which are discussed in more detail in section 5.7. The prescribed boundary conditions results in one unknown: the volume flow ratio between the two nostrils. Studies use either the same flow rate in both nostrils or an extended single inlet that is merged from both nostrils [32, 43, 104, 112]. The geometry used in this study shows some differences between the left and right nasal cavity, especially in the inlet nostril area. Therefore a new approach has been used. The flow ratio is obtained by requiring that the pressure at both nostrils is the same. A relation between the pressure and the volume flow rate is therefore needed, which is discussed in the next section.

5.4 Volume flow rate ratio estimation during inhalation

As discussed in the previous section, the ratio between the volume flow at the nostrils is unknown during unassisted inhalation. Physically, it makes most sense that the pressure at the nostrils are the same as they are connected to the atmospheric pressure of the surroundings.

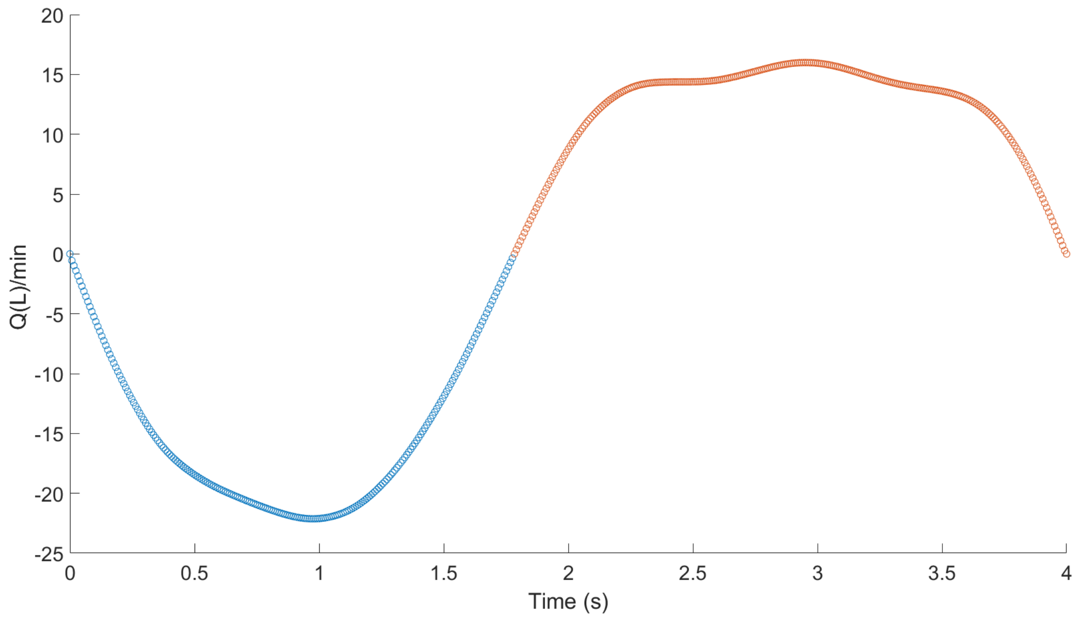

Time(s)	0.2	0.4	0.6	0.8	1.0	1.2	1.4	1.6	1.8	2.0
L/min	-10.17	-16.74	-19.63	-21.34	-22.11	-20.29	-15.33	-8.02	0.72	8.76

Time(s)	2.2	2.4	2.6	2.8	3.0	3.2	3.4	3.6	3.8	4.0
L/min	13.34	14.37	14.53	15.52	15.94	14.91	13.92	12.96	8.78	0

Figure 5.3: Data points used to model the breathing profile. In blue (negative) inhalation volume flow rate, in red the exhalation volume flow rate. The flow rate in liters per minute over time are also listed.

5.4.1 Approach

The ratio of flow between the nostrils is not constant, but is dependent on the total inflow. It is therefore needed to obtain a relation of the flow ratio between the nostrils as a function of the total inflow. It is only possible to estimate this relation via scaled problems due to the amount of computational resources. It is therefore decided that the convergent behaviour of the flow rate ratio is also investigated to take into account the change in going from a coarse grid to a fine grid. A total of 27 simulations were performed to obtain the flow rate relation. Three different grid sizes were used, having 12267107, 18447075 and 29494741 cells. On each grid, three different constant volume flow rates were used, which were limited due to the amount of computational resources available to ($1\mathrm{L/min}$, $1.5\mathrm{L/min}$ and $2\mathrm{L/min}$).
Combining the volume flow rate and the grids make up nine different cases. With these nine cases, it is possible to study the influence of the grid size and the influence of the volume flow rate on the volume flow rate ratio in the nostrils. All cases were ran until they reached a steady state. At each case, an initial guess for the volume flow rate was made. With that result a second guess was made. Finally, a third guess by interpolation ensured that a maximum pressure difference of 0.007% was obtained at the nostrils.

5.4.2 Results

The obtained percentage of the total volume flow rate for the left nostril can be found in table 5.2. With these values, two fits were made. For the convergence of the ratio (the relation between the grid size and the ratio) a power law fit was obtained with a convergence exponent of 12. A relation between the volume flow rate and the volume flow rate ratio was not directly evident. The two grids with the most cells show very linear behaviour, but the lowest resolution grid does not. This could however be caused by having a grid that is too coarse. It is therefore concluded that the linear relation of the finest grid will be used, but with an extra damping implemented in the ratio curve. The damping is added, since it can be deducted that a linear relation between the volume flow rate and the volume flow rate ratio is not physical as it is then mathematically possible that the volume flow in a nostril exceeds 100%. By linear extrapolation, the flow rate between the nostrils at peak inspiration was calculated to be 86:12. Such ratios are not seen anywhere in literature [4, 47, 109]. Therefore, a damped variation of the linear profile was constructed based on common sense and with conservation of the ratios obtained for the finest grid in table 5.2. This damping profile ensures that the maximum flow rate in the left nostril during peak inspiration is 62%. The curve for the percentage of volume flow as function of the total flow can be seen in figure 5.4.

Table 5.2: The percentage of volume flow rate through the left nostril with respect to the grid size and volume flow rate.

Grid size \ Volume flow rate	2 L/min	1.5 L/min	1 L/min
12267107 cells (h = 20 mm)	49.34 %	49.25 %	48.50 %
18447075 cells (h = 17.5 mm)	50.87 %	50.14 %	49.41 %
29494741 cells (h = 15 mm)	51.12 %	50.35 %	49.59 %

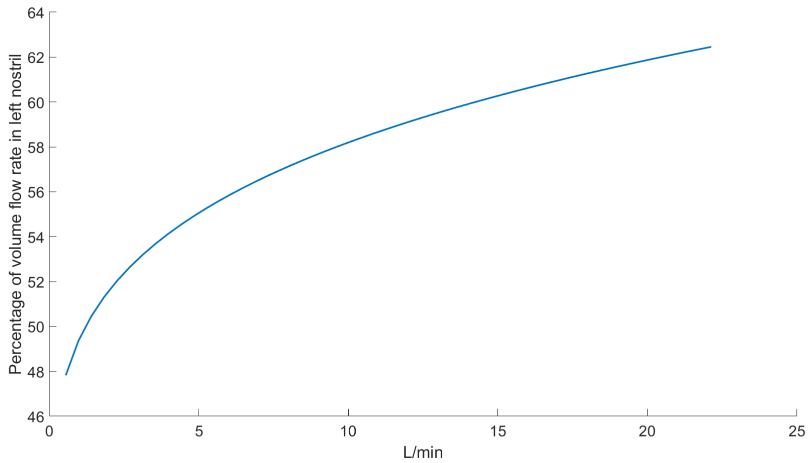

Figure 5.4: Curve of the percentage flow of the total volume flow in the left nostril per flow rate.

5.5 Flow and simulation parameters

The fluid properties of the air are chosen similar to the research by Brüning et al. [11] where the density $\rho = 1.180$ $\mathrm{kg/m^3}$ and dynamic viscosity $\mu_{phy} = 1.86 \cdot 10^{-5}$ $\mathrm{Pa \cdot s}$, which correspond with air properties at approximately 25 degrees Celsius. Reynolds numbers are calculated at the trachea, at the nostrils and at the transition plane between the nasopharynx and orophanyx, as illustrated in figure 5.5. The Reynolds number will be calculated using the average velocity magnitude on the plane and the hydraulic diameter as:

$$Re = \frac{\rho U_{phy,avg} D_h}{\mu_{phy}} \tag{5.1}$$

The hydraulic diameter of the trachea, regarded as an ellipse, is calculated by [79] :

$$D_{h,Tra} = \frac{4ab(64 - 16e^2)}{(a+b)(64 - 3e^4)} \qquad \text{with} \qquad e = \frac{a-b}{a+b} \tag{5.2}$$

With a the semi-major axis diameter and b the semi-minor axis diameter. The hydraulic diameters of the left and right nostrils are estimated to be 14 mm and 10 mm respectively. The hydraulic diameter at the pharynx is estimated to be 12.5 mm and its area is determined to be 124.709 mm^2. The lattice Mach number is calculated as:

$$Ma = \frac{U_{phy,max} \cdot \Delta t}{h} \tag{5.3}$$

with $U_{phy,max}$ the maximum velocity magnitude at peak exhalation/inhalation and Δt and h the physical time step size and grid spacing.

A multi-relaxation model with a Large-Eddy Scale (LES) turbulence model is used for the Lattice Boltzmann simulations. This was implemented due to stability reasons, as it turned out that high Reynolds and lattice Mach numbers caused divergence in the simulations with a single relaxation model or with DNS. To reduce the lattice Mach number, either h or

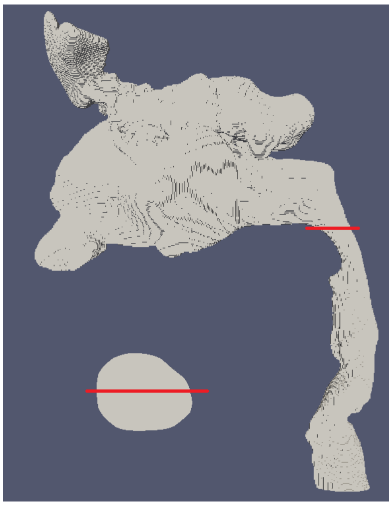

Figure 5.5: Plane in the pharynx where Reynulds number is monitored.

τ has to be chosen lower. From experience, with the BGK single-relaxation model, the lowest limit for τ is approximately $\frac{1}{1.9}$ while τ with multi-relaxation and a LES turbulence model sometimes can reach values of approximately $\frac{1}{1.95}$ which makes a big difference in the allowed maximum velocities on the grid. This can mathematically be supported when calculating the maximum velocity in which the upper Mach limit does not reach more than 0.1. The maximum velocity can be calculated by using the equation for the Mach number (equation 5.3), which gives by rewriting and substitution of Δt, written in the flow parameters (see also section 2.3.2), the following equation:

$$Ma = \frac{U_{max}(\tau - 0.5) * h}{3 * \nu_{phy}} \tag{5.4}$$

This equation can be rewritten in dimensionless groups:

$$\frac{U_{max} \cdot h}{\nu_{phy}} \cdot \frac{1}{Ma} = \frac{3}{(\tau - 0.5)} \tag{5.5}$$

Where the first group can be seen as the cell Reynolds number. Remember that $0.5 \leq \tau \leq 1$, which results in the asymptotes at $\frac{U_{max} \cdot h}{\nu_{phy}} \cdot \frac{1}{Ma} = 6$ and $\tau = 0.5$. The graph can be seen in figure 5.6. Decreasing τ from $\frac{1}{1.9}$ to $\frac{1}{1.95}$ causes an increase in 105% on each side of equation 5.5. This means that the maximum velocity allowed on the grid with a given Mach number limit is 105% higher, if the same grid size and kinematic viscosity is implemented.

The Multi-relaxations parameters are calculated from the single-relaxation parameter, which is set to be $\frac{1}{1.95}$, using the same procedure as used by Tölke et al. [94]. A LES turbulence model is used as described in 2.3.1. The Smagorinsky constant is set to be 0.17, which is the default setting in the code.

5.6 Grid convergence

A grid convergence study shows the convergence of the flow parameters for changing h. Variables such as pressure and velocity often converge slower in practice than the theoretical order of convergence. A complete grid convergence study has not been conducted, due to the high Reynolds numbers and lattice Mach numbers in the case. On coarse grids, the simulations diverge due to Mach numbers exceeding 0.3. Changing the lattice parameters will not help converging in this case. The estimated coarsest grid possible to perform simulations with the flow rates described is somewhere between 500 and 700 million cells, providing that LES turbulence model is used with relaxation parameter almost equal to 0.5. Due to a shortage of time and resources, a scaled breathing profile (which is 8 times smaller) is used to show some small insights in the convergent behaviour. The behaviour is studied for mesh sizes with a grid spacing of $h = 0.20, 0.175, 0.15, 0.125, 0.10, 0.09, 0.075\text{mm}$ which corresponds with mesh sizes of 12.2M , 18.4M, 29.5M , 51.3M , 101M, 139M and 241M. Graphs of the pressure and the velocity magnitude in pressure tab point 11 over time for the chosen grids can be found in Appendix B. It can be noted that, for the coarsest grids, unstable wobbling behaviour occurs during the transition from inhalation to exhalation.

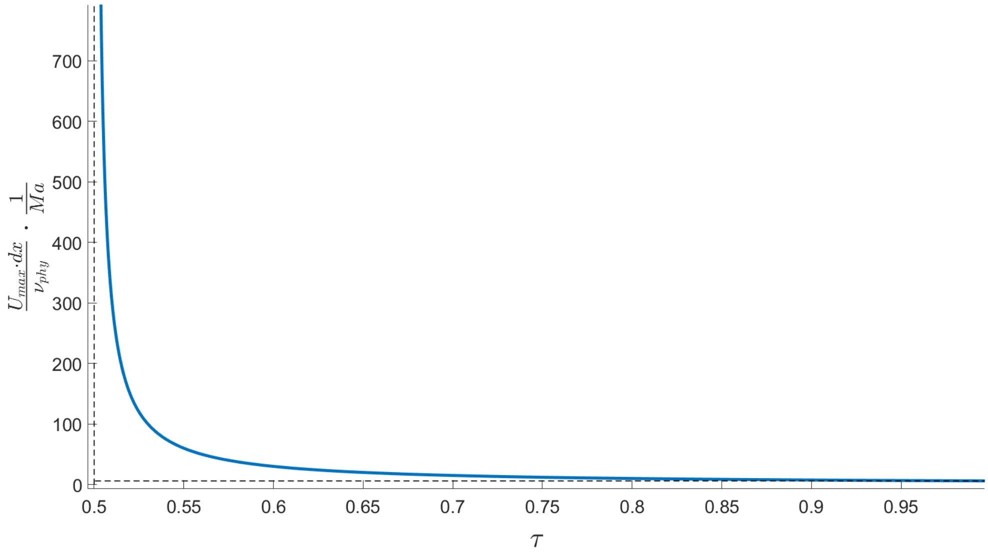

Figure 5.6: Asymptotic relation between τ and the dimensionless group $\frac{U_{max} \cdot dx}{\nu_{phy}} \cdot \frac{1}{Ma}$.

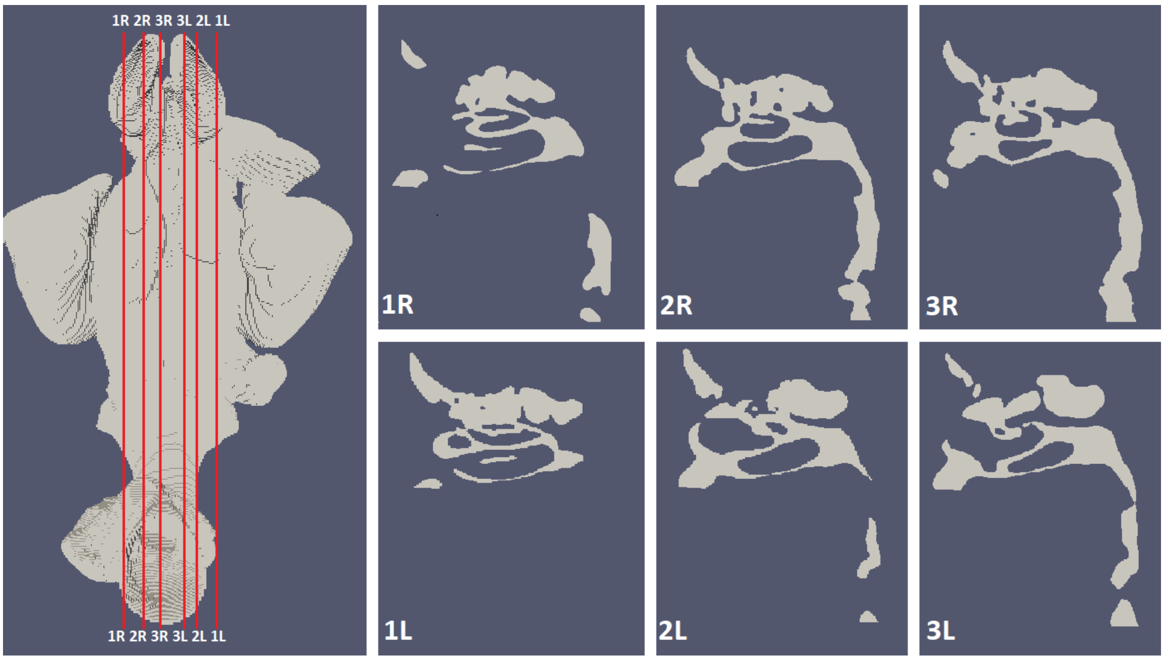

Figure 5.7: Several slices in the geometry where the flow is monitored.

The L_1 norm is calculated for the pressure relative to the pressure in the nostril boundary and the velocity magnitude, where the L_1 is defined as the mean of the sum of the absolute differences between the flow parameters on the grids and the flow parameters on the finest grid ($h = 0.075$ mm) on each time step:

$$L_1 = \frac{1}{N} \sum_{t=1}^{N} (|U_t - U_{t,0.075}|) \tag{5.6}$$

The results are plot in figure 5.8 and 5.9. It can be seen that the pressure norm decreases linear for most of the time, but then seems to slow down a bit more at the higher resolutions. The opposite happens at the velocity convergence plot, which is unexpected. However, this behaviour can be caused by the wobbling behaviour in the velocity magnitude near the transition from inhalation to exhalation at low resolution.

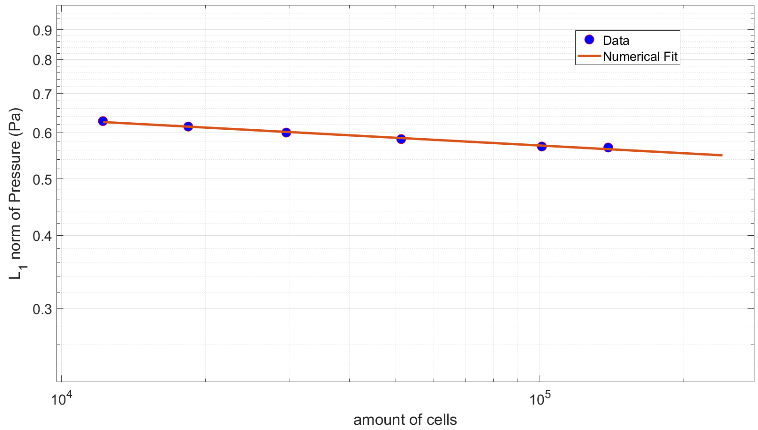

Figure 5.8: L_1 (Pa) norm of the pressure.

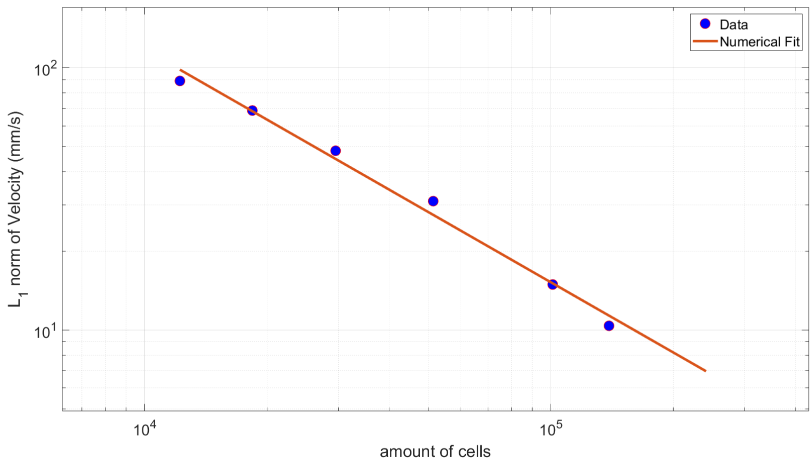

Figure 5.9: L_1 norm $(\mathrm{mm/s})$ of the velocity magnitude.

5.7 Mesh configuration

Normally, a grid is chosen based on the spatial discretization error. The finer the grid, the lower the error but the higher the computational costs. In this case, the grid spacing h has to be sufficiently low to prevent lattice Mach numbers to become too high. Based on the lattice parameters and the Mach numbers obtained from the scaled breathing profile, a grid spacing of $h = 0.048\ \mathrm{mm}$ has been chosen. With this h and the chosen τ of $\frac{1}{1.95}$, the maximum velocity in which the Mach number is less than 0.1 is $U_{max} < 7684\ \mathrm{mm/s}$. For Mach numbers less than 0.15, $U_{max} < 11526\ \mathrm{mm/s}$. Though no strong statements can be made, it can be mentioned that Lintermann et al. [47] obtained resolved grids with the cell size of 0.10 to $0.086\ \mathrm{mm}$ in a study that uses the Lattice Boltzmann method to simulate inspiration in the nasal cavities.

The configuration of the trachea outlet and the nostril inlet proved to be prone to numerical issues during inhalation simulations. At the trachea, locally very high velocities were observed, as can be seen in figure 5.10. This most likely occurs due to turbulent flow with high velocity and vorticity at the boundary, and was resolved by extending the outlet. At the inlets (nostrils), another numerical issue was observed. A reason for this behaviour might be that the outer cells of the inlet are almost completely surrounded by walls. This problem was also resolved by extending the inlet. Extending the nostril inlet has also been described and investigated in the inflow boundary conditions study at the nostrils conducted by Taylor et al. [92].

The extended inlet was purposely kept short to keep the flow as uniform as possible at the start of the nostrils. The velocity profile at the left nostril entrance can be seen in figure 5.11, which still shows reasonable agreement with a uniform flow.

Exhalation is performed without any major adjustments to the geometry, though a small unevenness in the mesh was removed. The mesh with extended inlet and outlet has 1037M cells, without extensions the mesh has 925M cells. A coarse mesh (4M cells) was made to illustrate the meshes with and without the extensions, which can be found in appendix C.

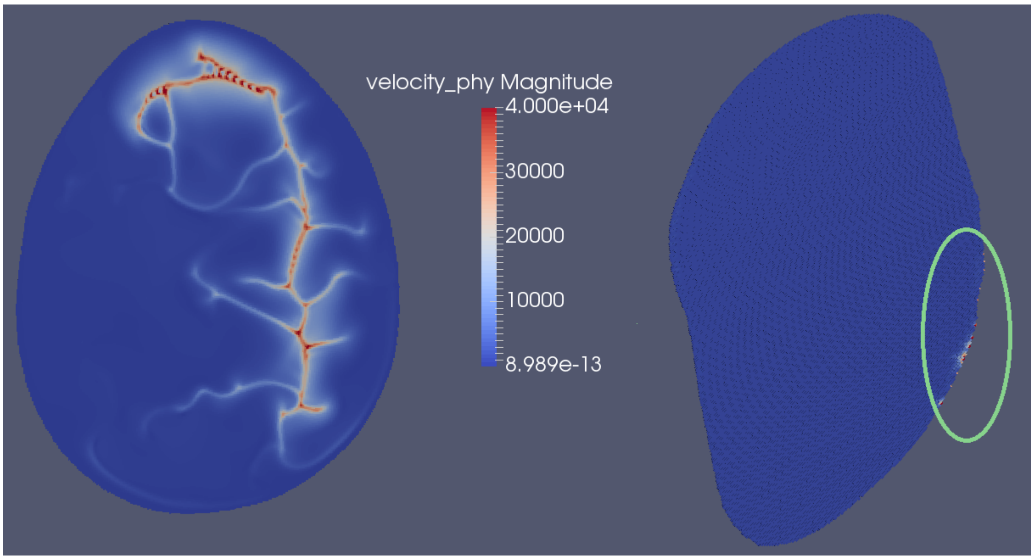

Figure 5.10: Numerical issues at the trachea outlet and nostril inlet.

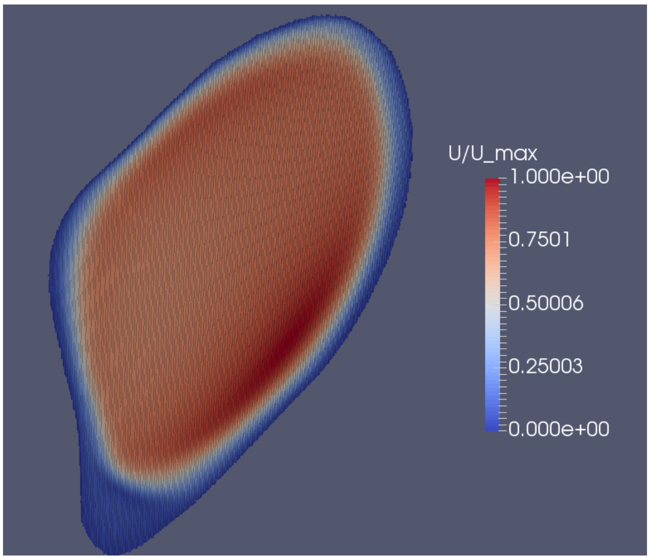

Figure 5.11: Normalized velocity at the entrance of the nostril with the extended inlet.

5.8 Last notes

Extracting and analyzing the results of all cells was not possible with the resources used due to its size. It is therefore that solutions are monitored at several intersection planes in the geometry and the points as can be seen in figure 5.2. It should be noted that, due to a typographical error the coordinate of tracking point 11, as depicted in 5.2, is placed 10 mm higher than intended, influencing the comparison between the experimental measurements and numerical results. The intersection planes that are monitored are the planes in 5.1, the planes depicted in figure 5.7, the boundaries and 10 xy-planes at different z-coordinates.
To prevent numerical issues during the exhalation curve, an additional pressure term was introduced. This causes a relative pressure solution, that can only be compared with the literature and the experiments when made dimensionless.

6 | Lattice Boltzmann method in unassisted breathing

The case description and methodology that is used to simulate unassisted breathing was elaborated on in chapter 5. This chapter shows and discusses the results of the LBM simulations. All simulations are performed on supercomputer Cartesius using 200 nodes with 24 cores. Simulations were split into smaller parts of 0.15 s, which take approximately 5 hours on the 4800 cores. Pressure was measured in the experiments, where the pressure was taken at the pressure tap points relative to the nostril pressure. The relative pressure in the numerical study is therefore defined as:

$$\Delta P = P_i - P_{nostril} \tag{6.1}$$

With P_i the pressure at a certain point in the geometry and $P_{nostril}$ the mean of the pressures obtained at the outlet of the nostrils. Note that this relative pressure is equal to the pressure drop from the nostril to a point i during inhalation. Calculated pressure results can be normalized by dividing the pressure of a pressure tab point by the pressure at point 17 (the trachea):

$$\Delta \bar{P} = \frac{P_i - P_{nostril}}{P_{17} - P_{nostril}} \tag{6.2}$$

6.1 Inhalation

The inspiration part of the breathing cycle takes up 1.78 s of the total breathing cycle. Peak inspiration occurs at 0.98 s with -22.13 $\mathrm{L/min}$. During peak inspiration, the velocity inlet in the left and rights nostrils are 1589 $\mathrm{mm/s}$ and 1071 $\mathrm{mm/s}$ respectively. This corresponds with approximated Reynolds numbers of 1411 and 680 for the left and right nostril. The velocity magnitude at the vertical cut planes in the nasal cavity during peak inspiration can be seen in figure 6.1. Maximum velocity magnitudes observed at these planes are listed in table 6.1. During inspiration, the flow accelerates in the z-direction at the nostrils due to narrowing of the nostril geometry. Measured over 19 time steps, the flow reaches an average maximum velocity of 1.97 times the inlet velocity in the left nasal valve and an average maximum velocity of 2.76 times the inlet velocity in the right valve.

Table 6.1: Maximum velocity magnitude during peak inspiration on different intersection planes as described in 5.1.

Plane	V1	V2	V3	V4	V5	V6	V7	V8	V9	V10
Maximum velocity magnitude ($\mathrm{m/s}$)	3.57	3.71	3.70	3.31	3.06	3.03	2.94	2.74	2.69	3.52

It can be seen that the flow in the left nasal valve reaches the upper part of the valve more than the flow in the right valve. The maximum velocity throughout the nasal cavity decreases slowly, but stays in the order of magnitude. Some flow separation and shear layer forming is observed in the lower front part of the ethmoid sinus and in the olfactory region, caused by a small jet like flow, best seen in figure 6.2, figure 6.4 and figure D.4. Past the conchae, the flow starts to accelerate towards the pharynx, due to the narrowing geometry. This also causes a rapid increase in the pressure drop at the pharynx. At the pharynx, a large jet is observed. This jet causes flow separation at the boundaries with recirculating flow at the anterior side. Big vorticity magnitude due to shear layer flow are observed in the length of the jet. The Reynolds number at peak inspiration in the pharynx is calculated to be 4356. After the nasopharynx, the geometry diverges again at the oropharynx before entering the larynx. The combination of a narrowing geometry at the larynx and some impinging at the wall of the oropharynx just above the larynx causes a very small jet with locally high magnitudes in velocity and vorticity. The maximum velocity observed is 11.2 $\mathrm{m/s}$, which results in a local maximum mach number of 0.146. This is also the maximum velocity observed in the whole inspiration simulation. The turbulent jet behaviour causes the vorticity and turbulence at the initial outlet. It is this behaviour that causes the outlet to be extended.

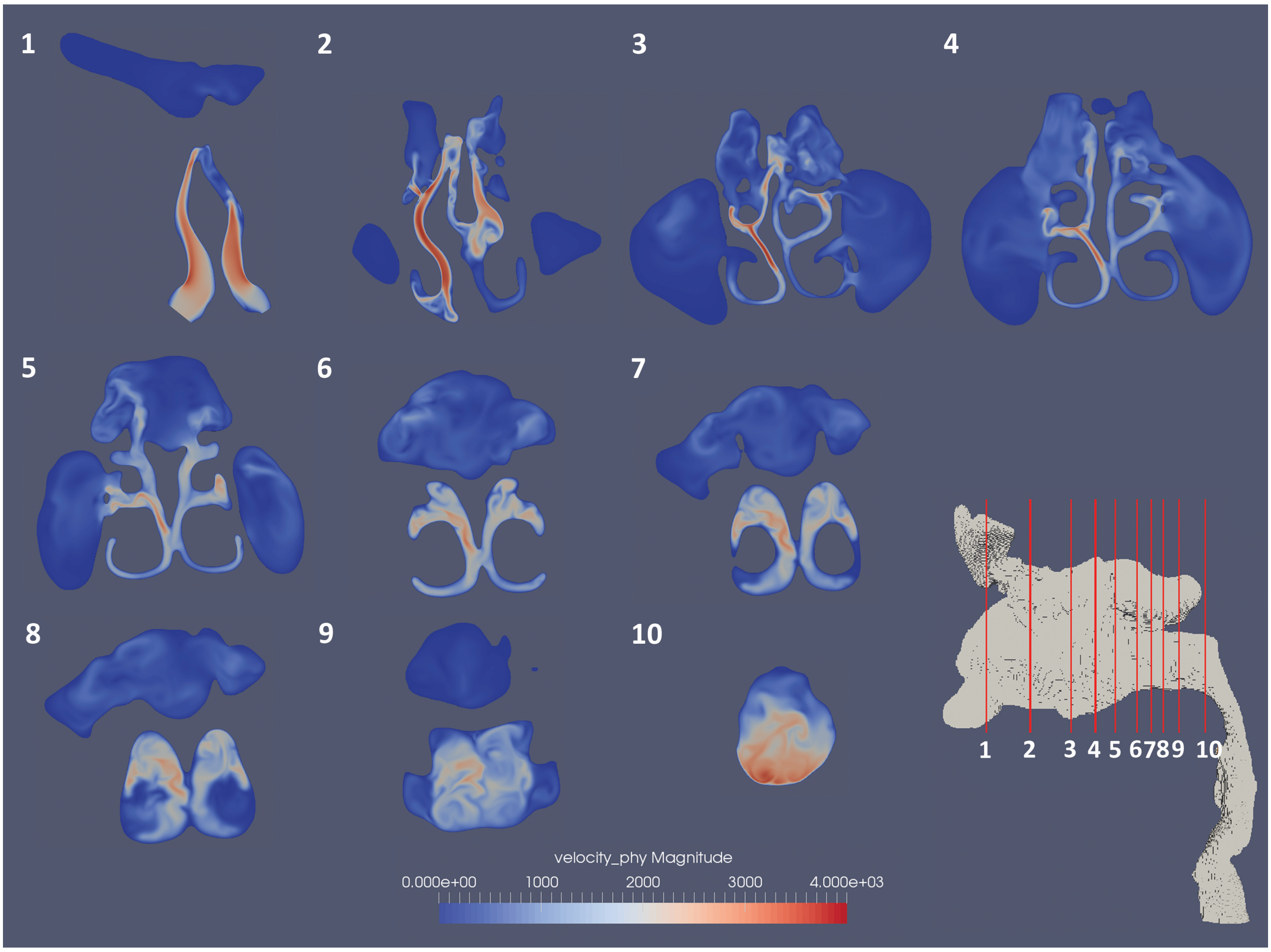

Figure 6.1: Velocity magnitude $(\mathrm{mm/s})$ at several planes during peak inhalation $(22.13\ \mathrm{L/min})$.

Table 6.2: Numerical results of the maximum, mean and 99th and 95th percentile of the velocity magnitudes in the 3R, 3L and V11 plane during inhalation.

		mean vel mag $(\mathrm{mm/s})$			max vel mag $(\mathrm{mm/s})$			99th percentile $(\mathrm{mm/s})$			95 percentile $(\mathrm{mm/s})$		
t(s)	$\mathrm{L/min}$	3R	3L	V11	3R	3L	V11	3R	3L	V11	3R	3L	V11
0.25	-12.4	774	851	1311	4300	5300	5066	3322	4022	4144	2233	3677	3177
0.35	-15.6	1054	1097	1853	5593	7125	7679	4241	5142	5446	3147	4659	4266
0.45	-17.8	1233	1266	1999	6599	8211	7888	4911	5888	6400	3466	5288	4722
0.65	-20.2	1400	1488	2366	6866	9766	9399	5388	6888	6711	3799	6144	5366
0.85	-21.7	1400	1511	2444	7244	9422	9577	5477	7088	7055	3855	6399	5500
0.9	-22.0	1477	1522	2455	7055	1.03e+4	1.09e+4	5644	7222	7377	4120	6355	5777
0.95	-22.1	1488	1444	2399	7766	1.12e+4	1.12e+4	5622	7155	7911	4144	6211	5833
1.05	-21.9	1466	1488	2199	7777	1.09e+4	1.09e+4	5677	7255	7200	4099	6399	5377
1.25	-19.2	1288	1300	2166	6322	9077	9922	4966	6244	6322	3611	5544	4977
1.45	-13.5	896	969	1522	4388	6455	6244	3622	4666	4511	2688	4133	3622
1.65	-5.65	363	439	621	2055	2699	2377	1600	2200	2011	1077	1922	1577

The Reynolds number at the (original) trachea is calculated to be 2826. The vorticity and velocity magnitude plots of the jets in can be seen in figure 6.2 and 6.3. The velocity vector field was plot in figure 6.4 by using Line integral convolution. Clear flow recirculation can be seen near the jets, which is supported by plots of the speed in z-direction as can be found in figure D.3. The mean, maximum and 99th and 95th percentile of the velocity magnitudes are listed for the 3R, the 3L and the V11 plane in table 6.2. The 99th percentile and 95th percentile are listed for literature comparison reasons as the maximum velocities are very local and dependent on the turbulent behaviour of the flow and might be damped out in some turbulence models. The mean and maximum velocity at the pressure tab points are listed in table 6.3 .

Table 6.3: Numerical results of the maximum and mean velocities during inhalation at pressure tab points.

Point	velocity magnitude $(\mathrm{m/s})$	
	Maximum	Mean
1R	1.70	1.09
1L	2.25	1.41
2R	0.37	0.21
2L	1.57	0.78
3R	0.29	0.18
3L	1.40	0.80
4R	0.21	0.15
4L	1.37	0.77
5R	0.63	0.41
5L	1.00	0.63
6R	1.16	0.74
6L	1.53	0.96

Point	velocity magnitude $(\mathrm{m/s})$	
	Maximum	Mean
7	2.50	1.21
8	2.57	1.76
9	5.04	3.48
10	6.43	4.38
11	6.39	4.37
12	6.56	4.21
13	5.47	3.55
14	4.04	2.38
15	5.61	3.72
16	6.00	3.55
17	2.47	1.41

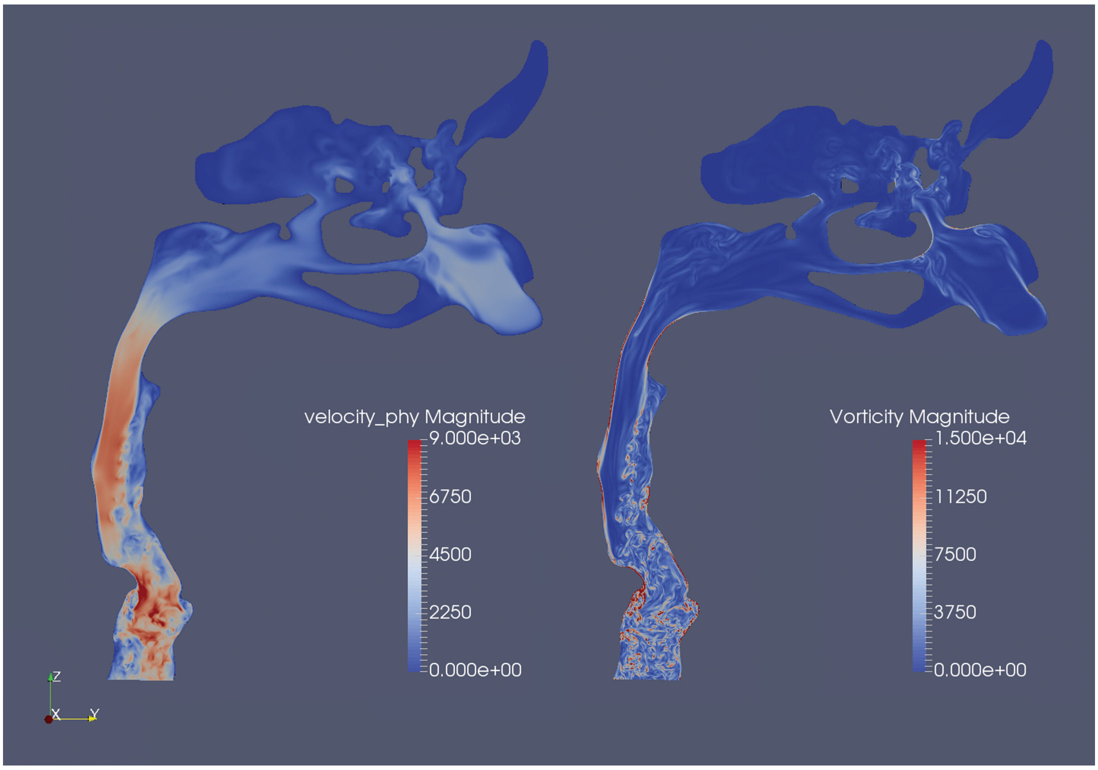

Figure 6.2: Velocity magnitude $(\mathrm{mm/s})$ and vorticity magnitude $(1/\mathrm{s})$ in cross section 3R as defined in 5.7 at peak inspiration.

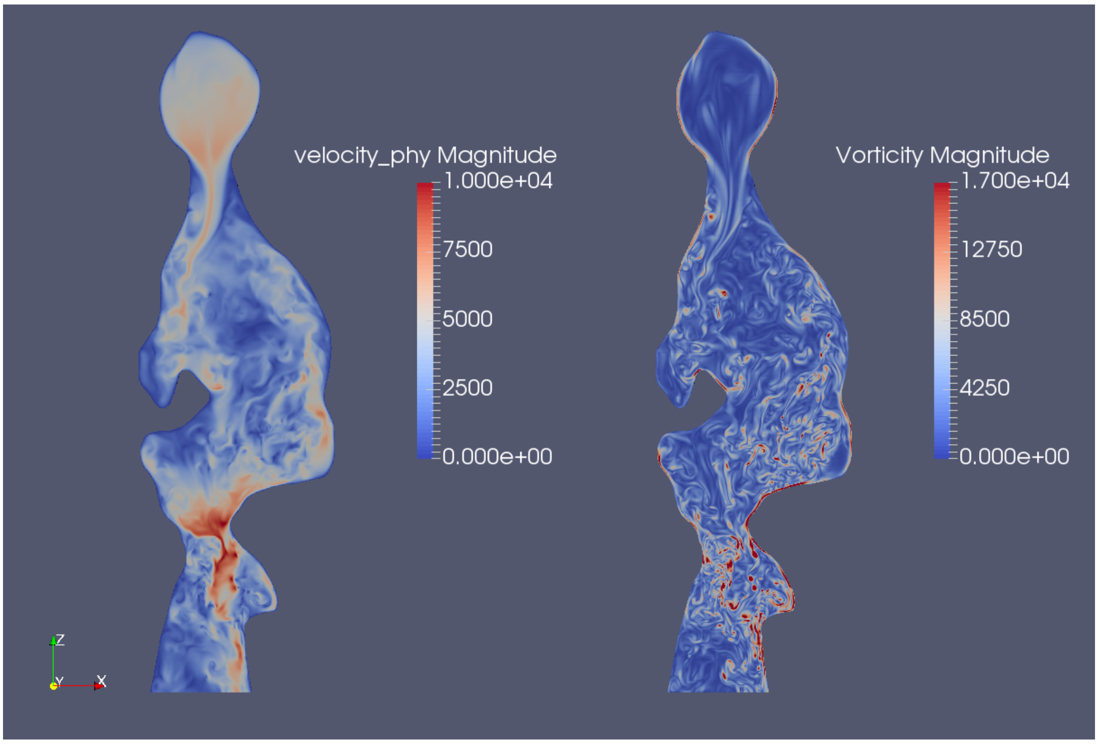

Figure 6.3: Velocity magnitude $(\mathrm{mm/s})$ and vorticity magnitude $(1/\mathrm{s})$ in cross section V11 as defined in 5.1 at peak inspiration.

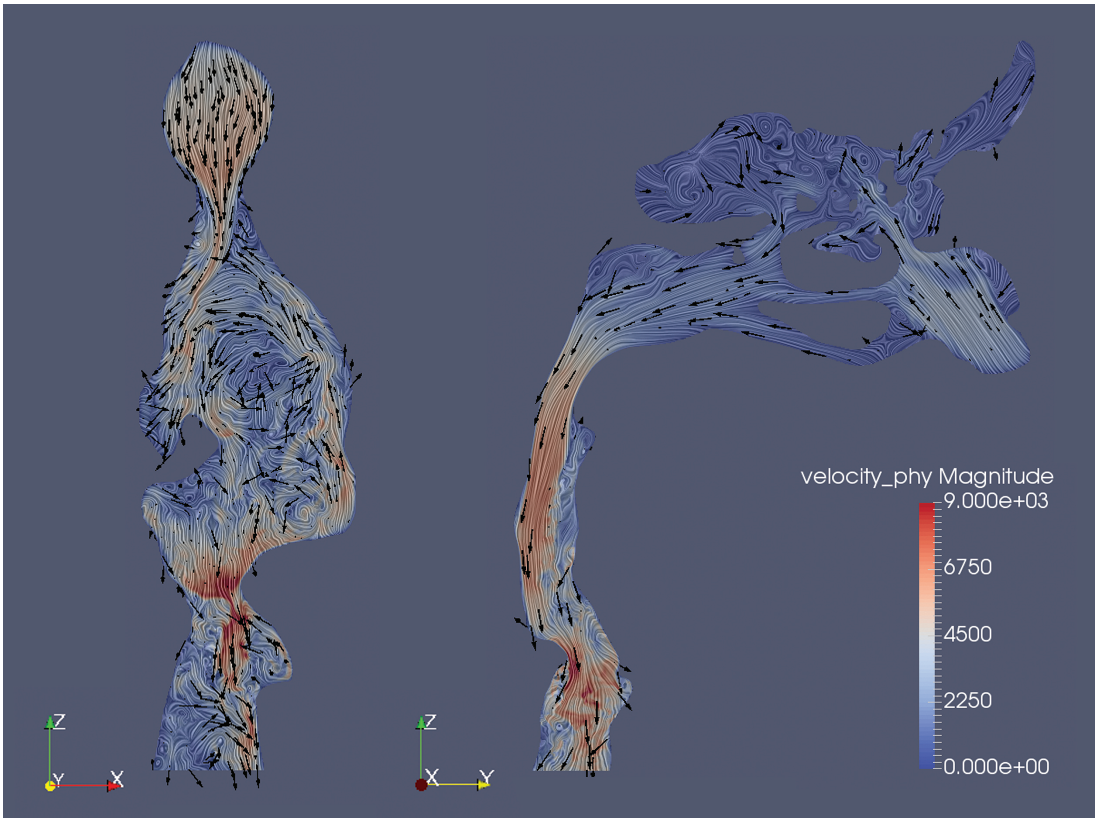

Figure 6.4: Line Integral Convolution (LIC) plot of the velocity vector field $(\mathrm{mm/s})$ in cross section V11 as defined in 5.1 and in 3R as defined in 5.7 at peak inspiration.

The pressure difference in the nostrils over time is evaluated. With the flow ratio as described in section 5.4, the maximum pressure difference between the left and right nostril is determined to be 5.26 %, the mean pressure difference 1.6 %. The pressure in both nostrils over time can be seen in figure 6.5. Pressure over time in the trachea for both experimental and numerical results during inhalation can be seen in figure 6.6. Since the numerical data only simulated one period, the same result was copied and pasted for comparison reasons at each period of the experimental results. The raw measurement data from the experiments was prone to noise and oscillations and therefore filtered with a Low-pass filter with a cut-off at 2.5 Hz. Numerical data was processed using a similar filter.
The pressure results at the other pressure points can be found in table 6.4. The experimental mean pressure was calculated from the filtered data of all inhalation periods. The minimum (peak) pressure, or maximum pressure drop, was calculated by taken the average of the minimum values obtained at each period. A contour of the numerical pressure drop can be seen in figure 6.7. A normalized pressure contour plot over slice 3R can be found in the appendix, figure D.8. More images of inhalation during unassisted breathing can also be found in appendix D, such as the progression of the flow over time in the 3R and V11 plane and vorticity over time in the V11 plane.

Table 6.4: Numerical and experimental results of the maximum and mean pressures during inhalation at pressure tab points.

	Mean pressure drop (Pa)		Maximum pressure drop (Pa)	
Point	Numerical	Experimental	Numerical	Experimental
1R	-1.17	-2.95	-3.35	-7.17
1L	-0.63	-2.52	-2.35	-6.08
2R	-3.77	-2.81	-7.60	-6.87
2L	-3.60	-2.57	-8.40	-6.04
3R	-3.72	-3.82	-7.80	-9.89
3L	-3.24	-3.52	-6.80	-8.51
4R	-4.05	-4.02	-8.50	-10.73
4L	-3.98	-3.99	-8.30	-10.65
5R	-4.39	-4.19	-9.40	-10.92
5L	-4.61	-3.98	-9.70	-10.40
6R	-4.96	-4.24	-10.80	-11.01
6L	-5.03	-4.70	-10.90	-11.84
7	-4.90	-4.68	-10.60	-11.42
8	-6.41	-5.81	-13.70	-13.82
9	-13.06	-11.45	-25.80	-23.90
10	-19.21	-17.37	-37.90	-33.94
11	-18.98	-20.39	-37.10	-39.94
12	-21.77	-18.45	-43.30	-38.22
13	-22.25	-20.52	-47.30	-40.32
14	-21.41	-16.38	-43.05	-32.39
15	-31.34	-31.59	-63.15	-58.37
16	-32.76	-28.93	-74.35	-52.64
17	-30.81	-27.88	-58.55	-52.94

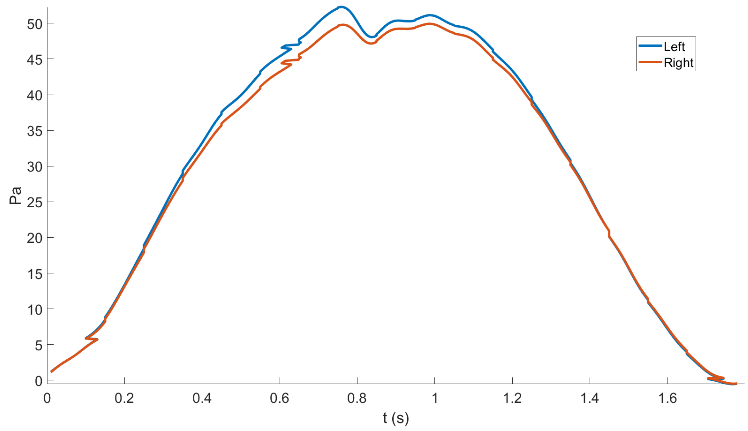

Figure 6.5: Plot of the nostril pressure with a Low-pass filter at 2.5 Hz) over time during inhalation

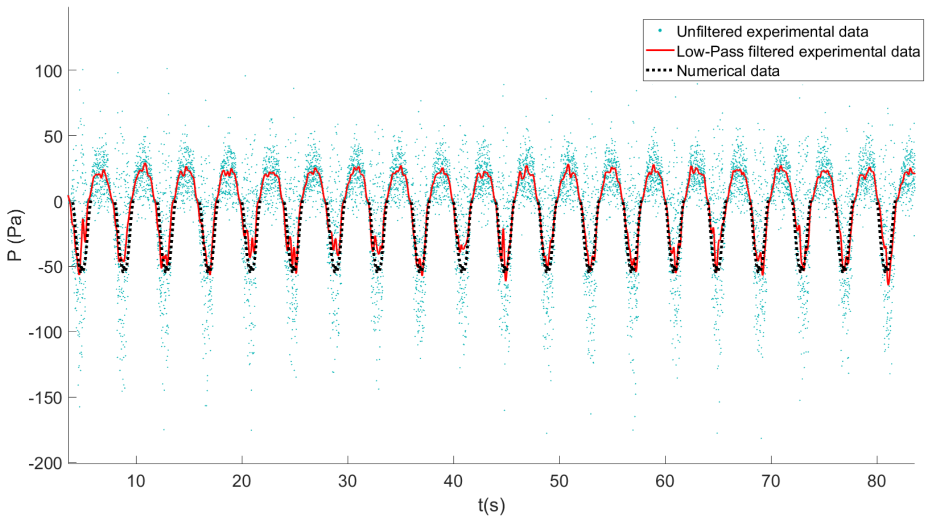

Figure 6.6: Plot of the experimental data (both unfiltered and with a Low-pass filter at 2.5 Hz) and the numerical data of inhalation repeated for the same amount of periods at the trachea (point 17).

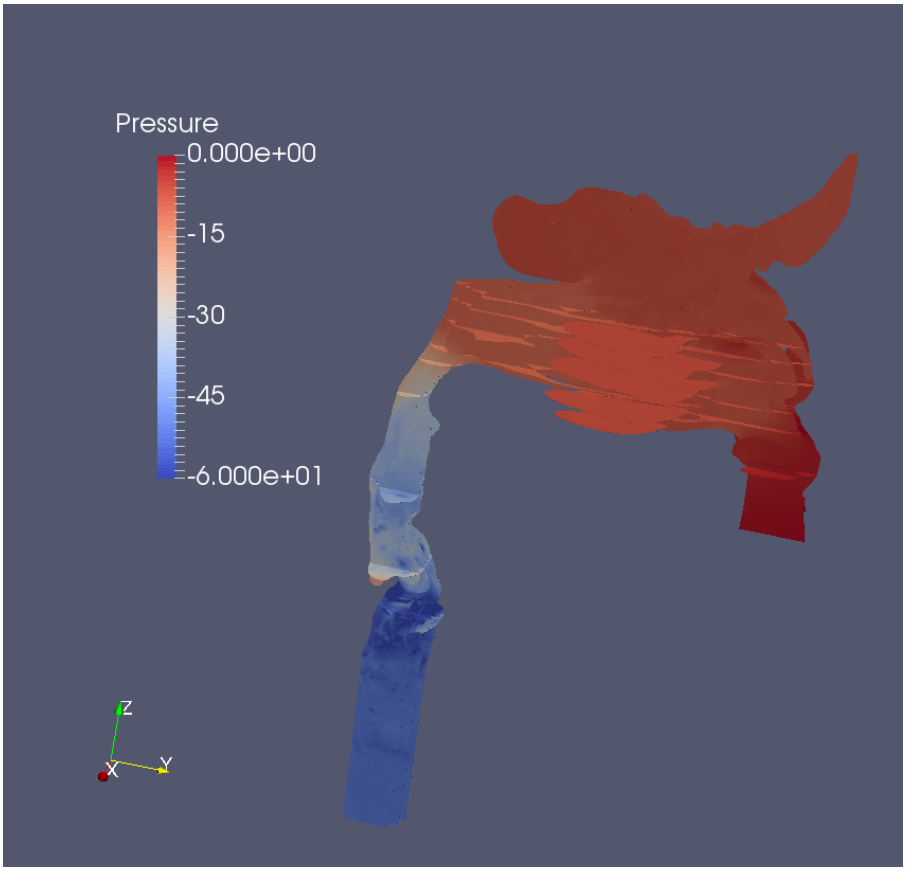

Figure 6.7: Pressure contour (Pa) of the pressure relative to the nostril pressure during peak inspiration.

6.2 Exhalation

Exhalation takes 2.216 seconds in the breathing profile that is used. Its peak flow is at 1.168 s in the exhalation part of the breathing cycle, having a volume flow rate of 16 $\mathrm{L/min}$ which corresponds with a maximum inlet velocity of 2955 $\mathrm{mm/s}$ at the trachea. The velocity magnitude at several vertical planes close to peak exhalation ($t = 1.15$ s) can be seen in figure 6.8. The maximum velocity in the nasal cavity planes as seen in figure 6.8 are listed in table 6.5. Reynolds numbers at peak expiration is 1398 at the trachea and 2242 at pharynx in the plane described in figure 5.5. Reynolds number at the left nostril is estimated to be 999, while Reynolds number at the right nostril is estimated to be 628. Flow is fully developed at the inlet boundary of the trachea, where it starts out laminar. Due to the converging geometry of the larynx, the flow is accelerated. At the smallest cross section in the larynx, the area is 78 mm^2, more than two times smaller than the cross sectional area of trachea. The velocity accelerates accordingly, creating a jet flow at the larynx. As the flow progresses through the larynx into the oropharynx, the geometry diverges before converging again in the nasopharynx, creating a second jet there that points to the top. Both jets can best be seen in the 3R plane and the vertical V11 plane, as depicted in figure 6.9 and 6.10. These jets are also present at low flow rates, though the core of the jet flow is longer for higher flow rates. This can also be seen in the snapshots of the velocity magnitude in the 3R plane over time which can be found in appendix D, figure D.14. High vorticity is observed at the walls near the jet flow due to boundary layer separation and at the shear layers of the jets due to shear flow. Recirculating flow is observed near the pharyngeal jet at the anterior site and near the laryngeal jet at posterior site due to flow separation. This is indicated by a negative amplitude of the z-velocity component and can be seen in figure D.3. The pharyngeal jet mostly points upwards, causing the flow to enter the nasal cavities most dominant near the superior nasal concha. As flow progresses towards the nostrils, the stream distributes more evenly over the cross section (see also figure 6.8). The ratio between flow rates of the right and left nostril is 0.479 : 0.521 at peak expiration when leaving the nostrils. The airflow velocity magnitude at the nostril boundaries can be seen in figure D.5. The shape of the outflow does not change much over time, in contrast to the amplitude.

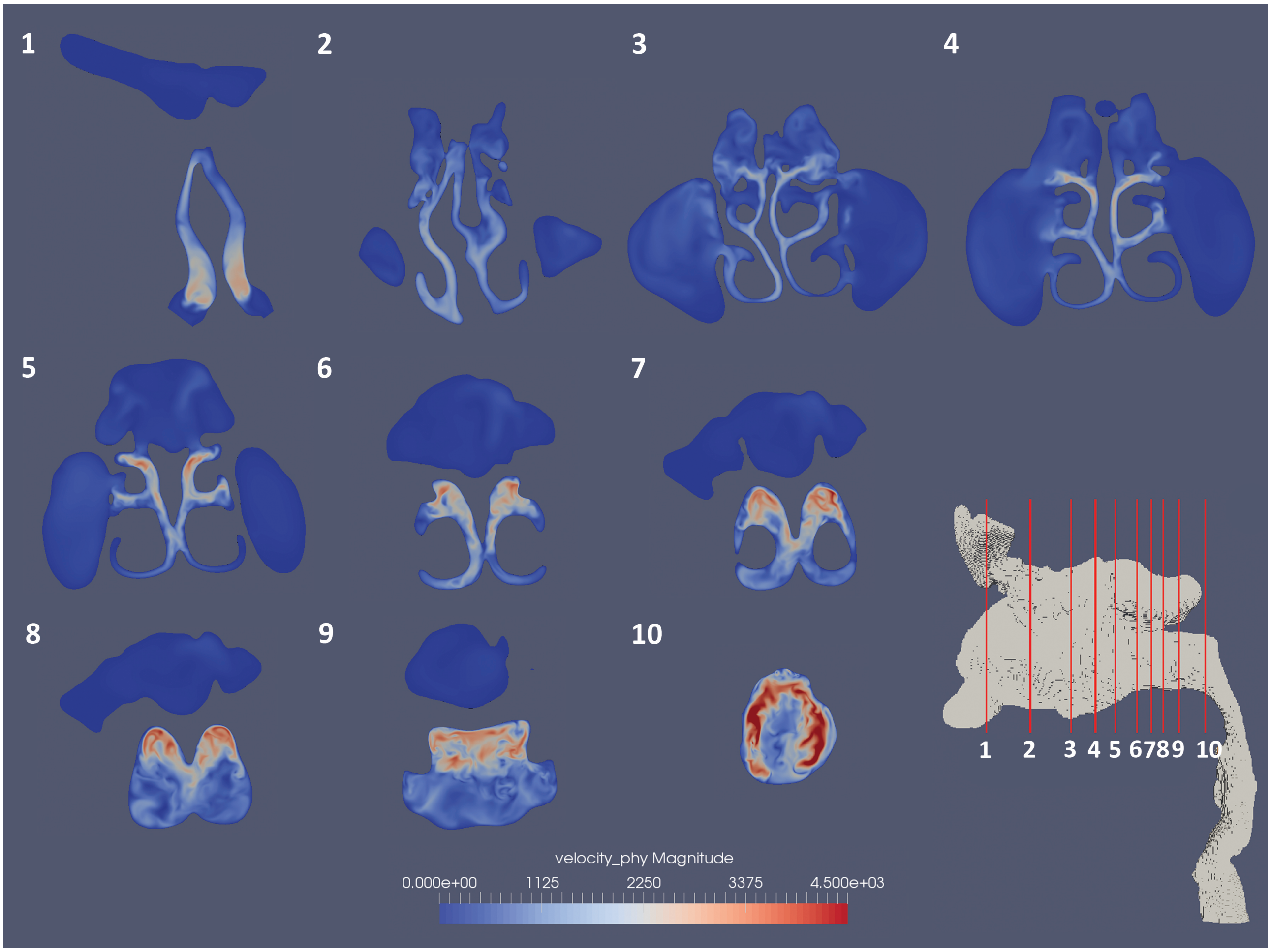

Figure 6.8: Velocity magnitude ($\mathrm{mm/s}$) at several planes during peak exhalation (16 $\mathrm{L/min}$).

Table 6.5: Maximum velocity magnitude during peak expiration on different intersection planes as described in 5.1.

Plane	V1	V2	V3	V4	V5	V6	V7	V8	V9	V10
Maximum velocity magnitude ($\mathrm{m/s}$)	2.82	2.15	2.77	2.11	3.76	3.73	4.44	4.23	3.91	5.85

Table 6.6: Numerical results of the maximum, mean and 99th and 95th percentile of the velocity magnitudes in the 3R, 3L and V11 plane during exhalation

		mean vel mag ($\mathrm{mm/s}$)			max vel mag ($\mathrm{mm/s}$)			99th percentile ($\mathrm{mm/s}$)			95 percentile ($\mathrm{mm/s}$)		
t(s)	L/min	3R	3L	V11	3R	3L	V11	3R	3L	V11	3R	3L	V11
0.15	6.42	338	282	749	2099	1888	2355	1833	1755	2055	1499	1344	1811
0.30	11.32	643	500	1300	3833	4044	4077	3255	2955	3644	2666	2388	3233
0.45	13.78	771	650	1677	5055	5088	4855	4077	3755	4444	3122	2955	3922
0.60	14.36	820	675	1788	5633	4866	5122	4199	4011	4688	3355	3055	4177
0.75	14.40	811	652	1800	5066	4544	5155	4244	3888	4644	3344	3088	4100
0.90	14.91	877	694	1833	5322	6100	5255	4377	4122	4800	3655	3255	4222
1.00	15.48	863	704	1888	5877	4855	5677	4411	4166	4700	3566	3311	4211
1.15	15.98	912	754	1877	5900	5914	5544	4777	4299	4944	3755	3255	4400
1.25	15.82	891	747	1922	6455	5288	6111	4766	4300	5411	3788	3477	4655
1.40	15.02	876	703	1822	5455	5311	5488	4488	4055	4966	3622	3122	4411
1.55	14.15	817	642	1711	5244	4733	5011	4155	3966	4733	3244	2833	4099
1.70	13.64	775	643	1711	5200	4822	4933	4099	3722	4322	3166	2955	3844
1.85	12.50	737	598	1599	4444	4400	4488	3755	3455	3977	3055	2688	3588
2.00	9.05	540	436	1200	3488	3155	3433	2833	2622	3100	2244	1900	2755

The maximum velocity at peak expiration is 6287 $\mathrm{mm/s}$, which is observed in the nasopharynx, as can be seen in figure 6.9. However, the highest velocity observed is not at peak expiration but at $1.25s$ where the velocity reaches 7257 $\mathrm{m/s}$ at the pharyngeal jet. The maximum Mach number on the lattice is therefore determined to be 0.0944, which is less than the desired upper limit of 0.1, ensuring that compressibility errors are not dominant. The mean, maximum and 99th and 95th percentile of the velocity magnitudes are listed for the 3R, the 3L and the V11 plane in table 6.6. Maximum and mean velocity magnitude are also monitored over the 23 pressure tab locations. Its results can be seen in table 6.7. The velocity over some points in time can also be seen in figure D.1 in the appendix.

A contour of the normalized pressure drop can be seen in figure 6.12 and a normalized pressure plot of slice 3R can be found in the appendix, figure D.7.More images of exhalation during unassisted breathing can be found in appendix D.

Table 6.7: Numerical results of the maximum and mean velocities during exhalation at pressure tab points

Point	velocity magnitude ($\mathrm{m/s}$)	
	Maximum	Mean
1R	0.24	0.10
1L	2.53	1.93
2R	1.31	1.01
2L	1.85	1.40
3R	0.35	0.27
3L	0.97	0.66
4R	0.35	0.22
4L	0.93	0.64
5R	0.49	0.29
5L	0.72	0.45
6R	1.00	0.67
6L	1.04	0.70

Point	velocity magnitude ($\mathrm{m/s}$)	
	Maximum	Mean
7	1.27	0.77
8	1.00	0.71
9	4.70	3.63
10	4.77	3.51
11	4.66	3.47
12	2.58	1.62
13	3.86	2.55
14	1.99	1.23
15	4.11	3.14
16	3.16	2.41
17	2.96	2.25

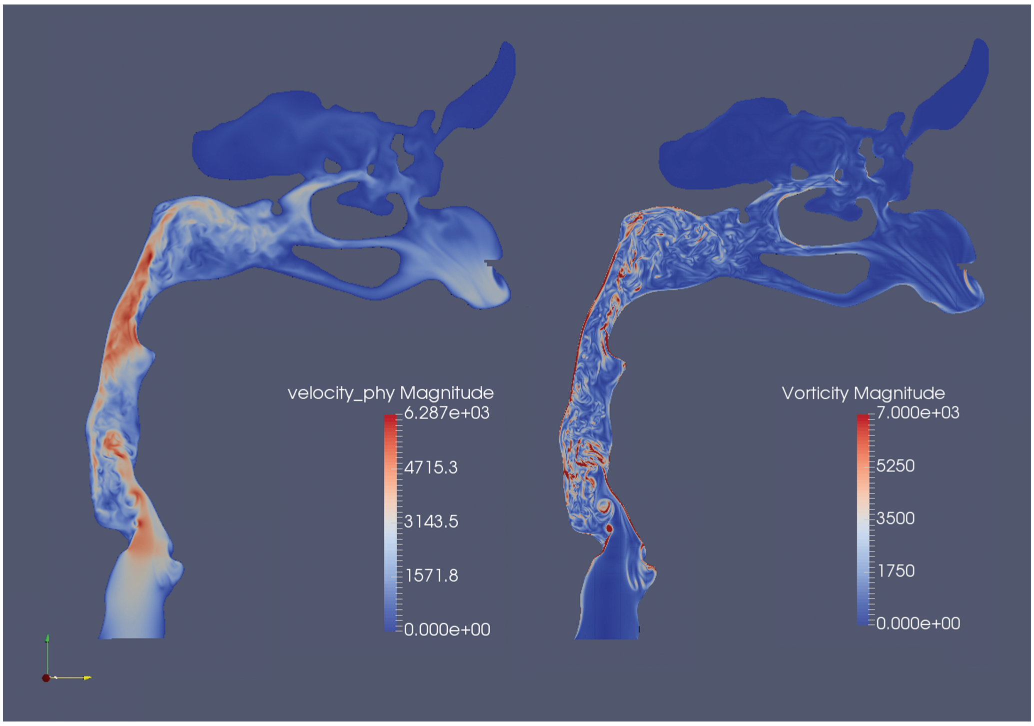

Figure 6.9: Velocity magnitude $(\mathrm{mm/s})$ and vorticity magnitude $(1/\mathrm{s})$ in cross section 3R as defined in 5.7 at peak expiration.

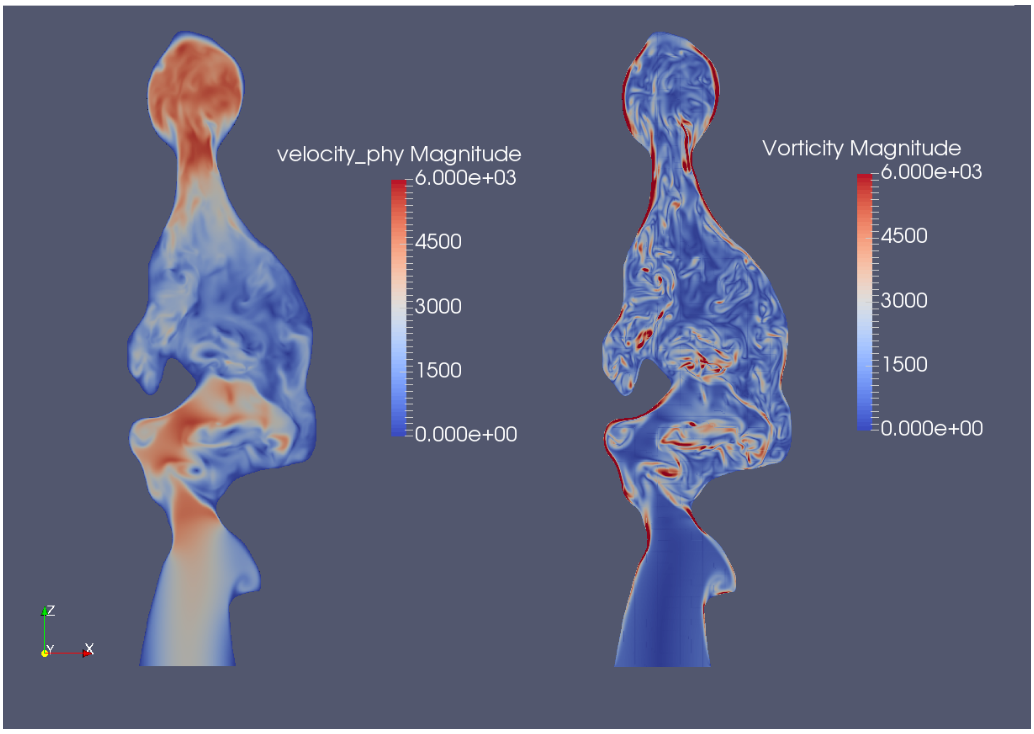

Figure 6.10: Velocity magnitude $(\mathrm{mm/s})$ and vorticity magnitude $(1/\mathrm{s})$ in cross section V11 as defined in 5.1 at peak expiration.

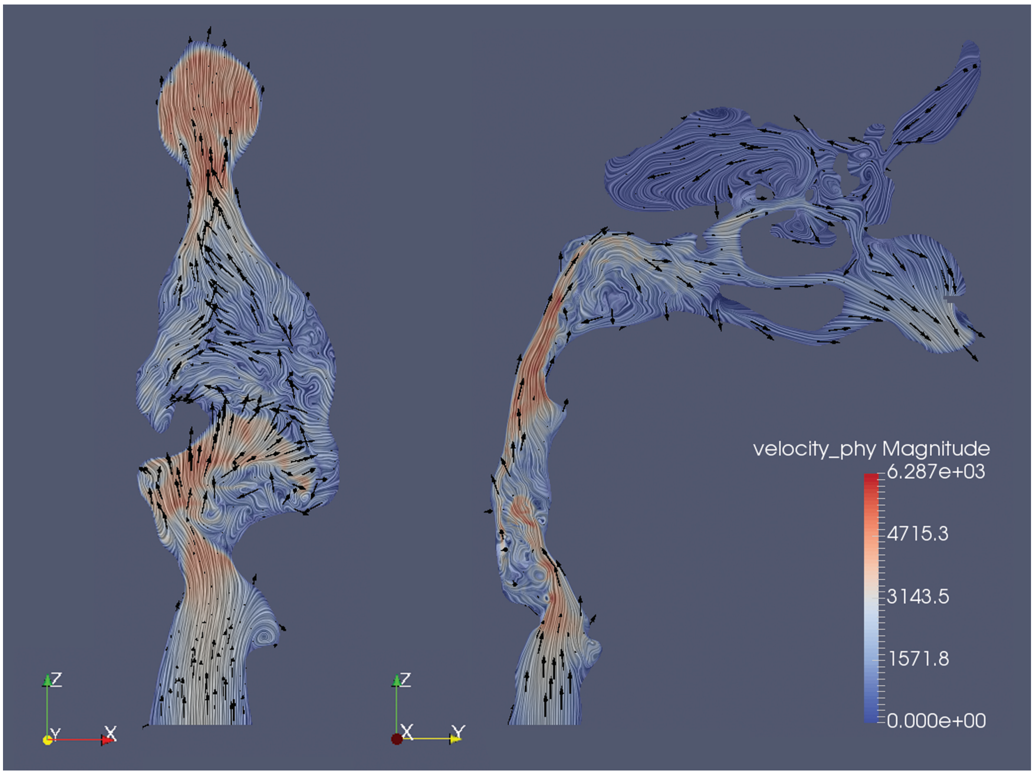

Figure 6.11: Line Integral Convolution (LIC) plot of the velocity vector field $(\mathrm{mm/s})$ in cross section V11 as defined in 5.1 and 3R as defined in 5.7 at peak expiration.

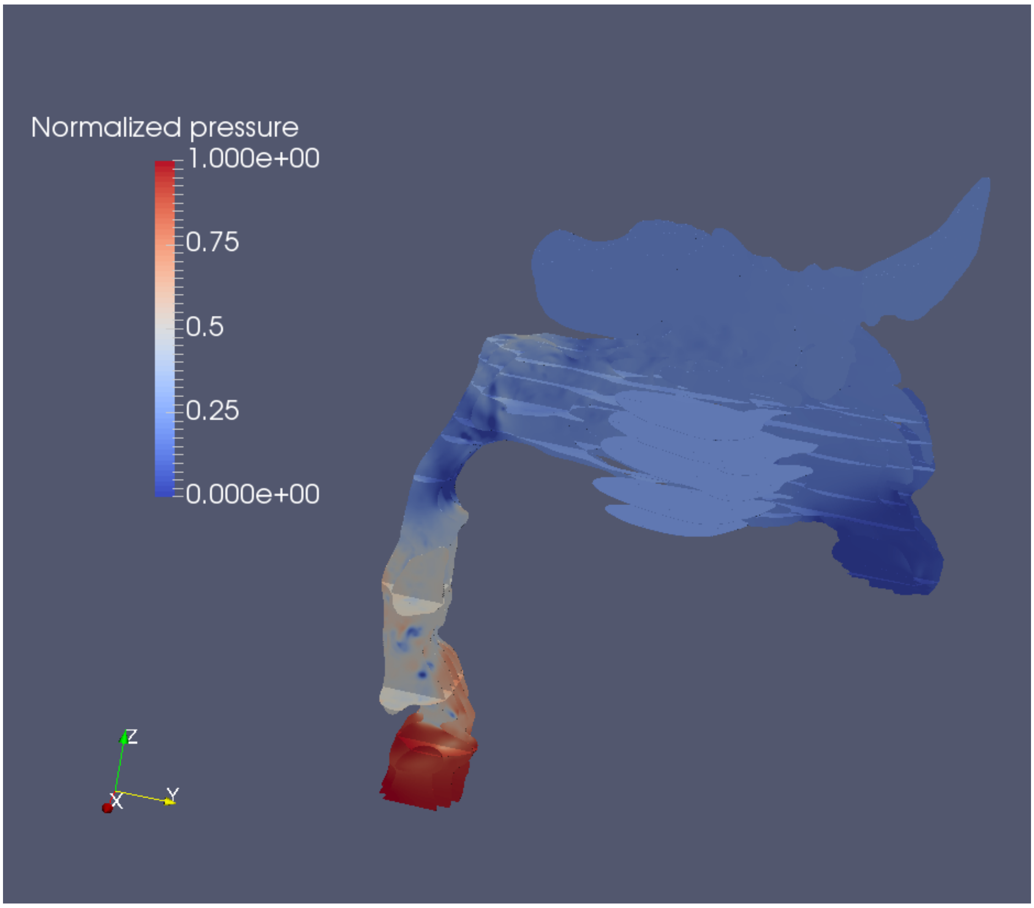

Figure 6.12: Contour of the normalized pressure $\frac{P_i - P_{nostril}}{P_{trachea} - P_{nostril}}$ at peak expiration.

6.3 Discussion

The results that are obtained with the LBM in the past two section are discussed in this section. To the results from the current work (LBM simulations) is sometimes referred to as the iterative *this work*, to show clear distinction.

Xiong et al. [104] studied laminar airflow in the paranasal sinuses and the nasal cavity and observed extremely little flow exchange between the cavities and the paranasal sinuses. *This work* shows slightly more flow in the sinuses during inhalation, but shows also almost no flow in the sinuses during exhalation. The flow in the sinuses is however not quantified.

A LES turbulence model was used to model the whole cycle in both inspiration and expiration. By implementing this model, a positive non-zero turbulent viscosity term is added. Doorly et al. [14] stated, following from an experimental research, that the airflow in the nasal cavities is mostly laminar for flow rates under 12 $\mathrm{L/min}$. Inthavong et al. [35] and Zuber et al. [112] simulated airflow less than 15 $\mathrm{L/min}$ as laminar and above as turbulent. It should be noted that the geometries used do not surpass the nasopharynx. When the rest of the inspiratory tract is regarded, the flow regimes change from laminar to transitional and end in a fully turbulent regime in the trachea [91]. The transition from laminar flow to transitional and turbulent flow makes the choice of a suitable turbulence model problematic. LES is however a good option, as studies show that it is able to accurately describe challenging transitional flows [2, 51, 55]. However, disturbances introduced artificially in the laminar region may be propagated or amplified for some geometries. Mihaescu et al. [55] compared RANS models with a LES model in a simplified pharyngeal geometry and concluded that LES models are more suitable for modelling in the pharyngeal airways than RANS models.

The next paragraphs will sometimes compare the transient obtained results with results of steady simulations in literature. Hörschler et al. [33] studied the validity of the assumption of steady flow in the nasal cavities and stated that especially at lower flow rates and increasing max flux major differences are seen.

6.3.1 Inhalation

An estimation for the division of the flow rate over both nostrils was made in section 5.4. This is to ensure that both nostrils have the same pressure condition during inhalation. Results in figure 6.5 show a difference in nostril pressure, indicating an error in the estimated flow rate ratio. The use of different flow rates in each nostril is not found in any other study. Many studies use one inlet for both nostrils by combining them or by simulating only one half of the geometry [32, 43, 104, 112]. Alternatives used were inlet conditions based on the Saint-Venant - Wantzel formula for outflow gas [47], a pressure inlet [108] or simply prescribing the same inlet in both nostrils [48]. The occurrence of an unequal flow rate between the left and right cavity is not uncommon. Lintermann et al. [47] noticed a ratio of 60.78 : 39.22 between the left and right cavity, though this was in a patient with extreme septum deviation and a swollen lower concha in the right nasal cavity. In *this work*, at peak inspiration, the balance between the volume flow during inspiration is 62:38. Bates et al. [4] included a hemisphere around the nostrils in the geometry and prescribed a velocity boundary condition at this hemisphere which caused a unequal flow rate between the left and right cavity of approximately 56:44. Zhao et al. [109] noticed an unequal flow rate of 42:58 in left and right cavities.

The difference in the geometry used in *this work* causes higher mean and maximum velocities in the left nasal cavity, as can be observed from table 6.3. Overall, the velocity maxima in the right cavity are significantly lower. This is mainly due to the geometry not being symmetrical rather than the difference in flow rate. The monitoring points are located on the same height (z-axis). The main airflow in the left cavity is geometrically lower orientated than in the right cavity, which can also be seen in figure 6.1

Table 6.2 shows not only the maximum and mean velocity magnitude but also the 99th percentile and 95th percentile of the velocity magnitudes. The main reason is that the observed maximum velocity magnitude might be higher in LES simulations than RANS simulations, as there is a chance that the local maximum velocities will be damped due to the time averaging of the RANS model. Mihaescu et al. [55] compared RANS models with a LES model in a simplified pharyngeal geometry and showed that velocities at some points can differ 30%. It was shown that the jet flow in RANS models damp out much faster.
Table 6.2 shows higher velocity magnitudes than most other numerical studies in the nasal cavities. This is mostly due to the fact that the geometry used includes the complete pharynx and larynx up until the trachea. These are regions where higher velocities are observed due to the jet flows. Figure 6.1 and table 6.4 show that the velocity magnitudes in the cavities and sinuses are lower. The maximum velocity magnitudes of the planes 1 t/m 10 are listed in table 6.1. Relatively high velocities are observed in V1, as the flow enters the nasal valve and the geometry narrows. The maximum velocity obtained in this plane during peak inspiration is 3.6 $\mathrm{m/s}$. Maximum velocity in the nasal cavities was observed in the V2

and V3 plane, with a magnitude of 3.7 $\mathrm{m/s}$ in the left cavity. In the planes, velocity peaks are observed near the middle and lower conchae.
Zhao and Jiang [108] performed a computational study of 22 adult geometries to describe normal airflow. It was stated that the location of the velocity peaks in the nasal cavities differs per individual, though it is not likely for the location to be in the superior meatus or at the olfactory cleft [108].
Inthavong et al. [35] studied flow characteristics in 6 different geometries at an inhalation flow rate of 15 $\mathrm{L/min}$. It was stated that all six geometries showed high velocities, mostly in the inferior half of a plane similar to V1 with maximum velocities ranging from 5.6 $\mathrm{m/s}$ to 2.2 $\mathrm{m/s}$. One geometry in particular shows many similarities in behaviour, which is a geometry where one nostril area is significantly bigger than the other. That case also shows more flow in the upper half of the V1 plane for the nostril with a bigger nostril area.

Brüning et al. [11] obtained an average maximum and an average mean velocity of 25 geometries over the nasal cavity during inhalation and exhalation. The averaged maximum velocity during inhalation was determined to be 2.77 $\mathrm{m/s}$ at a flow rate of 12 $\mathrm{L/min}$ with a standard deviation of 0.59 $\mathrm{m/s}$ in the nasal valve. In this work, the flow rate of 12 $\mathrm{L/min}$ occurs approximately at t=0.25 s and at t=1.50 s in the inspiration profile. Accurate comparison with *this work* is difficult, as the location of the maximum velocity is not depicted in the study by Brüning et al. [11] and the maximum velocity in the current study can not be analyzed over all cells or a specific region of cells due to the size of the mesh. Analyses of the available slices show maximum values of 2.2 $\mathrm{m/s}$ during inhalation. This value is within the standard deviation of the described averaged maximum velocity by Brüning et al. [11]. It is expected however that the actual maximum in *this work* might be (slightly) higher but not visable on the planes available.

Hörschler et al. [32] conducted a numerical study of the flow field in a simplified model of the nasal cavity. Inspiration volume flow of 16.8 $\mathrm{L/min}$ resulted in a Reynolds number of 1560 in the (single) nostril, expiration with a volume flow of 13.2 $\mathrm{L/min}$ resulted in a Reynolds number of 1230 in the nostril. Riazuddin et al. [80] studied inspiration and expiration in the nasal cavities for multiple flow rates. At an inspiratory flow rate of 15 $\mathrm{L/min}$, the nostril inlet Reynolds number was determined to be around 1600.
Lintermann et al. [47] performed Lattice Boltzmann simulations in 3 different geometries ranging from the nostrils to the pharynx. The Reynolds number of the pharynx with a hydraulic diameter of 10.49 mm was determined to be 1597 at a inspiratory flow rate of 15 $\mathrm{L/min}$. The maximum velocity of the three geometries was determined to be 6.5 $\mathrm{m/s}$, which was at the pharynx. In *this work*, the Reynolds number of the pharynx with a hydraulic diameter of 12.5 mm at t=0.35 s is estimated to be 2373, the Reynolds number at t=1.45 s is estimated to be 2037. These points in time correspond with a flow rate of $15.6\ \mathrm{L/min}$ and $13.5\ \mathrm{L/min}$. Table 6.2 shows that the maximum velocity obtained at t=0.35 s is 7.7 $\mathrm{m/s}$ and at t=1.45 s is 6.5 $\mathrm{m/s}$. If only the values are taken in the same range from the pharynx to the nostril, the maximum velocities, obtained by optical estimation, at t=0.35 s and t=1.45 s are 5.2 $\mathrm{m/s}$ and 4.5 $\mathrm{m/s}$ respectively. Xiong et al. [104] studied inspiration with a steady flow rate of 21.1 $\mathrm{L/min}$ in a CT-scan geometry that also includes the paranasal sinuses. Maximum velocity was observed to be 4.82 $\mathrm{m/s}$ in the transition zone from the nasal valve to the nasal cavities.

Figure 6.4 and D.4 show recirculation in the olfactory area as well as in the ethmoid sinuses and the upper region near the nasopharyngeal wall. Recirculation in the olfactory region is a common airflow characteristic. The study of Inthavong et al. [35] showed recirculation in the olfactory region for geometries with a bi-lateral and uni-lateral notch in the nasal vestibule, as well as in one of the not-notched geometries. Riazuddin et al. [80] observed the same recirculation at the olfactory region with recirculating flow with low velocity magnitudes. Recirculation was also observed by other studies [65, 100, 112]. Zhao and Jiang [108] stated that the forming of the vortex is mostly dependent of the angle of the nostrils and the volume change between the nasal valve and the cavities. Taylor et al. [92] stated that the region of the olfactory cleft is most prone to the type of inlet boundary condition prescribed. For the purpose of *this work*, the influence of the boundary condition is relatively low, as the precise characteristics of the flow in the olfactory cleft such as wall-shear stress or odorant transport are not of interest.
Highest vorticity magnitudes are observed at the core and the shear layers of the pharyngeal and laryngeal jet, as can be seen in figure 6.2 and 6.3. Some flow detachment in the jet in the pharynx leaves under a slight angle, as can be seen in figure 6.2. A possible reason for this behaviour is the difference in the nasal cavities. The angle of the jet is not a direct result of the flow rate error, as its behaviour is also observed at time steps in the inhalation cycle where lower flow rates occur and the error between the nostril pressures low is.
The laryngeal jet is the place in the geometry with the highest velocity magnitude. Near peak inspiration, velocities with a magnitude of 11.2 $\mathrm{m/s}$ are observed. Tabe et al. [91] studied the airflow in a realistic model from the oral cavities to the trachea for flow rates spanning from 30 $\mathrm{L/min}$ to 60 $\mathrm{L/min}$. Laryngeal jet flow was observed with a velocity magnitude of 22 $\mathrm{m/s}$ at a flow rate of 30 $\mathrm{L/min}$. A main flow recirculation zone was observed near the trachea inlet plane. similar recirculation was also observed in *this work*. Wang et al. [99] studied tidal breathing with a sinusoidal function with a peak of 36 $\mathrm{L/min}$. The geometry consisted of a CT-scan from the nasal cavities up until the trachea and was extended

to the lungs. A k - ϵ turbulence model was used. Maximum velocity during inspiration was 6.5 $\mathrm{m/s}$, which was near the nostrils. It is stated that the velocity magnitudes decrease going to the nasopharynx. A pharyngeal jet was observed, but with a significantly lower velocity magnitude as observed in *this work* and the study of Tabe et al. [91].
Lin et al. [46] studied the characteristics of the turbulent laryngeal jet in a geometry that includes the mouth, oropharynx, the larynx, the trachea and the airway tree. Reynolds number in the trachea was determined to be 1700 at an inlet flow rate of 19.2 $\mathrm{L/min}$. It was observed that the maximum velocity is biased toward the posterior side of the trachea wall. High turbulent kinetic energy was observed in the trachea jet and core of in narrow zones near the trachea walls. Martonen et al. [52] studied the airflow in a simplified model of the larynx and the upper tracheobronchial airways. Despite the use of a simplified model, a pharyngeal jet with recirculating flow near the trachea and pharynx were localized. Velocities with a magnitude of 11.1 $\mathrm{m/s}$ were observed during 15 $\mathrm{L/min}$ inspiration. Trachea Reynolds number was determined to be 1160. The LES simulations performed by Mihaescu et al. [55] show velocity speed in z-direction in the pharynx of 5.1 $\mathrm{m/s}$ at a flow rate of 10 $\mathrm{L/min}$. Reynolds numbers were calculated to vary between 1000 and 2700. Table 6.2 shows the maximum velocity in the 3R, 3L and V11 planes at 12.4 $\mathrm{L/min}$ to be 5.3 $\mathrm{m/s}$, and at 15.6 $\mathrm{L/min}$ to be 7.7 $\mathrm{m/s}$.
Liu et al. [48] studied flow in a obstructed airway, where the pharyngeal diameter is smaller, and also observed pharyngeal jet flow in both expiration and inspiration using a LES model. A velocity magnitude of 6.2 $\mathrm{m/s}$ was found at 16.8 $\mathrm{L/min}$ inspiration. *This work* shows similar velocity magnitudes, jet flow and recirculation zones in both expiration and inspiration. Differences are found near the larynx, where the flow in *this work* reaches even higher velocities and the velocity magnitudes in the study of Liu et al. [48] decrease near the larynx to approximately 4 $\mathrm{m/s}$. Bates et al. [4] studied a transient sniffing profile with peak flow of 60L/min in a realistic geometry from the hemisphere around the nostrils to the bronchial tree. Pharyngeal and laryngeal jets are observed with Vorticity behaviour very similar to this work. Velocity magnitudes observed during peak sniffing in the larynx and pharynx were found to be 10.8 and 17.7 $\mathrm{m/s}$ respectively.
[105] studied the inhalation in three different geometries from the nostrils till the trachea. Big differences in velocity magnitudes at the larynx were observed for the three different CT-scan based models due to the shape of the larynx. One model showed higher velocities in the pharyngeal jet than the laryngeal jet, while the other two showed higher velocity magnitudes in the laryngeal jet. All three models showed a shift in high velocity zone from the anterior wall in the pharynx to the posterior wall in the larynx, something which can also be observed in *this work* (figure 6.2). The geometry of the pharynx and larynx has a big influence of the jet flow behaviour, where especially the angle between the trachea and the larynx is of importance. It is believed that this is the reason for the high velocities observed in this region in the current study, though more research is required to support this statement.

Pressure drop

A direct comparison of the pressure results with the experiments from the same geometry can be made. In general, the numerical pressure results show good agreement with the experiments, as can also be seen in figure 6.6 and in table 6.4. The mean absolute difference in pressure drop between the experimental and numerical means and maxima is 1.33 Pa and 3.78 Pa. The mean and maximum pressure results from table 6.4 are normalized by dividing the mean/maximum pressure of a pressure tab point by the mean/maximum pressure at point 17 (the trachea), as described in equation 6.2.The normalized mean and normalized maximum pressure can be seen in figure 6.13 and 6.14 respectively. The points that shows the biggest deviation in normalized pressure drop behaviour between the numerical and experimental results are 11, 14 and 16 and the maximum value at 15. The difference in point 11 is expected, due to the mistake in monitoring location as explained in section 5.8. The other points will be looked into with more detail.
The numerical pressures are calculated in the middle of the geometry, while the experimental pressures are measured at the walls. At point 16, the flow is very turbulent which can cause local pressure peaks. This is a probable cause for the big difference between the measured and calculated pressure drop between point 16 and the nostril pressure. To illustrate this, the pressure difference between the mean nostril pressure and the calculated pressure at the line between the points [83.5 49 40] and [83.5 64 40] is plotted in figure D.15. This is in the same plane as the plane where point 16 [83.64 56.71 40] is in. The pressure drop value at the pressure tab point in the wall is 9% lower than the pressure value drop at point 16 in the simulations and 18% lower than the maximum pressure drop value calculated at the line. The mean pressure drop between the nostrils and the line is 58.3 Pa, which is 2.5% higher than the pressure drop measured in point 16. This behaviour was also seen at point 14. Exactly the opposite happens at point 15, where the pressure drop between point 15 and the nostrils is lower than the pressure drop measured at the experiment. A line plot can again be found in the appendix, figure D.16. The mean pressure drop over the cross sectional line is in this case 1.75 $\%$ lower than the measured pressure drop at point 15, but the measured pressure drop between the wall and the nostrils is 5.3% higher than the pressure drop calculated over point 15 and the nostrils.
The pressure over the nasal cavity up until the (naso)pharynx was also determined and compared with other studies by Riazuddin et al. [80]. The numerically calculated pressure drop for an inflow of 15 $\mathrm{L/min}$ was 22.6 Pa during inspiration. Other pressure drops from the literature at the same point mentioned in the research of Riazuddin et al. [80] are 18 Pa and 20 Pa. The pressure drop of the current study at a similar point in the geometry and at a point in time with the same volume flow rate is determined to be around 18 Pa. Taylor et al. [92] listed results for the pressure drop for different

boundary conditions over the nasal cavity for a volume flow rate of 6 $\mathrm{L/min}$. The pressure drop was determined to be between 8.7 and 9.7 Pa for a female subject and between 1.7 to 2.0 Pa for a male subject, the ranges for both subjects were dependent on the boundary condition at the inlet. The difference in pressure drop between the geometries was claimed to be a cause of different passage volumes. Nostril Reynolds number was calculated by using the area of the nasal vale times 4 divided by the perimeter of the nostril as the hydraulic diameter. At 6 $\mathrm{L/min}$ it was determined to be 900 for subject A and 675 for subject B. The pressure drops in *this work* close to 6 $\mathrm{L/min}$ was determined at t=0.112 s (6.06 $\mathrm{L/min}$) and at t=1.648 s (5.99 $\mathrm{L/min}$), which gives a pressure drop in point 9 of 3.9 Pa and 3.1 Pa respectively.

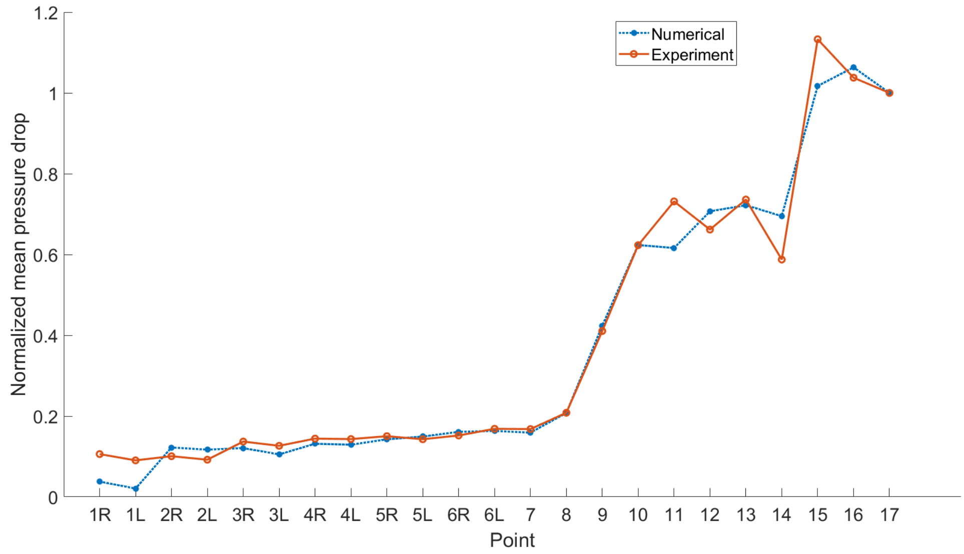

Figure 6.13: Comparison of the numerical and experimental normalized mean pressure drop at each point during inhalation

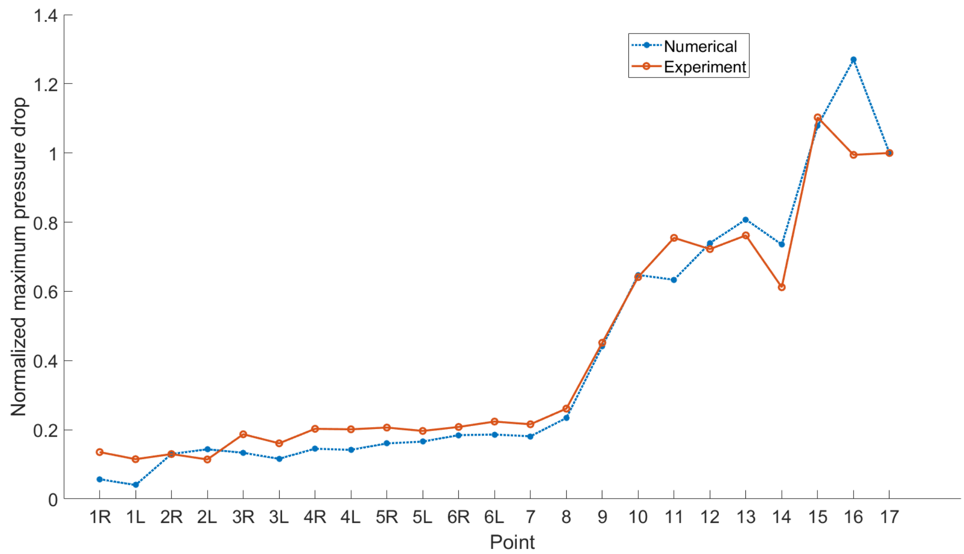

Figure 6.14: Comparison of the numerical and experimental normalized maximum pressure drop at each point during exhalation

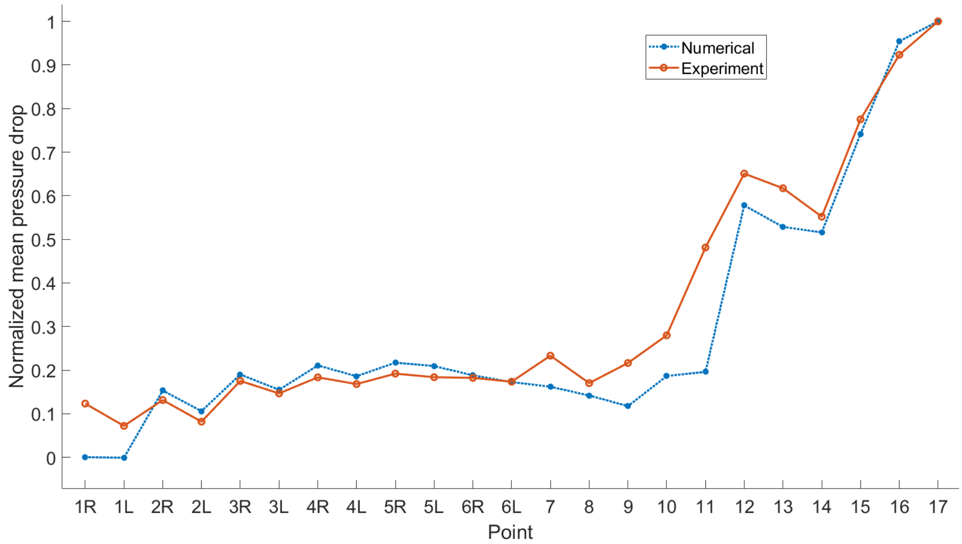

Figure 6.15: Comparison of the numerical and experimental normalized mean pressure drop at each point during exhalation

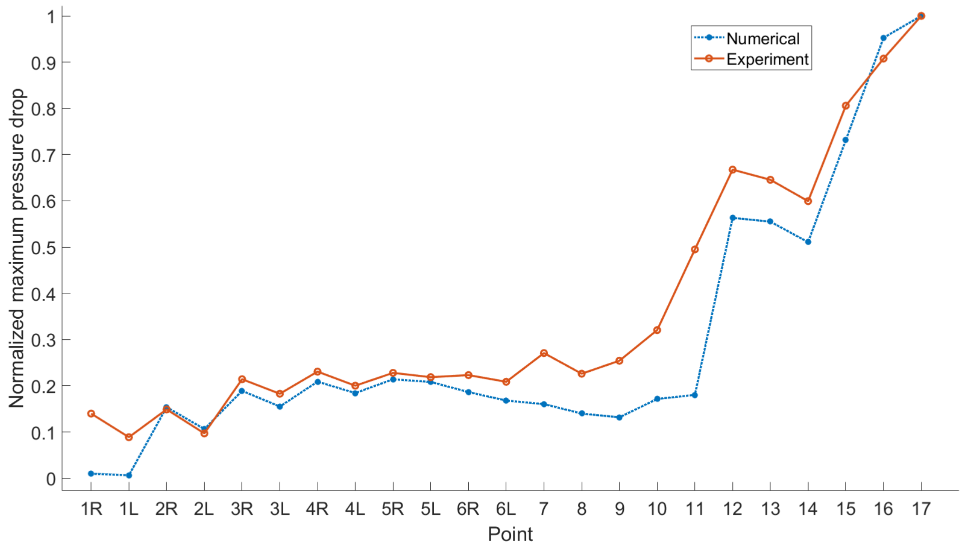

Figure 6.16: Comparison of the numerical and experimental normalized maximum pressure drop at each point during exhalation

6.3.2 Exhalation

Similar to inhalation, table 6.7 shows significant differences between the mean and maximum velocity in left and right nasal cavities at the measured points. This is a result of asymmetric geometry of the nasal cavity. The location of each left and right component of the points monitored is at equal height, in the lower region of the nasal cavity under the inferior concha. From figure D.6 in the Appendix it can be seen that the flow in the right cavity is more dominant in the upper regions of the nasal cavity while the flow in the left cavity is more equally spread over the geometry, resulting in higher flow velocities at the pressure tap points.
Table 6.6 shows the velocity magnitude characteristics over the 3R, 3L and V11 plane. It can be noted that in general the velocities during expiration are lower than velocities during inhalation. Highest velocities are seen at the laryngeal and pharyngeal jet. Velocities in the nasal cavities are lower. In the planes V1-V10 shows the V10 plane the highest velocity, due to the pharyngeal jet being still present in this plane. In the rest of the planes in the nasal cavity the velocity decelerates before accelerating just before the nostril output. Brüning et al. [11] described a velocity boundary condition at the truncated pharynx that corresponded in a 12 $\mathrm{L/min}$ flow rate. The averaged maximum flow velocity during exhalation was determined over 25 geometries to be 2.99 $\mathrm{m/s}$ with a standard deviation of 0.67 $\mathrm{m/s}$. In *this work*, highest velocities obtained at t=1.85 s (12.6 $\mathrm{L/min}$) is 4.4 $\mathrm{m/s}$ in the V8 plane. This is the end of the jet originating from the nasopharynx. Highest velocities at t=1.85 s in the V1, V2 and V3 plane are 2.4, 1.81 and 2.19 $\mathrm{m/s}$ respectively. The observed velocities in the nasal cavity by Brüning et al. [11] closer to the pharynx are smaller, but this is probably due to the fact that the study of Brüning et al. [11] does not simulate the complete pharynx and therefore does not observe the jet. Velocities observed in the planes closer to the nostrils are within the standard deviation. Na et al. [65] also studied the flow from a truncated pharynx and found the maximum velocity during expiration to be 3.28 $\mathrm{m/s}$ in the nasal valve at a steady flow rate of 15 $\mathrm{L/min}$. Normal velocities in cut planes in the nasal cavity showed significantly lower velocities neighbouring 2 $\mathrm{m/s}$. Xiong et al. [104] observed a maximum flow velocity in the nasal cavity of 3.76 $\mathrm{m/s}$ for a flow rate of 21.1 $\mathrm{L/min}$. Hörschler et al. [32] assumed a flow rate of 13.2 $\mathrm{L/min}$ during exhalation and computed the Reynolds number in the (single) nostril to be 1230. Riazuddin et al. [80] observed flow recirculation at the lower part of the posterior region of the nasal cavity in the neighbourhood of the soft palate, beneath the nasopharyngeal jet. This was also observed in *this work*, as can best be seen in figure 6.11.

Liu et al. [48] observed similar jet flow in the pharynx when performing a numerical study with LES turbulence model of the respiratory tract with an obstruction, where the pharynx causes a jet flow with a high magnitude but also a negative velocity near the anterior wall indicating reversed flow. Liu et al. [48] stated that the maximum velocity before the pharyngeal jet is approximately $5.6\ \mathrm{m/s}$ for a flow rate of $16.8\ \mathrm{L/min}$. The velocity of the pharyngeal jet at $16.0\ \mathrm{L/min}$ in *this work* is approximately 6.3 $\mathrm{m/s}$.

The pressure during exhalation could not be directly be compared with the experiments due to the scaling explained in section 5.8. Pressure was therefore only compared by the normalized pressure drop, as defined in equation 6.2.
The results can be seen in figure 6.16 and 6.15. The normalized pressure drop show reasonable to good agreement with the experiments. The normalized pressure drop in the cavities is slightly higher in the numerical simulations than in the experiments. Biggest difference is again seen in point 11, as expected due to the fault in location.

6.3.3 Concluding remarks

Nasal airflow is very dependent on individual geometries. A universal airflow is yet to be described. The pressure results obtained from the simulations show good agreement with the pressure measured from the experiments. The Lattice Boltzmann method was able to simulate the complex airflow from the nostrils to the trachea where recirculation zones and jet flow in the larynx and pharynx are observed. Vorticity and velocity plots of several section planes were created and plotted. The simulations show insight of the flow in the geometry, which will also be used for NHFT experiments.

7 | Lattice Boltzmann method in Nasal High Flow Therapy

Simulating Nasal High Flow Therapy turned too big of a challenge and it was not succeeded due to a few reasons. This chapter will be used to explain the case, the challenges and the reasons why these challenges are not (yet) tackled .

7.1 Case description

The same geometry and fluid parameters are used as during unassisted breathing. During Nasal High Flow Therapy, cannulas are inserted in the nostrils which supply humidified air. The experiments are performed with three different sizes of cannula, produced by Fisher & Paykel Healthcare. The diameters for the large, medium and small cannula are measured to be 6 mm, 4.5 mm and 3-4 mm respectively. Stereolithographic (STL) parts for the cannulas were made as cylinders with a wall thickness of 0.5 mm, which is approximately one cell. Orientation of the cannula is first determined to be normal to the xy-plane, though other orientations and angles are possible. A coarse mesh representation of the configuration can be seen in figure 7.1. Hove et al. [31] stated that an alteration of the cannula angle by 15% can change the pressure generated by 10%. The breathing profile as depicted in figure 5.3 and used in the unassisted breathing describes is assumed to be the same in NHFT.

7.2 Dimensionless numbers

Nasal High Flow Therapy uses inflow flow rates up to 60 $\mathrm{L/min}$ that insert the cannulas. Estimation of the Reynolds numbers and local Mach numbers can be made in the cannulas. It is assumed that the grid spacing and the relaxation parameter τ stay the same: $(h = 0.048)$ mm and $\tau = \frac{1}{1.95}$. The velocity magnitudes in the cannula can be calculated from the flow rates by dividing over the cannula area. It is assumed that the velocity profiles stay flat in the cannulas. Reynolds number are calculated using the inside diameters of the cannulas. Outside diameter of the smallest cannula is set to be 3.5 mm for the calculations of the dimensionless parameters. The results for the different cannula sizes and flow rates can be seen in table 7.1

Table 7.1: Calculation of the Reynolds number and Mach number based on the volume flow rate and the diameter of the cannula for different cannula sizes and therapy flow rates.

	Large Cannula (6mm)				Medium Cannula (4.5mm)				Small Cannula (3.5mm)			
Total inflow (L/min)	20	30	40	60	20	30	40	60	20	30	40	60
Reynolds number	2693	4039	5385	8078	3846	5770	7693	11539	5385	8078	10770	16155
Lattice Mach number	0.11	0.16	0.22	0.33	0.23	0.34	0.45	0.68	0.44	0.66	0.88	1.33

It can be seen that high Reynolds numbers and lattice Mach numbers are expected. In general, lattice Mach numbers bigger than 0.15 are highly unwanted and simulating with Mach numbers that exceed 0.30 is by the definition of Lattice-Boltzmann Method not physical. The lattice Mach numbers calculated in table 7.1 are only the minimum mach numbers that are seen in the cannula and not necessarily the highest Mach number that occur in the geometry, on the contrary it is expected that higher velocity magnitudes might occur in the rest in the geometry. The Reynolds numbers are not dependent on the LBM parameters, but the lattice Mach numbers are. As the relaxation parameter is almost on its lowest limit, the only possibility is to reduce the grid spacing. Mach numbers in diffusive scaling are linearly related with the grid spacing. The mesh size is related with the grid spacing to the third order, since the geometry is in 3D. This means that reducing the mach numbers to an acceptable level results in mesh sizes that are simply too big to compute. To illustrate this, the amount of cells needed per case is estimated for an upper Mach number limit of 0.15. Grid spacing is

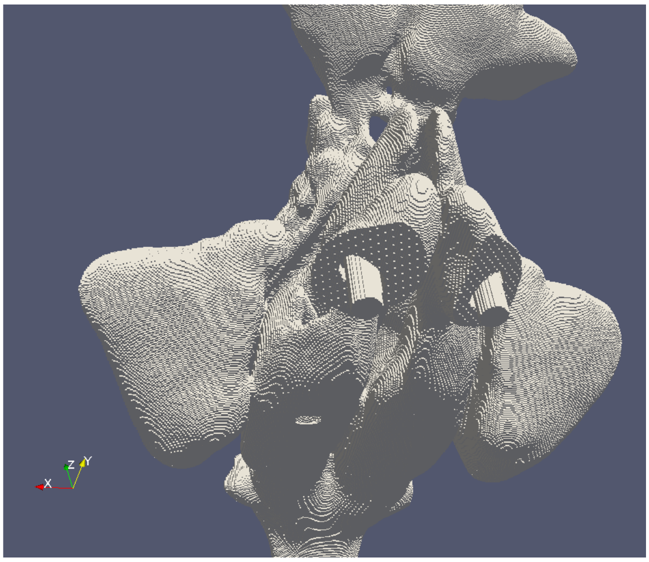

Figure 7.1: Coarse mesh representation of the configuration for NHFT simulations.

calculated using $\tau = \frac{1}{1.95}$, the desired Mach number, the total inflow and the geometrical properties of the cannula. The calculated grid spacing with the resulting estimated mesh sizes are listed in table 7.2. Simulations up till 2.9 billion cells have been performed before using the same LBM code with diffusive scaling [37]. This was however on 304K cores. The amount of cores available for this study was limited to 7.2K due to some technical difficulties at the supercomputer. It is therefore believed that with more resources some of the listed NHFT cases can be simulated without any change in the code configuration, other cases might need other methods such as local grid refinements on which will be elaborated on in chapter 8.

Table 7.2: Calculation of the maximum grid spacing that ensures a Lattice Mach number of ≤ 0.15 based on the volume flow rate and cannula sizes.

	Large Cannula (6mm)				Medium Cannula (4.5mm)				Small Cannula (3.5mm)			
Total inflow (L/min)	20	30	40	60	20	30	40	60	20	30	40	60
h (μm)	65	44	32	22	32	21	16	11	16	11	8	5
Mesh size (Billion cells)	0.44	1.48	3.51	11.86	3.73	12.60	29.87	100.81	28.12	94.89	224.92	759.11

7.3 On Boundary conditions

An important concept that contributes to the working mechanisms of nasal high flow therapy is leakage. The surplus of delivered air can escape the nasal geometry due to the leakage in the nostrils. The area of the cannula is typically twice as small as the area of he nostrils. This however changes the case to a problem with six boundary conditions. Two inflow boundary conditions are needed, one for each cannula (both in inspiration and expiration). The wall is a boundary condition, which can be set to a no-slip boundary condition. The remainder of the nostril areas represent two outlet boundary conditions, which can be set to zero pressure outlet for both inspiration and expiration. The trachea concludes the list of boundary conditions. The boundary condition in the trachea is also the one that requires most attention. This is best explained using a simple example. Consider a constant flow rate of 30 $\mathrm{L/min}$ evenly distributed over both cannulas, often described as the possible optimal flow rate for NHFT [81]. For the simplicity in this example, a constant breathing flow of 13 $\mathrm{L/min}$ is assumed in both inspiration and expiration. This means that during exhalation, flow with a flow rate of 13 $\mathrm{L/min}$ leaves the trachea. A total flow of 30 $\mathrm{L/min}$ enters the geometry from the cannulas. The flow rate that comes out of the nostrils is then 43 $\mathrm{L/min}$. The problem during exhalation can therefore fully be described by prescribing zero pressure outlets in the nostrils, a velocity profile in the cannulas and a velocity profile in the trachea. This is not the case during inspiration. The cannula flow stays 15 $\mathrm{L/min}$ per cannula. The challenge arises when prescribing a boundary condition at the trachea that ensures that the right volume flow enters the trachea. In the example case, flow enters the geometry with a rate of 30 $\mathrm{L/min}$. The inspiratory flow in the trachea should be 13 $\mathrm{L/min}$, so flow should leave the nostrils with a rate of 17 $\mathrm{L/min}$. It is therefore needed to prescribe pressure boundary conditions in the nostril outlet and at the trachea outlet in such a way that flow leaves the geometry in the desired ratio. These pressure conditions might be easy to find for steady inspiration but for transient simulations that follow the breathing profile, the pressure conditions should be time dependent. To obtain an accurate pressure relation, many iterations are needed which require many resources. This problem can possibly be tackled by assuming the problem to be quasi-steady. It is then possible to reverse the problem by prescribing some pressures, run steady simulations and investigate the flow distribution. Several simulations could be performed with different pressures until the steady solutions within the whole range of the inspiration cycle are found. Still this method requires many resources, but less than the transient method. Simulating a steady state with Lattice Boltzmann method in problems with these velocity magnitudes takes a very long time, since the geometry will stay in the order of 1000M cells. Scaling the problem is not an option. Changing settings of the simulation, such as changing the cannula size, the flow rate or the orientation requires new iterations and therefore even more time and resources.

A lack of time and resources to overcome the described problems is the reasons why simulating NHFT with Lattice Boltzmann was not succeeded in this thesis.

8 | Recommendations and limitations

Several recommendations arise from the research that is conducted. The work that is done also shows several limitations. Some of the recommendations and limitations were briefly mentioned before but will be elaborated on in this chapter.

The main purpose of this research was to study the effects of Nasal High Flow Therapy and ideally find optimal patient settings. Simulating NHFT did not succeed due to the occurrence of high local Mach numbers and Reynolds numbers, as discussed in chapter 7. The most important recommendation is therefore to use local grid refinements in the regions with high Mach numbers However, this brings new challenges in the simulations as due to the diffusive scaling, the time step on a grid that is refined to $h/2$ should become $dt/4$. Musubi, the code that is used, is able to implement local grid refinements with diffusive scaling [28]. Implementing this procedure in the NHFT simulations is worth to look into. Local refinements should probably be made in the cannula, the neighbourhood of the cannula, the smallest region of the pharynx where the jet occurs and the region where the laryngeal jet occurs.

Unassisted breathing simulations were performed, as it is wanted to compare the flow and wash-out of CO_2 rich air in the geometry. In future work, it is wanted to implement a method in the code that can track particles or CO_2 fractions. Simulations during NHFT and unassisted breathing could then be compared on the wash-out effects of CO_2 rich air, as seen in the study by Hove et al. [31].

Simulating NHFT comes with a set of unknown boundary conditions, as has been extensively explained in section 7.3. An approach has been described, which is computationally expensive. Especially by taking into account that, to find optimal therapy settings for NHFT, a wide variety of parameters should be studied such as: Different flow rates, geometries, cannula sizes, positioning of the cannulas and supplied airflow properties. Another method to more effectively tackle this problem would be to implement an pressure boundary condition that tries to target a mass flow rate. Such a method is implemented in the Finite Volume Method solver Fluent by Ansys [34]. A variation of Bernoulli's equation is used:

$$dP = \frac{\frac{1}{2}\rho_{avg}\left(\dot{m}^2 - \dot{m}_{target}^2\right)}{\rho_{avg}^2 A^2} \tag{8.1}$$

With dP the pressure change (Pa), $\dot{m}$ the mass flow rate, A the area of the boundary m^2 and ρ_{avg} the average density over the area $\mathrm{kg/m^3}$. The concept is that every iteration, the pressure changes accordingly to the mass flow rate that is achieved at the boundary to target the mass flow rate prescribed. A similar method is also implemented in Musubi, but has so far only been validated for a multi-specie flow case [113].

In the unassisted breathing study (chapter 6), only the geometry of one individual was used. The whole study adds in value when more geometries are used. The used geometry is obtained from a third party and segmentation was not performed by the author. Limitations in the geometry are therefore unknown. Despite the geometry being realistic, it is only a small part of the complete respiratory tract. Simulations that include the bronchial tree are seen in the literature, though often partially and/or simplified [46, 99]. The geometry in the current study does not include the oral cavities and assumes no airflow through the mouth. In physical situations, breathing with open mouth is not uncommon. Including the oral cavities and study the (partially) breathing from the mouth adds value to the study. Ideally, the influence of different breathing profiles should be studied. However, this is only of importance to contribute to the knowledge of tidal breathing and not necessarily for the understanding of NHFT.

There is still a lot of doubt about the influence of certain geometry characteristics and deviations. Quantifying the influence of certain geometry characteristics on the global airflow and flow during NHFT is yet to be done [15, 31]. It might be very helpful if in future researches a universal procedure in segmenting the geometry will be used. Different choices in image segmentation also leads to differences in the geometries [15]. The study of Nejati et al. [66] describes a method that can obtain geometries from a wide variety of nasal cavity shapes, including different numbers of conchae and deformations. No extensive geometry inspection was performed in this study. The geometry was also not extensively compared with other geometries to spot deviations in the geometry.

Boundary conditions are important in the behaviour of the flow. It is assumed that the nostril inlet is a uniform flow and the trachea inlet is fully developed. This is a simplification of the real situation. An extended inlet was used during inspiration causing the inflow to be not fully uniform. The simulations can be improved by a more accurate description of the boundary conditions, which can for example be obtained by conducting experiments with stereoscopic particle image velocimetry on the same geometry [87]. The obtained velocity profile at the boundary conditions can then be used as an input in the inflow boundary condition. An error was made by prescribing the flow rates at each nostril. The maximum difference between the left and right nostril was calculated to be 5.26%. In order to increase the accuracy and validity of this work, the flow rate function as described in section 5.4 should be re-evaluated. A good starting point would be to use the solution obtained at peak exhalation, 0.479 : 0.521 at 15 $\mathrm{L/min}$. Another possibility can be to merge the extended inlets in one single inlet, as has been seen in other studies. Since the geometry during inhalation is already extended, merging the inlets into one can cause natural development of the flow over the cavities.

Doorly et al. [15] stated that the geometry below the nasopharynx impresses during exhalation, something no model has incorporated up till this moment. Other simplifications made in both the numerical study and the experimental set-up is the absence of mucous and cilia. A rigid, no-slip wall was assumed in the simulations at the complete wall, though some parts in the geometry are in fact compliant [31]. Fodil et al. [21] studied the influence of the assumption of a rigid model versus a compliant model in the nasal geometry and stated that the nostril resistance differs significantly for high pressures (up to 300Pa) but is within limits for the pressures obtained in this work.

A more solid statement about the quality of the study can be made by performing a more extensive grid convergence study and simulate for different values of τ. In this way, a prediction of the discretization error can be made. Performing the grid convergence study and simulating for different τ costs a lot of time and resources, making it possibly not worth to put real effort in this.

As mentioned before in the discussion of chapter 6, a LES turbulence model was used. A positive non-zero turbulent viscosity is therefore added, even in laminar flow. Airflow in the nasal cavities is often stated to be laminar for flow rates lower than 15L/min [14, 35, 112]. Direct numerical simulation in Lattice Boltzmann is possible and can add value by capturing the laminar, transitional and turbulent flow. There is a good chance that DNS is possible in the unassisted breathing and NHFT simulations if local grid refinement is used or more resources are available. Especially when more geometries are simulated, a really solid statement can be made about the types of flow in the upper respiratory tract. An alternative solution might be to perform DNS on low flow rates and LES at higher flow rates.

Pressure results were directly compared with experiments using the same geometry, one of the strengths of this research. The comparison could be made stronger by elaborating on the measured results. Standard deviations of the obtained means and maxima can be calculated to make more solid statements on the experimental results.

A method of simulating NHFT using the LBM was proposed in chapter 7. The challenges that come with them are also discussed. It is assumed that the breathing profile in the trachea is the same during unassisted breathing and NHFT. Several studies show that this is not the case and the breathing behaviour changes during NHFT [8, 61, 74]. The exact quantification on how this breathing profile changes is not yet known, but should be incorporated when found.

One of the working mechanics of NHFT is the supply of humidified and heated air. The temperature of airflow that enters the nose during unassisted breathing is dependent on the atmospheric temperature, which can vary. During NHFT, heated, humidified air is supplied which has not only other air properties, but also other thermal effects on the nose. In this study, no attempts are made to imply the effects such as heating the air during unassisted breathing to body temperature and humidification. Simulations that investigate this behaviour have been performed in the past and can contribute to quantify the effects of NHFT [47, 102].

9 | Conclusion

The purpose of this study is to help understanding the working mechanics of Nasal High Flow Therapy. By understanding the working mechanics, it might me be possible to find optimal patient settings which can significantly help treating patients with COPD.

The Lattice Boltzmann method has been used, since it is able to simulate flow in complex geometries such as the upper respiratory tract. Simulations in this work are performed with the LBM solver musubi. The Lattice Boltzmann method is compared with the Finite Volume and Finite Element Method. The comparison with the FVM was made by simulating the flow in a 2D-benchmark case of flow over a cylinder using musubi and Ansys Fluent. This allowed direct comparison of the visual and numerical results. The flow in a femoral artery bifurcation has been simulated to compare LBM with SimVascular. Both comparison cases show good agreement and the Lattice Boltzmann method shows to be able to accurately capture vortices, lift and drag coefficients and general flow and pressure contours. Both cases were also used to study the influence of the relaxation parameter and different pressure boundary conditions.

To clearly study the effect of Nasal High Flow Therapy, the flow behaviour during unassisted breathing has been studied by performing transient Large Eddy Simulations on a very high resolution mesh. A realistic geometry has been used that was created from the CT-scan of an adult male with closed mouth. Contrary to many earlier studies, the geometry includes all paranasal sinuses and the complete upper respiratory tract from the nostrils up till the trachea. Transient Large Eddy Simulations with a realistic model have not been studied often. A structured mesh with approximately 1000M cells was created and used, which is possibly the highest resolution mesh used to simulate tidal breathing.

An unconventional method in describing the boundary conditions was used at the nostril during inhalation. Rather then equaling the flow rate at each nostril, an estimation of the flow rate distribution over the cavities, based on 27 scaled test cases, was used. Using this method, it is possible to equal the pressure in both nostrils. An error was made in this method, resulting in a maximum pressure difference of 5% between the nostrils.

Extended inlets and outlets were needed to prevent numerical artifacts and instabilities during inhalation. Multi-relaxation has been used in the Lattice Boltzmann method to increase stability. Outlets were prescribed as zero pressure outlet. During expiration, a fully developed flow is prescribed at the trachea. The wall was regarded rigid with a no-slip condition. The Large Eddy simulations captured pharyngeal and laryngeal jets with high velocities in both inspiration and expiration. Recirculation zones were observed near the jets, as well as in the olfactory region during inhalation. Experiments were conducted parallel to the numerical simulations in the same geometry and results were therefore directly comparable. The pressure drop was measured at several points in the geometry and directly compared with pressure drop results from the experiments, which showed good agreement.

Simulating the airflow during Nasal High Flow Therapy was not succeeded. The main reason for this is the high lattice Mach numbers that are calculated during Nasal High Flow Therapy, which can possibly be resolved by local grid refinements. Implementing local grid refinements should be the main focus point to make Lattice Boltzmann simulations in Nasal High Flow Therapy work. It is also recommended to implement a method of tracking particles in order to study the wash-out effects of Nasal High Flow Therapy.

There are many similarities in the approach of NHFT simulations and the unassisted breathing simulations performed in this work. This work therefore paves the path towards Nasal High Flow Therapy simulations using Lattice Boltzmann. The simulations of unassisted breathing provide insights and visualizations which can later be used to compare with Nasal High Flow Therapy simulations, therefore helping to understand the mechanics of Nasal High Flow Therapy. Regions with high velocities are identified which is useful for future Nasal High Flow Therapy simulations that use local grid refinements. This work shows a very detailed flow solution of tidal breathing due to the high resolution mesh and Large Eddy simulations and therefore has the potential to serve as a benchmark for the validation of coarser simulations.

Bibliography

[1] Cletus F. Adams, Patrick H. Geoghegan, Callum J. Spence, and Mark C. Jermy. Modelling nasal high flow therapy effects on upper airway resistance and resistive work of breathing. *Respiratory Physiology and Neurobiology*, 254:23 – 29, 2018. ISSN 1569-9048. doi: https://doi.org/10.1016/j.resp.2018.03.014. URL `http://www.sciencedirect.com/science/article/pii/S1569904817304500`.

[2] H. Aly, Khalid Saqr, Yehia Eldrainy, and Mohammad Nazri Mohd Jaafar. Can large eddy simulation (les) predict laminar to turbulent flow transition? *International Journal of Mechanical and Materials Engineering*, 4, 06 2009.

[3] A. J. Banko, F. Coletti, D. Schiavazzi, C. J. Elkins, and J. K. Eaton. Three-dimensional inspiratory flow in the upper and central human airways. *Experiments in Fluids*, 56(6):117, May 2015. ISSN 1432-1114. doi: 10.1007/s00348-015-1966-y. URL `https://doi.org/10.1007/s00348-015-1966-y`.

[4] A. J. Bates, D. J. Doorly, R. Cetto, H. Calmet, A. M. Gambaruto, N. S. Tolley, G. Houzeaux, and R. C. Schroter. Dynamics of airflow in a short inhalation. *Journal of The Royal Society Interface*, 12(102):20140880, 2015. doi: 10.1098/rsif.2014.0880. URL `https://royalsocietypublishing.org/doi/abs/10.1098/rsif.2014.0880`.

[5] M Beigzadeh-Abbassi, Moha Taeibi-Rahni, M Beigzadeh-Abbassi, and A Beigzadeh-Abbassi. A comparative study of three different bounce-back scheme based methods for a moving curved solid boundary implementation in the lattice boltzmann method a comparative study of three different bounce-back scheme based methods for a moving curved solid boundary implementation in the lattice boltzmann method. *Journal of American Science*, 8, 01 2012.

[6] Gila Benchetrit. Breathing pattern in humans: diversity and individuality. *Respiration Physiology*, 122(2):123 – 129, 2000. ISSN 0034-5687. doi: https://doi.org/10.1016/S0034-5687(00)00154-7. URL `http://www.sciencedirect.com/science/article/pii/S0034568700001547`.

[7] P. L. Bhatnagar, E. P. Gross, and M. Krook. A model for collision processes in gases. i. small amplitude processes in charged and neutral one-component systems. *Phys. Rev.*, 94:511–525, May 1954. doi: 10.1103/PhysRev.94.511. URL `https://link.aps.org/doi/10.1103/PhysRev.94.511`.

[8] Paolo J. C. Biselli, Jason P. Kirkness, Ludger Grote, Kathrin Fricke, Alan R. Schwartz, Philip Smith, and Hartmut Schneider. Nasal high-flow therapy reduces work of breathing compared with oxygen during sleep in COPD and smoking controls: a prospective observational study. *Journal of Applied Physiology*, 122(1):82–88, January 2017. doi: 10.1152/japplphysiol.00279.2016. URL `https://doi.org/10.1152/japplphysiol.00279.2016`.

[9] Bruce Blaus. Medical gallery of blausen medical 2014. *WikiJournal of Medicine*, 1(2), 2014. doi: 10.15347/wjm/2014.010. URL `https://doi.org/10.15347/wjm/2014.010`.

[10] M'hamed Bouzidi, Mouaouia Firdaouss, and Pierre Lallemand. Momentum transfer of a boltzmann-lattice fluid with boundaries. *Physics of Fluids*, 13(11):3452–3459, 2001. doi: 10.1063/1.1399290. URL `https://doi.org/10.1063/1.1399290`.

[11] Jan Brüning, Thomas Hildebrandt, Werner Heppt, Nora Schmidt, Hans Lamecker, Angelika Szengel, Natalja Amiridze, Heiko Ramm, Matthias Bindernagel, Stefan Zachow, and Leonid Goubergrits. Characterization of the airflow within an average geometry of the healthy human nasal cavity. *Scientific Reports*, 10(1):3755, Feb 2020. ISSN 2045-2322. doi: 10.1038/s41598-020-60755-3. URL `https://doi.org/10.1038/s41598-020-60755-3`.

[12] Ernesto Crisafulli, Enric Barbeta, Antonella Ielpo, and Antoni Torres. Management of severe acute exacerbations of copd: an updated narrative review. *Multidisciplinary respiratory medicine*, 13:36–36, Oct 2018. ISSN 1828-695X. doi: 10.1186/s40248-018-0149-0. URL `https://pubmed.ncbi.nlm.nih.gov/30302247`. 30302247[pmid].

[13] Paul J. Dellar. Incompressible limits of lattice boltzmann equations using multiple relaxation times. *Journal of Computational Physics*, 190(2):351 – 370, 2003. ISSN 0021-9991. doi: https://doi.org/10.1016/S0021-9991(03)00279-1. URL `http://www.sciencedirect.com/science/article/pii/S0021999103002791`.

[14] D Doorly, D J Taylor, P Franke, and R C Schroter. Experimental investigation of nasal airflow. *Proceedings of the Institution of Mechanical Engineers, Part H: Journal of Engineering in Medicine*, 222(4):439–453, 2008. doi: 10.1243/09544119JEIM330. URL `https://doi.org/10.1243/09544119JEIM330`. PMID: 18595356.

[15] D.J. Doorly, D.J. Taylor, and R.C. Schroter. Mechanics of airflow in the human nasal airways. *Respiratory Physiology and Neurobiology*, 163(1):100 – 110, 2008. ISSN 1569-9048. doi: https://doi.org/10.1016/j.resp.2008.07.027. URL `http://www.sciencedirect.com/science/article/pii/S1569904808002140`. Respiratory Biomechanics.

[16] Kevin Dysart, Thomas Miller, Marla Wolfson, and Thomas Shaffer. Research in high flow therapy: Mechanisms of action. *Respiratory medicine*, 103:1400–5, 06 2009. doi: 10.1016/j.rmed.2009.04.007.

[17] Jakub Elcner, Jan Jedelsky, Frantisek Lizal, and Miroslav Jicha. Velocity profiles in idealized model of human respiratory tract. *The European Physical Journal Conferences*, 45, 04 2013. doi: 10.1051/epjconf/20134501025.

[18] embodi3D.com. Easily Create 3D Printable Muscle and Skin STL Files from Medical CT Scans. https://www.embodi3d.com/blogs/entry/353-easily-create-3d-printable-muscle-and-skin-stl-files-from-medical-ct-scans/, October 2016.

[19] Y. Feng, Kook Han, and D.R.sJ. Owen. Coupled lattice boltzmann method and discrete element modeling of particle transport in turbulent fluid flows: Computational issues. *International Journal for Numerical Methods in Engineering*, 72:1111 – 1134, 11 2007. doi: 10.1002/nme.2114.

[20] M. Finck, D. Hänel, and I. Wlokas. Simulation of nasal flow by lattice boltzmann methods. *Computers in Biology and Medicine*, 37(6):739 – 749, 2007. ISSN 0010-4825. doi: https://doi.org/10.1016/j.compbiomed.2006.06.013. URL `http://www.sciencedirect.com/science/article/pii/S0010482506000965`.

[21] Redouane Fodil, Lydia Brugel-Ribere, Céline Croce, Gabriela Sbirlea-Apiou, Christian Larger, Jean-François Papon, Christophe Delclaux, André Coste, Daniel Isabey, and Bruno Louis. Inspiratory flow in the nose: a model coupling flow and vasoerectile tissue distensibility. *Journal of Applied Physiology*, 98(1):288–295, 2005. doi: 10.1152/japplphysiol.00625.2004. URL `https://doi.org/10.1152/japplphysiol.00625.2004`. PMID: 15333615.

[22] U. Frisch, B. Hasslacher, and Y. Pomeau. Lattice-gas automata for the navier-stokes equation. *Phys. Rev. Lett.*, 56:1505–1508, Apr 1986. doi: 10.1103/PhysRevLett.56.1505. URL `https://link.aps.org/doi/10.1103/PhysRevLett.56.1505`.

[23] F.J.H. Gijsen, F.N. van de Vosse, and J.D. Janssen. The influence of the non-newtonian properties of blood on the flow in large arteries: steady flow in a carotid bifurcation model. *Journal of Biomechanics*, 32(6):601 – 608, 1999. ISSN 0021-9290. doi: https://doi.org/10.1016/S0021-9290(99)00015-9. URL `http://www.sciencedirect.com/science/article/pii/S0021929099000159`.

[24] Emmanuelle Girou, Christian Brun-Buisson, Solenne Taillé, François Lemaire, and Laurent Brochard. Secular Trends in Nosocomial Infections and Mortality Associated With Noninvasive Ventilation in Patients With Exacerbation of COPD and Pulmonary Edema. *JAMA*, 290(22):2985–2991, 12 2003. ISSN 0098-7484. doi: 10.1001/jama.290.22.2985. URL `https://doi.org/10.1001/jama.290.22.2985`.

[25] George V. Guibas and Nikolaos G. Papadopoulos. *Viral Upper Respiratory Tract Infections*, pages 1–25. Springer International Publishing, Cham, 2017. ISBN 978-3-319-54093-1. doi: 10.1007/978-3-319-54093-1_1. URL `https://doi.org/10.1007/978-3-319-54093-1_1`.

[26] Farzaneh Hajabdollahi and Kannan N. Premnath. Improving the low mach number steady state convergence of the cascaded lattice boltzmann method by preconditioning. *Computers and Mathematics with Applications*, 78(4):1115 – 1130, 2019. ISSN 0898-1221. doi: https://doi.org/10.1016/j.camwa.2016.12.034. URL `http://www.sciencedirect.com/science/article/pii/S0898122117300664`. ICMMES-2015.

[27] Iram Haq, Saikiran Gopalakaje, Alan C. Fenton, Michael C. McKean, Christopher J. O'Brien, and Malcolm Brodlie. The evidence for high flow nasal cannula devices in infants. *Paediatric Respiratory Reviews*, 15(2): 124 – 134, 2014. ISSN 1526-0542. doi: https://doi.org/10.1016/j.prrv.2013.12.002. URL http://www.sciencedirect.com/science/article/pii/S1526054213001553.

[28] M. Hasert. *Multi-scale Lattice Boltzmann simulations on distributed octrees*. PhD thesis, Aachen University, 2013.

[29] Manuel Hasert, Kannan Masilamani, Simon Zimny, Harald Klimach, Jiaxing Qi, Jörg Bernsdorf, and Sabine Roller. Complex fluid simulations with the parallel tree-based lattice Boltzmann solver Musubi. *Journal of Computational Science*, 5(5):784–794, 2014.

[30] Dean R Hess. Noninvasive ventilation for acute respiratory failurediscussion. *Respiratory Care*, 58(6):950–972, 2013. ISSN 0020-1324. doi: 10.4187/respcare.02319. URL http://rc.rcjournal.com/content/58/6/950.

[31] S. C. Van Hove, J. Storey, C. Adams, K. Dey, P. H. Geoghegan, N. Kabaliuk, S. D. Oldfield, C. J. T. Spence, M. C. Jermy, V. Suresh, and J. E. Cater. An experimental and numerical investigation of CO2 distribution in the upper airways during nasal high flow therapy. *Annals of Biomedical Engineering*, 44(10):3007–3019, April 2016. doi: 10.1007/s10439-016-1604-8. URL https://doi.org/10.1007/s10439-016-1604-8.

[32] I Hörschler, M Meinke, and W Schröder. Numerical simulation of the flow field in a model of the nasal cavity. *Computers & Fluids*, 32(1):39 – 45, 2003. ISSN 0045-7930. doi: https://doi.org/10.1016/S0045-7930(01)00097-4. URL http://www.sciencedirect.com/science/article/pii/S0045793001000974.

[33] Ingolf Hörschler, Wolfgang Schröder, and Matthias Meinke. On the assumption of steadiness of nasal cavity flow. *Journal of biomechanics*, 43:1081–5, 04 2010. doi: 10.1016/j.jbiomech.2009.12.008.

[34] ANSYS Inc. Ansys fluent theory guide. 2019. ansysinfo@ansys.com ANSYS Europe.

[35] Kiao Inthavong, Jiawei Ma, Yidan Shang, Jingliang Dong, Annicka S.R. Chetty, Jiyuan Tu, and Dennis Frank-Ito. Geometry and airflow dynamics analysis in the nasal cavity during inhalation. *Clinical Biomechanics*, 66: 97 – 106, 2019. ISSN 0268-0033. doi: https://doi.org/10.1016/j.clinbiomech.2017.10.006. URL http://www.sciencedirect.com/science/article/pii/S0268003317302188. SI: Clinical Relevance of Respiratory Mechanics and Flows.

[36] Kartik Jain. *Transition to Turbulence in Physiological Flows: Direct Numerical Simulation of Hemodynamics in Intracranial Aneurysms and Cerebrospinal Fluid Hydrodynamics in the Spinal Canal*. PhD thesis, Universitat Siegen, Germany, September 2016.

[37] Kartik Jain. Efficacy of the fda nozzle benchmark and the lattice boltzmann method for the analysis of biomedical flows in transitional regime. *Medical & Biological Engineering & Computing*, 58(8):1817–1830, Aug 2020. ISSN 1741-0444. doi: 10.1007/s11517-020-02188-8. URL https://doi.org/10.1007/s11517-020-02188-8.

[38] Mitchel Johnson, Daniel Playne, and Ken Hawick. Data-parallelism and gpus for lattice gas fluid simulations. pages 210–216, 01 2010.

[39] Michael Junk and Zhaoxia Yang. Asymptotic analysis of lattice boltzmann outflow treatments. *Communications in Computational Physics*, 9, 05 2011. doi: 10.4208/cicp.091009.290910s.

[40] Harald Klimach, Kartik Jain, and Sabine Roller. End-to-end parallel simulations with apes. In *Parallel Computing: Accelerating Computational Science and Engineering (CSE)*, volume 25, pages 703–711, 2014.

[41] Timm Krüger, Halim Kusumaatmaja, Alexander Kuzmin, Orest Shardt, Goncalo Silva, and Erlend Magnus Viggen. *The Lattice Boltzmann Method - Principles and Practice*. Springer International Publishing, 10 2016. ISBN 978-3-319-44647-9. doi: 10.1007/978-3-319-44649-3.

[42] D. Kumar, R. Vinoth, Adhikari Raviraj, and C. 19 S. Vijay Shankar. Non-newtonian and newtonian blood flow in human aorta: A transient analysis. *Biomedical Research*, 28(7):3194–3203, 1 2017. ISSN 0970-938X.

[43] Haribalan Kumar, Callum J.T. Spence, and Merryn H. Tawhai. Modeling the pharyngeal pressure during adult nasal high flow therapy. *Respiratory Physiology & Neurobiology*, 219:51–57, December 2015. doi: 10.1016/j.resp.2015.06.011. URL https://doi.org/10.1016/j.resp.2015.06.011.

[44] J. Rudi K.M. Latt. Choice of units in lattice boltzmann simulations. 2008.

[45] Like Li. Multiple-time-scaling lattice boltzmann method for the convection diffusion equation. *Physical Review E*, 99, 06 2019. doi: 10.1103/PhysRevE.99.063301.

[46] Ching-Long Lin, Merryn H. Tawhai, Geoffrey McLennan, and Eric A. Hoffman. Characteristics of the turbulent laryngeal jet and its effect on airflow in the human intra-thoracic airways. *Respiratory physiology & neurobiology*, 157(2-3):295–309, Aug 2007. ISSN 1569-9048. doi: 10.1016/j.resp.2007.02.006. URL `https://pubmed.ncbi.nlm.nih.gov/17360247`. 17360247[pmid].

[47] Andreas Lintermann, Matthias Meinke, and Wolfgang Schröder. Fluid mechanics based classification of the respiratory efficiency of several nasal cavities. *Computers in Biology and Medicine*, 43(11):1833 – 1852, 2013. ISSN 0010-4825. doi: https://doi.org/10.1016/j.compbiomed.2013.09.003. URL `http://www.sciencedirect.com/science/article/pii/S0010482513002540`.

[48] Xingli Liu, Weiwei Yan, Yang Liu, Yat Sze Choy, and Yikun Wei. Numerical investigation of flow characteristics in the obstructed realistic human upper airway. *Computational and Mathematical Methods in Medicine*, 2016: 3181654, Sep 2016. ISSN 1748-670X. doi: 10.1155/2016/3181654. URL `https://doi.org/10.1155/2016/3181654`.

[49] A. B. Lumb and C. R. Thomas. High-flow nasal therapy - modelling the mechanism. *Anaesthesia*, 74(4):420–423, February 2019. doi: 10.1111/anae.14544. URL `https://doi.org/10.1111/anae.14544`.

[50] Jing-chao Luo, Mei-shan Lu, Zhi-hong Zhao, Wei Jiang, Biao Xu, Li Weng, Tong Li, and Bin Du. Positive end-expiratory pressure effect of 3 high-flow nasal cannula devices. *Respiratory Care*, 62(7):888–895, 2017. ISSN 0020-1324. doi: 10.4187/respcare.05337. URL `http://rc.rcjournal.com/content/62/7/888`.

[51] Emily L. Manchester and Xiao Yun Xu. The effect of turbulence on transitional flow in the fda's benchmark nozzle model using large-eddy simulation. *International Journal for Numerical Methods in Biomedical Engineering*, 36 (10):e3389, 2020. doi: https://doi.org/10.1002/cnm.3389. URL `https://onlinelibrary.wiley.com/doi/abs/10.1002/cnm.3389`.

[52] T. B. Martonen, Z. Zhang, and R. C. Lessmann. Fluid dynamics of the human larynx and upper tracheobronchial airways. *Aerosol Science and Technology*, 19(2):133–156, 1993. doi: 10.1080/02786829308959627. URL `https://doi.org/10.1080/02786829308959627`.

[53] T. B. Martonen, Z. Zhang, and R. C. Lessmann. Fluid dynamics of the human larynx and upper tracheobronchial airways. *Aerosol Science and Technology*, 19(2):133–156, 1993. doi: 10.1080/02786829308959627. URL `https://doi.org/10.1080/02786829308959627`.

[54] Steven McKinstry, Joseph Singer, Jan Pieter Baarsma, Mark Weatherall, Richard Beasley, and James Fingleton. Nasal high-flow therapy compared with non-invasive ventilation in copd patients with chronic respiratory failure: A randomized controlled cross-over trial. *Respirology*, 24(11):1081–1087, 2019. doi: 10.1111/resp.13575. URL `https://onlinelibrary.wiley.com/doi/abs/10.1111/resp.13575`.

[55] Mihai Mihaescu, Shanmugam Murugappan, Maninder Kalra, Sid Khosla, and Ephraim Gutmark. Large eddy simulation and reynolds-averaged navier–stokes modeling of flow in a realistic pharyngeal airway model: An investigation of obstructive sleep apnea. *Journal of Biomechanics*, 41(10):2279 – 2288, 2008. ISSN 0021-9290. doi: https://doi.org/10.1016/j.jbiomech.2008.04.013. URL `http://www.sciencedirect.com/science/article/pii/S0021929008001942`.

[56] A. A. Mohamad. *Lattice Boltzmann Method Fundamentals and Engineering Applications with Computer Codes*. Springer-Verlag London, 2011. ISBN 978-0-85729-455-5. doi: 10.1007/978-0-85729-455-5.

[57] Winfried Möller, Gülnaz Celik, Sheng Feng, Peter Bartenstein, Gabriele Meyer, Oliver Eickelberg, Otmar Schmid, and Stanislav Tatkov. Nasal high flow clears anatomical dead space in upper airway models. *Journal of Applied Physiology*, 118(12):1525–1532, June 2015. doi: 10.1152/japplphysiol.00934.2014. URL `https://doi.org/10.1152/japplphysiol.00934.2014`.

[58] Winfried Möller, Sheng Feng, Ulrike Domanski, Karl-Josef Franke, Gülnaz Celik, Peter Bartenstein, Sven Becker, Gabriele Meyer, Otmar Schmid, Oliver Eickelberg, Stanislav Tatkov, and Georg Nilius. Nasal high flow reduces dead space. *Journal of Applied Physiology*, 122(1):191–197, January 2017. doi: 10.1152/japplphysiol.00584.2016. URL `https://doi.org/10.1152/japplphysiol.00584.2016`.

[59] Charles P. Moore, Ira M. Katz, Georges Caillibotte, Warren H. Finlay, and Andrew R. Martin. Correlation of high flow nasal cannula outlet area with gas clearance and pressure in adult upper airway replicas. *Clinical Biomechanics*, 66:66–73, June 2019. doi: 10.1016/j.clinbiomech.2017.11.003. URL `https://doi.org/10.1016/j.clinbiomech.2017.11.003`.

[60] C.P. Moore, I.M. Katz, M. Pichelin, G. Caillibotte, W.H. Finlay, and A.R. Martin. High flow nasal cannula: Influence of gas type and flow rate on airway pressure and CO2 clearance in adult nasal airway replicas. *Clinical Biomechanics*, 65:73–80, May 2019. doi: 10.1016/j.clinbiomech.2019.04.004. URL `https://doi.org/10.1016/j.clinbiomech.2019.04.004`.

[61] Toby Mündel, Sheng Feng, Stanislav Tatkov, and Hartmut Schneider. Mechanisms of nasal high flow on ventilation during wakefulness and sleep. *Journal of Applied Physiology*, 114(8):1058–1065, April 2013. doi: 10.1152/japplphysiol.01308.2012. URL `https://doi.org/10.1152/japplphysiol.01308.2012`.

[62] Toby Mundel, Sheng Feng, Stanislav Tatkov, and Hartmut Schneider. Mechanisms of nasal high flow on ventilation during wakefulness and sleep. *Journal of applied physiology (Bethesda, Md. : 1985)*, 114, 02 2013. doi: 10.1152/japplphysiol.01308.2012.

[63] Niels Mygind and Ronald Dahl. Anatomy, physiology and function of the nasal cavities in health and disease. *Advanced Drug Delivery Reviews*, 29(1-2):3–12, January 1998. doi: 10.1016/s0169-409x(97)00058-6. URL `https://doi.org/10.1016/s0169-409x(97)00058-6`.

[64] Niels Mygind and Ronald Dahl. Anatomy, physiology and function of the nasal cavities in health and disease. *Advanced Drug Delivery Reviews*, 29(1):3 – 12, 1998. ISSN 0169-409X. doi: https://doi.org/10.1016/S0169-409X(97)00058-6. URL `http://www.sciencedirect.com/science/article/pii/S0169409X97000586`. Nasal Drug Delivery.

[65] Yang Na, Seung-Kyu Chung, and Seongsu Byun. Numerical study on the heat-recovery capacity of the human nasal cavity during expiration. *Computers in Biology and Medicine*, 126:103992, 2020. ISSN 0010-4825. doi: https://doi.org/10.1016/j.compbiomed.2020.103992. URL `http://www.sciencedirect.com/science/article/pii/S0010482520303231`.

[66] Alireza Nejati, Natalia Kabaliuk, Mark C. Jermy, and John E. Cater. A deformable template method for describing and averaging the anatomical variation of the human nasal cavity. *BMC Medical Imaging*, 16(1): 55, Oct 2016. ISSN 1471-2342. doi: 10.1186/s12880-016-0154-8. URL `https://doi.org/10.1186/s12880-016-0154-8`.

[67] Katie R Nielsen, Laura E Ellington, Alan J Gray, Larissa I Stanberry, Lincoln S Smith, and Robert M DiBlasi. Effect of high-flow nasal cannula on expiratory pressure and ventilation in infant, pediatric, and adult models. *Respiratory Care*, 63(2):147–157, 2018. ISSN 0020-1324. doi: 10.4187/respcare.05728. URL `http://rc.rcjournal.com/content/63/2/147`.

[68] M. Nishimura. High-flow nasal cannula oxygen therapy in adults: Physiological benefits, indication, clinical benefits, and adverse effects. *Respiratory Care*, 61(4):529–541, March 2016. doi: 10.4187/respcare.04577. URL `https://doi.org/10.4187/respcare.04577`.

[69] Masaji Nishimura. High-flow nasal cannula oxygen therapy in adults. *Journal of Intensive Care*, 3(1), March 2015. doi: 10.1186/s40560-015-0084-5. URL `https://doi.org/10.1186/s40560-015-0084-5`.

[70] Masaji Nishimura. High-flow nasal cannula oxygen therapy devices. *Respiratory Care*, 64(6):735–742, 2019. ISSN 0020-1324. doi: 10.4187/respcare.06718. URL `http://rc.rcjournal.com/content/64/6/735`.

[71] R.R. Nourgaliev, T.N. Dinh, T.G. Theofanous, and D. Joseph. The lattice boltzmann equation method: theoretical interpretation, numerics and implications. *International Journal of Multiphase Flow*, 29(1):117 – 169, 2003. ISSN 0301-9322. doi: https://doi.org/10.1016/S0301-9322(02)00108-8. URL `http://www.sciencedirect.com/science/article/pii/S0301932202001088`.

[72] Government of Canada. Chronic obstructive pulmonary disease (copd), 2019. URL `https://www.canada.ca/en/public-health/services/chronic-diseases/chronic-respiratory-diseases/chronic-obstructive-pulmonary-disease-copd.html`.

[73] R. L. Parke, M. L. Eccleston, and S. P. McGuinness. The effects of flow on airway pressure during nasal high-flow oxygen therapy. *Respiratory Care*, 56(8):1151–1155, August 2011. doi: 10.4187/respcare.01106. URL `https://doi.org/10.4187/respcare.01106`.

[74] Maximilian Pinkham, Russel Burgess, Toby Mündel, and Stanislav Tatkov. Nasal high flow reduces minute ventilation during sleep through a decrease of carbon dioxide rebreathing. *Journal of Applied Physiology*, 126(4):863–869, April 2019. doi: 10.1152/japplphysiol.01063.2018. URL https://doi.org/10.1152/japplphysiol.01063.2018.

[75] Aniruddhe Pradhan and Sumedh Yadav. Large eddy simulation using lattice boltzmann method based on sigma model. *Procedia Engineering*, 127, 12 2015. doi: 10.1016/j.proeng.2015.11.324.

[76] D. F. Proctor. Airborne disease and the upper respiratory tract. *Bacteriological reviews*, 30(3):498–513, Sep 1966. ISSN 0005-3678. URL https://pubmed.ncbi.nlm.nih.gov/5331172. 5331172[pmid].

[77] Jiaxing Qi, Kartik Jain, Harald Klimach, and Sabine Roller. Performance evaluation of the LBM solver Musubi on various HPC architectures. In *Advances in Parallel Computing: On the Road to Exascale*, volume 27 of *Advances in Parallel Computing*, pages 807–816. IOS Press, March 2016. doi: https://doi.org/10.3233/978-1-61499-621-7-807.

[78] C. Raherison and P-O Girodet. Epidemiology of copd. *European Respiratory Review*, 18(114):213–221, 2009. ISSN 0905-9180. doi: 10.1183/09059180.00003609. URL https://err.ersjournals.com/content/18/114/213.

[79] Jerry Ratzlaff, 2018. URL https://www.piping-designer.com/index.php/properties/fluid-mechanics/2250-hydraulic-diameter-of-an-ellipse.

[80] Vizy Nazira Riazuddin, Mohammad Zuber, M.Z. Abdullah, Rushdan Ismail, Ibrahim Lutfi Shuaib, Suzina Sheikh Ab Hamid, and Kamarul Ahmad. Numerical study of inspiratory and expiratory flow in a human nasal cavity. *Journal of Medical and Biological Engineering*, 31:201–206, 09 2010. doi: 10.5405/jmbe.781.

[81] Nuttapol Rittayamai, Prapinpa Phuangchoei, Jamsak Tscheikuna, Nattakarn Praphruetkit, and Laurent Brochard. Effects of high-flow nasal cannula and non-invasive ventilation on inspiratory effort in hypercapnic patients with chronic obstructive pulmonary disease: a preliminary study. *Annals of Intensive Care*, 9(1), October 2019. doi: 10.1186/s13613-019-0597-5. URL https://doi.org/10.1186/s13613-019-0597-5.

[82] Oriol Roca, Jordi Riera, Ferran Torres, and Joan R Masclans. High-flow oxygen therapy in acute respiratory failure. *Respiratory Care*, 55(4):408–413, 2010. ISSN 0020-1324. URL http://rc.rcjournal.com/content/55/4/408.

[83] Sabine Roller, Jörg Bernsdorf, Harald Klimach, Manuel Hasert, Daniel Harlacher, Metin Cakircali, Simon Zimny, Kannan Masilamani, Laura Didinger, and Jens Zudrop. An adaptable simulation framework based on a linearized octree. In *High Performance Computing on Vector Systems 2011*, pages 93–105. Springer-Verlag Berlin Heidelberg, 2012. ISBN 978-3-642-22244-3.

[84] M. Schäfer, S. Turek, F. Durst, E. Krause, and R. Rannacher. *Benchmark Computations of Laminar Flow Around a Cylinder*, pages 547–566. Vieweg+Teubner Verlag, Wiesbaden, 1996. ISBN 978-3-322-89849-4. doi: 10.1007/978-3-322-89849-4_39. URL https://doi.org/10.1007/978-3-322-89849-4_39.

[85] Andreas Schneider. *A Consistent Large Eddy Approach for Lattice Boltzmann Methods and its Application to Complex Flows*. doctoralthesis, Technische Universität Kaiserslautern, 2015. URL http://nbn-resolving.de/urn:nbn:de:hbz:386-kluedo-40568.

[86] Franz Schwabl. *The Boltzmann Equation*, pages 437–478. Springer Berlin Heidelberg, Berlin, Heidelberg, 2006. ISBN 978-3-540-36217-3. doi: 10.1007/3-540-36217-7_9. URL https://doi.org/10.1007/3-540-36217-7_9.

[87] C. J. T. Spence, N. A. Buchmann, M. C. Jermy, and S. M. Moore. Stereoscopic PIV measurements of flow in the nasal cavity with high flow therapy. *Experiments in Fluids*, 50(4):1005–1017, September 2010. doi: 10.1007/s00348-010-0984-z. URL https://doi.org/10.1007/s00348-010-0984-z.

[88] Giulia Spoletini and Nicholas S. Hill. High-flow nasal oxygen versus noninvasive ventilation for hypoxemic respiratory failure: Do we know enough? *Annals of thoracic medicine*, 11(3):163–166, 2016. ISSN 1817-1737. doi: 10.4103/1817-1737.185760. URL https://pubmed.ncbi.nlm.nih.gov/27512504. 27512504[pmid].

[89] S. Succi. *The Lattice Boltzmann Equation: For Fluid Dynamics and Beyond*. Numerical mathematics and scientific computation. Oxford University Press, 2013. ISBN 9780191761348. URL https://books.google.nl/books?id=b_YSnQAACAAJ.

[90] Michael C. Sukop and Daniel T. Thorne Jr. *Lattice Boltzmann Modeling*. Springer, Berlin, Heidelberg, 2006. ISBN 978-3-540-27981-5. doi: https://doi.org/10.1007/978-3-540-27982-2.

[91] Reza Tabe, Roohollah Rafee, Mohammad Sadegh Valipour, and Goodarz Ahmadi. Investigation of airflow at different activity conditions in a realistic model of human upper respiratory tract. *Computer Methods in Biomechanics and Biomedical Engineering*, 0(0):1–15, 2020. doi: 10.1080/10255842.2020.1819256. URL https://doi.org/10.1080/10255842.2020.1819256. PMID: 32940084.

[92] D. J. Taylor, D. J. Doorly, and R. C. Schroter. Inflow boundary profile prescription for numerical simulation of nasal airflow. *Journal of The Royal Society Interface*, 7(44):515–527, 2010. doi: 10.1098/rsif.2009.0306. URL https://royalsocietypublishing.org/doi/abs/10.1098/rsif.2009.0306.

[93] Lan-Fang Tung, Sheng-Yeh Shen, Hui-Hsuan Shih, Yen-Ting Chen, Chia-te Yen, and Shu-Chuan Ho. Effect of high-flow nasal therapy during early pulmonary rehabilitation in patients with severe aecopd: a randomized controlled study. *Respiratory Research*, 21(1):84, Apr 2020. ISSN 1465-993X. doi: 10.1186/s12931-020-1328-z. URL https://doi.org/10.1186/s12931-020-1328-z.

[94] Jonas Tölke, Giuseppe De Prisco, and Yaoming Mu. A lattice boltzmann method for immiscible two-phase stokes flow with a local collision operator. *Computers & Mathematics with Applications*, 65(6):864 – 881, 2013. ISSN 0898-1221. doi: https://doi.org/10.1016/j.camwa.2012.05.018. URL http://www.sciencedirect.com/science/article/pii/S0898122112004178. Mesoscopic Methods in Engineering and Science.

[95] Adam Updegrove, Nathan M. Wilson, Jameson Merkow, Hongzhi Lan, Alison L. Marsden, and Shawn C. Shadden. Simvascular: An open source pipeline for cardiovascular simulation. *Annals of Biomedical Engineering*, 45(3): 525–541, 2017. ISSN 1573-9686. doi: 10.1007/s10439-016-1762-8. URL https://doi.org/10.1007/s10439-016-1762-8.

[96] Lennart van de Velde. Computational fluid dynamics : a clinician's tool for femoral artery stenosis? Master thesis, University of Twente, 2018.

[97] Erlend Magnus Viggen. *The lattice Boltzmann method: Fundamentals and acoustics*. PhD thesis, Norwegian University of Science and Technology, 02 2014.

[98] Claus F. Vogelmeier, Miguel Román-Rodríguez, Dave Singh, MeiLan K. Han, Roberto Rodríguez-Roisin, and Gary T. Ferguson. Goals of copd treatment: Focus on symptoms and exacerbations. *Respiratory Medicine*, 166:105938, 2020. ISSN 0954-6111. doi: https://doi.org/10.1016/j.rmed.2020.105938. URL http://www.sciencedirect.com/science/article/pii/S0954611120300780.

[99] Ying Wang, Yingxi Liu, Xiuzhen Sun, Shen Yu, and Fei Gao. Numerical analysis of respiratory flow patterns within human upper airway. *Acta Mechanica Sinica*, 25(6):737, Aug 2009. ISSN 1614-3116. doi: 10.1007/s10409-009-0283-1. URL https://doi.org/10.1007/s10409-009-0283-1.

[100] Jian Wen, Kiao Inthavong, Jiyuan Tu, and Simin Wang. Numerical simulations for detailed airflow dynamics in a human nasal cavity. *Respiratory Physiology and Neurobiology*, 161(2):125 – 135, 2008. ISSN 1569-9048. doi: https://doi.org/10.1016/j.resp.2008.01.012. URL http://www.sciencedirect.com/science/article/pii/S1569904808000189.

[101] S.C. Wetstein. Implementing the lattice-boltzmann method. Bachelor's thesis, Delft University of Technology, 2014. retrieved at 10 march 2020.

[102] Jinxiang Xi, Xiuhua April Si, Haibo Dong, and Hualiang Zhong. Effects of glottis motion on airflow and energy expenditure in a human upper airway model. *European Journal of Mechanics - B/Fluids*, 72:23 – 37, 2018. ISSN 0997-7546. doi: https://doi.org/10.1016/j.euromechflu.2018.04.011. URL http://www.sciencedirect.com/science/article/pii/S0997754617304776.

[103] Zhenhua Xia, Yipeng Shi, Yu Chen, Moran Wang, and Shiyi Chen. Comparisons of different implementations of turbulence modelling in lattice boltzmann method. *Journal of Turbulence*, 16(1):67–80, 2015. doi: 10.1080/14685248.2014.954709. URL https://doi.org/10.1080/14685248.2014.954709.

[104] Guan-Xia Xiong, Jie-Min Zhan, Hong-Yan Jiang, Jian-Feng Li, Liang-Wan Rong, and Gen Xu. Computational fluid dynamics simulation of airflow in the normal nasal cavity and paranasal sinuses. *American Journal of Rhinology*, 22(5):477–482, September 2008. doi: 10.2500/ajr.2008.22.3211. URL https://doi.org/10.2500/ajr.2008.22.3211.

[105] Chang Xu, Nguyen Dang Khoa, Sung-Jun Yoo, Xin Zheng, Shifei Shen, and Kazuhide Ito. Inhalation airflow and ventilation efficiency in subject-specific human upper airways. *Respiratory Physiology & Neurobiology*, page 103587, 2020. ISSN 1569-9048. doi: https://doi.org/10.1016/j.resp.2020.103587. URL http://www.sciencedirect.com/science/article/pii/S1569904820302469.

[106] Xiaoyu Xu, Jialin Wu, Wenguo Weng, and Ming Fu. Investigation of inhalation and exhalation flow pattern in a realistic human upper airway model by piv experiments and cfd simulations. *Biomechanics and Modeling in Mechanobiology*, Feb 2020. ISSN 1617-7940. doi: 10.1007/s10237-020-01299-3. URL https://doi.org/10.1007/s10237-020-01299-3.

[107] Fuzhang Zhao. Optimal relaxation collisions for lattice boltzmann methods. *Computers and Mathematics with Applications*, 65(2):172 – 185, 2013. ISSN 0898-1221. doi: https://doi.org/10.1016/j.camwa.2011.06.005. URL http://www.sciencedirect.com/science/article/pii/S0898122111004731. Special Issue on Mesoscopic Methods in Engineering and Science (ICMMES-2010, Edmonton, Canada).

[108] Kai Zhao and Jianbo Jiang. What is normal nasal airflow? a computational study of 22 healthy adults. *International Forum of Allergy & Rhinology*, 4(6):435–446, March 2014. doi: 10.1002/alr.21319. URL https://doi.org/10.1002/alr.21319.

[109] Kai Zhao, Peter Scherer, Shoreh Hajiloo, and Pamela Dalton. Effect of anatomy on human nasal air flow and odorant transport patterns: Implications for olfaction. *Chemical senses*, 29:365–79, 06 2004. doi: 10.1093/chemse/bjh033.

[110] Guo Zhao-Li, Zheng Chu-Guang, and Shi Bao-Chang. Non-equilibrium extrapolation method for velocity and pressure boundary conditions in the lattice boltzmann method. *Chinese Physics*, 11(4):366–374, mar 2002. doi: 10.1088/1009-1963/11/4/310. URL https://doi.org/10.1088%2F1009-1963%2F11%2F4%2F310.

[111] Qisu Zou and Xiaoyi He. On pressure and velocity boundary conditions for the lattice boltzmann bgk model. *Physics of Fluids*, 9(6):1591–1598, 1997. doi: 10.1063/1.869307. URL https://doi.org/10.1063/1.869307.

[112] Mohammad Zuber, Vizy Nazira Riazuddin, M.Z. Abdullah, Rushdan Ismail, Ibrahim Lutfi Shuaib, Suzina Sheikh Ab Hamid, and Kamarul Ahmad. Airflow inside the nasal cavity: Visualization using computational fluid dynamics. *Asian Biomedicine*, 4:657–661, 08 2010. doi: 10.2478/abm-2010-0085.

[113] Jens Zudrop, Sabine Roller, and Pietro Asinari. Lattice boltzmann scheme for electrolytes by an extended maxwell-stefan approach. *Phys. Rev. E*, 89:053310, May 2014. doi: 10.1103/PhysRevE.89.053310. URL https://link.aps.org/doi/10.1103/PhysRevE.89.053310.

[114] David Zwicker, Kai Yang, Simone Melchionna, Michael P Brenner, Bob Liu, and Robin W Lindsay. Validated reconstructions of geometries of nasal cavities from CT scans. *Biomedical Physics & Engineering Express*, 4(4):045022, June 2018. doi: 10.1088/2057-1976/aac6af. URL https://doi.org/10.1088/2057-1976/aac6af.

Appendices

A | Binary update functions in Lattice Gas Automata

Cellular automaton is an algorithm that, in general, examines its state and the state of the neighbouring cells to describe its state in the next time step, often via a simple update rule or function. In this case, a very simple variation is explained: a 1-dimensional version with cells either being 0 or 1 and its updating function is only dependent on the direct neighbouring cells:

$$s_{i,t+1} = \Phi(s_{i-1,t}, s_{i,t}, s_{i+1,t}) \tag{A.1}$$

with Φ the update function and t a given time step. There are $2^3 = 8$ different states in which these cells can be. Since the new state of a cell is either 0 or 1, there are $2^8 = 256$ possible update functions.
It is possible to describe the update functions using the decimal numbers in binary from 00000000 (0) to 11111111 (255). By taking the exponents of the binary number and using the relation $n = 4 * n_1 + 2 * n_2 + 1 * n_3$, the new state can be determined with a given state for any binary number within the range by solving for n_1, n_2 and n_3 with $\Phi(n_1, n_2, n_3)$. The new state is then given by taking the value matching exponent in the binary number. To explain this, the binary number 01100110 is taken as an example update function.
The right most exponent is 0 in binary, so the equation has to be equal to 0. This gives the equation:

$$n = 0 = 4 * 0 + 2 * 0 + 1 * 0 \tag{A.2}$$

Expressed in the update function, this can be written as $\Phi(0, 0, 0)$. The value of the right most digit in 01100110 is 0, so $\Phi(0, 0, 0) = 0$. The second binary solves the equation by equalling it to 1, since the second binary represents 2^1. Solving the equation gives:

$$n = 1 = 4 * 0 + 2 * 0 + 1 * 1 \tag{A.3}$$

Expressed in the update function, this can be written as $\Phi(0, 0, 1)$. The value of the second right digit in 01100110 is 1, so $\Phi(0, 0, 1) = 1$. For the given example function with binary number 01100110, all new states can be expressed as:

$$\begin{aligned}
\Phi(0,0,0) &= 0\\
\Phi(0,0,1) &= 1\\
\Phi(0,1,0) &= 1\\
\Phi(0,1,1) &= 0\\
\Phi(1,0,0) &= 0\\
\Phi(1,0,1) &= 1\\
\Phi(1,1,0) &= 1\\
\Phi(1,1,1) &= 0
\end{aligned}$$

which gives 01100110 again when reading from top to bottom.

B | Nasal geometry grid convergence

A complete grid convergence study has not been conducted. Instead, a scaled breathing profile is used that is 8 times smaller in amplitude. The behaviour is studied for mesh sizes with a grid spacing of $h = 0.20, 0.175, 0.15, 0.125, 0.10, 0.09$ and 0.075 mm which corresponds with mesh sizes of $12.2\mathrm{k}$, $18.4\mathrm{k}$, $29.5\mathrm{k}$, $51.3\mathrm{k}$, $101\mathrm{k}$, $139\mathrm{k}$ and $241\mathrm{k}$.

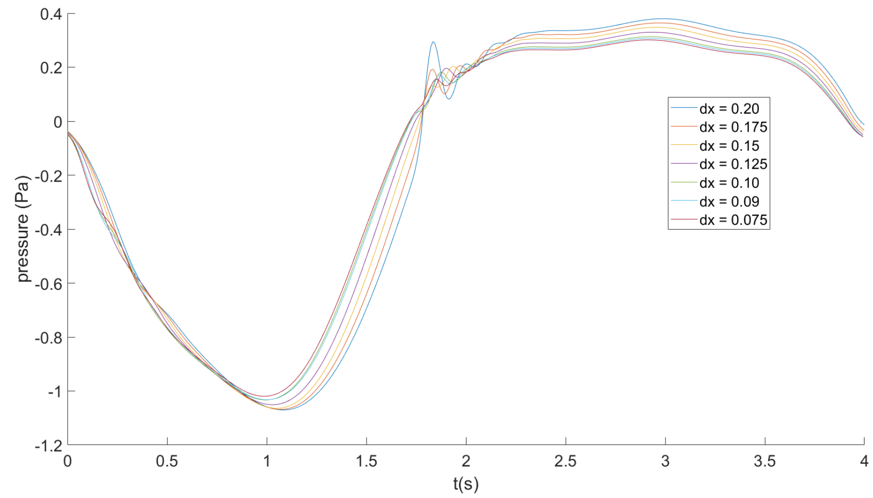

Figure B.1: Relative pressure (Pa) with respect to the nostril boundary pressure at point 11 for different grid sizes.

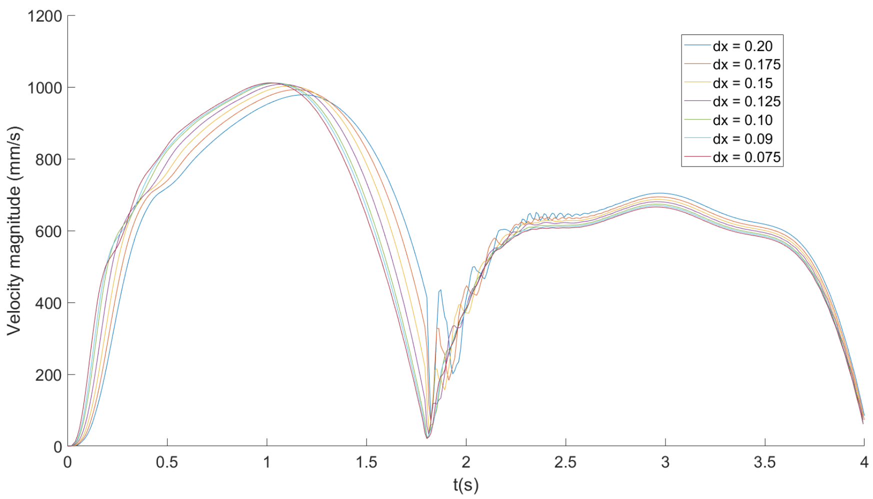

Figure B.2: Velocity magnitude $(\mathrm{mm/s})$ at point 11 for the scaled case with different grid sizes.

C | Final Mesh

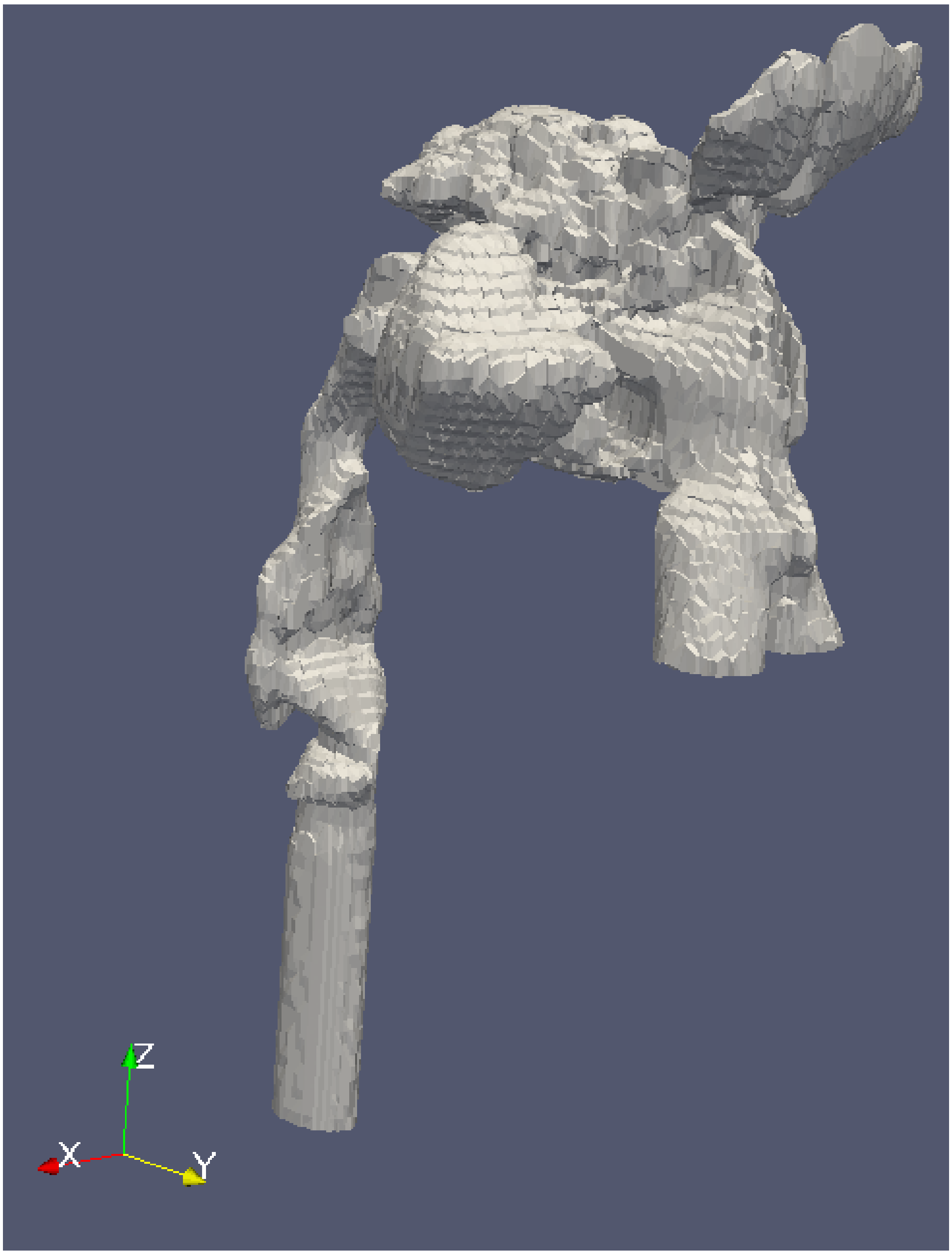

Figure C.1: Coarse mesh with extended inlet and outlet to illustrate the configuration at inhalation.

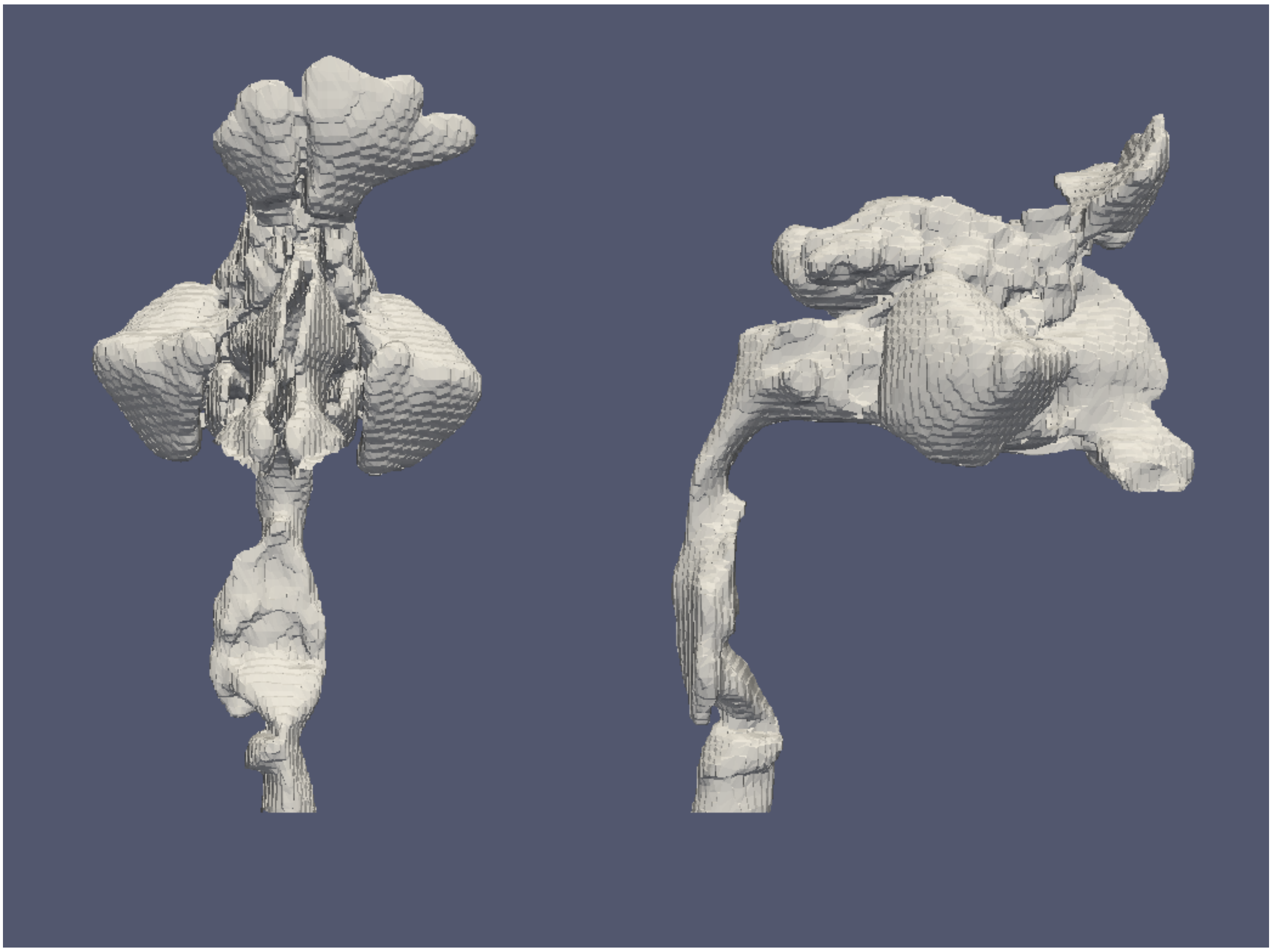

Figure C.2: Coarse mesh without extended inlet and outlet to illustrate the configuration at expiration.

D | Extra images of unassisted breathing

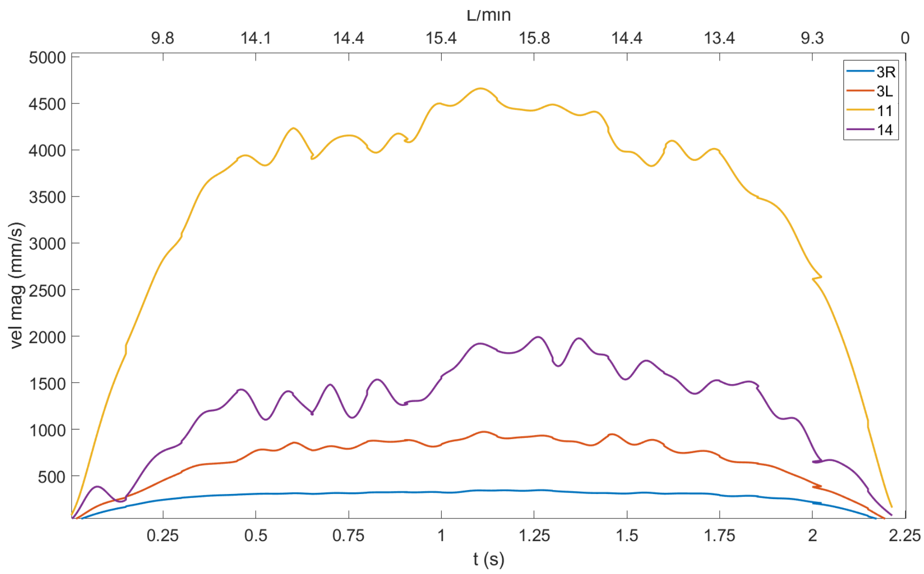

Figure D.1: Velocity magnitude $(\mathrm{mm/s})$ over time at several points in the geometry during exhalation. Low-pass filter was applied with 2.5 Hz cut-off frequency.

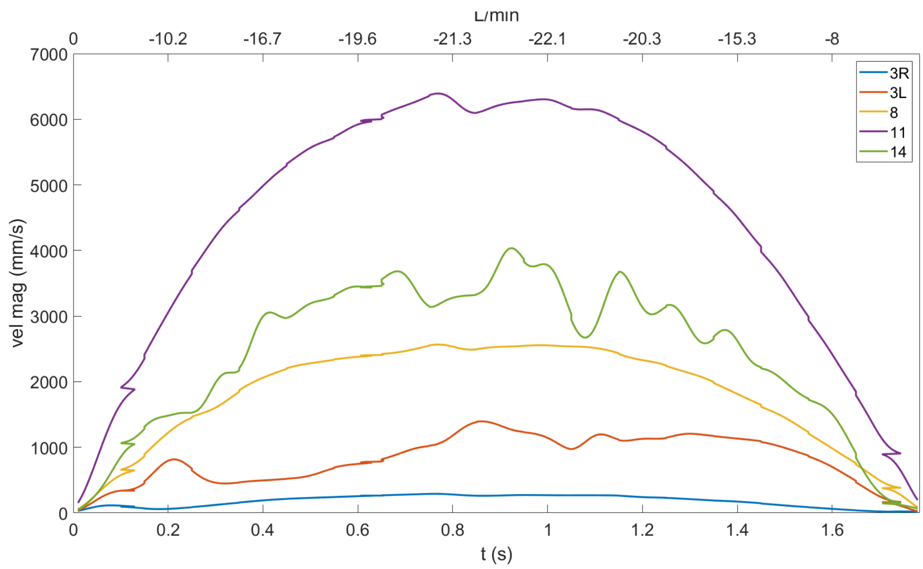

Figure D.2: Velocity magnitude $(\mathrm{mm/s})$ over time at several points in the geometry during inhalation. Low-pass filter was applied with 2.5 Hz cut-off frequency.

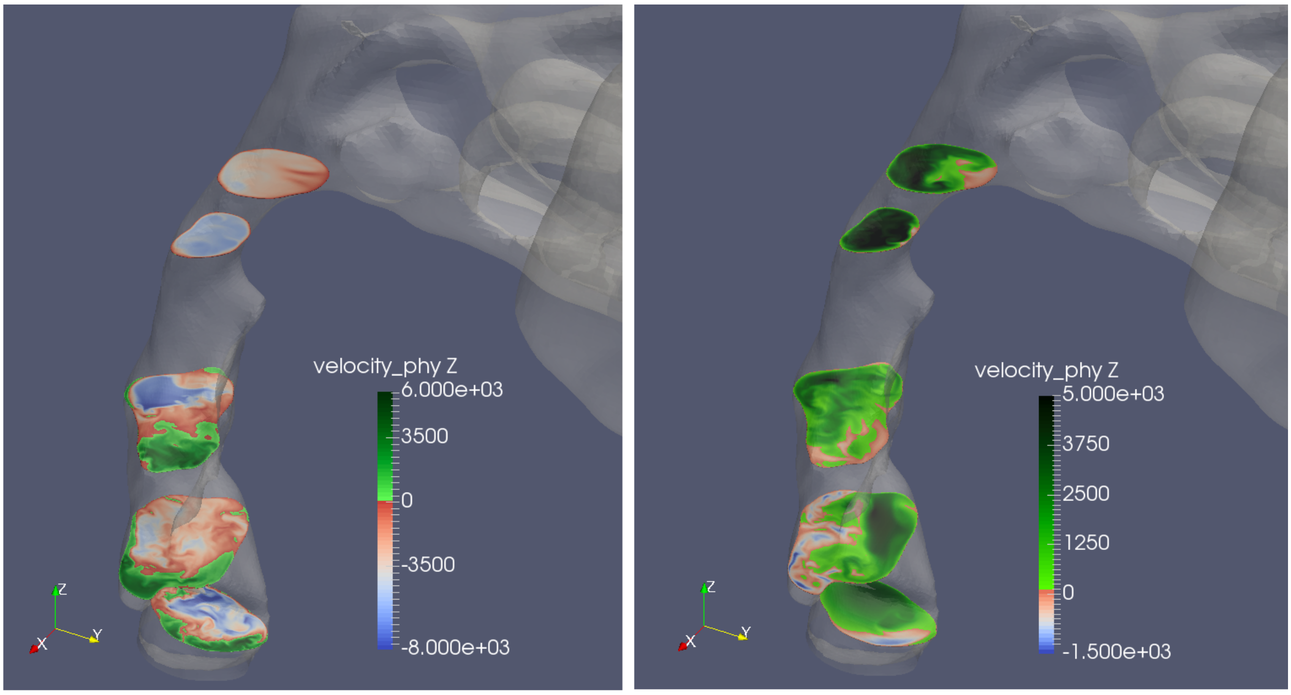

Figure D.3: Speed $(\mathrm{mm/s})$ in z-direction at maximum inspiration. Positive speed in green scale. Left: peak inhalation. Right: peak expiration.

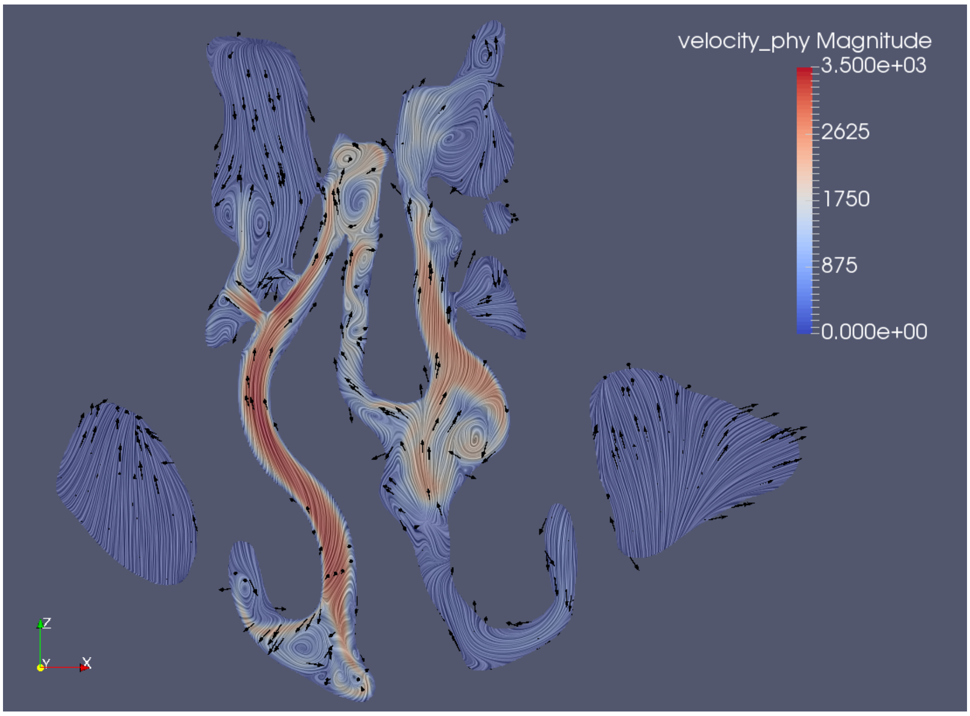

Figure D.4: Line integral convolution plot of the velocity vector $(\mathrm{mm/s})$ in the V2 plane during peak inhalation. Posterior point of view.

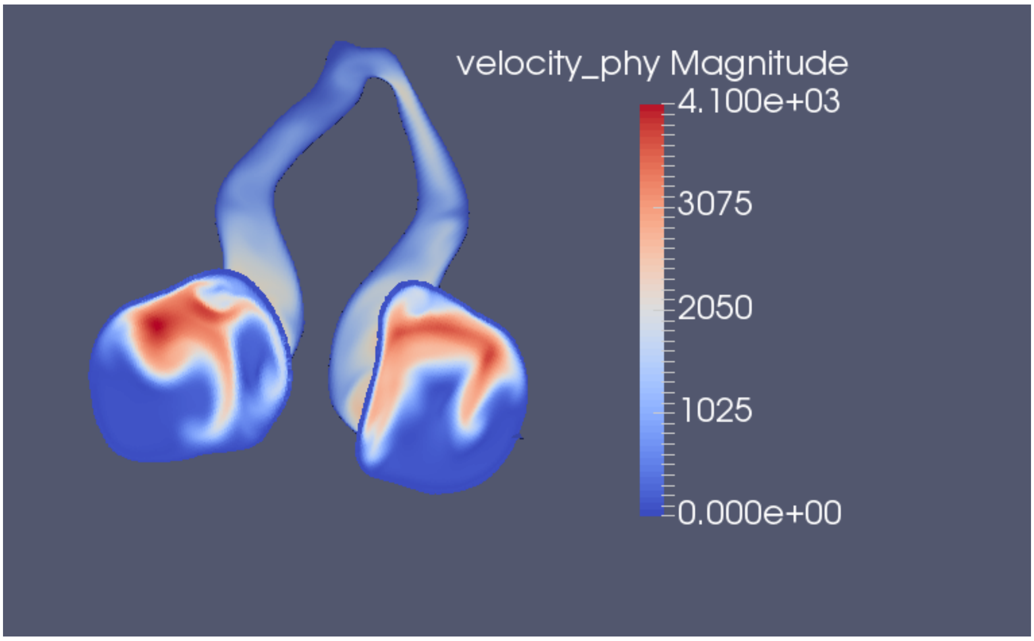

Figure D.5: Velocity magnitude $(\mathrm{mm/s})$ at the nostril boundary outlet at peak expiration (t=1.15 s)

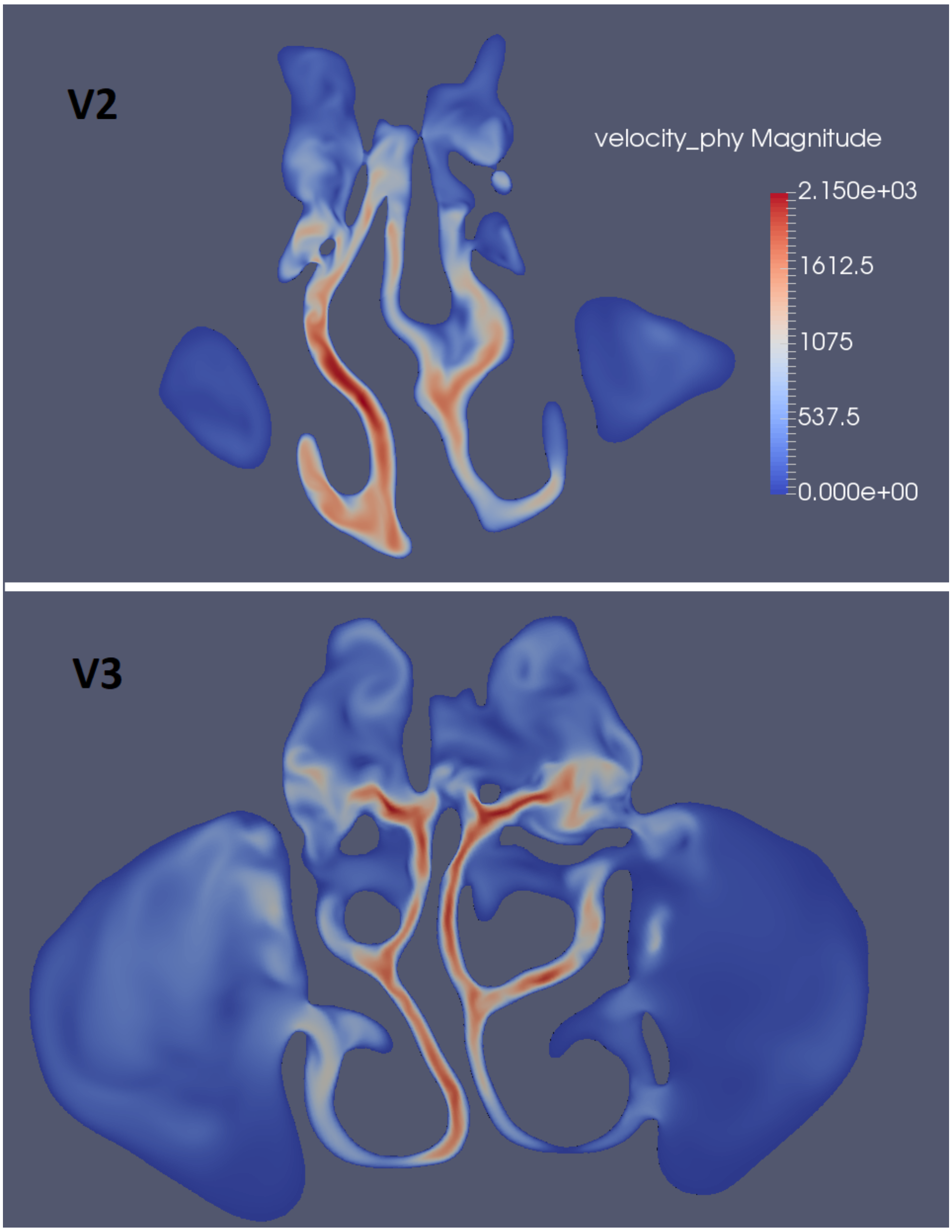

Figure D.6: Velocity magnitude $(\mathrm{mm/s})$ in the V2 and V3 plane at peak expiration. Posterior point of view

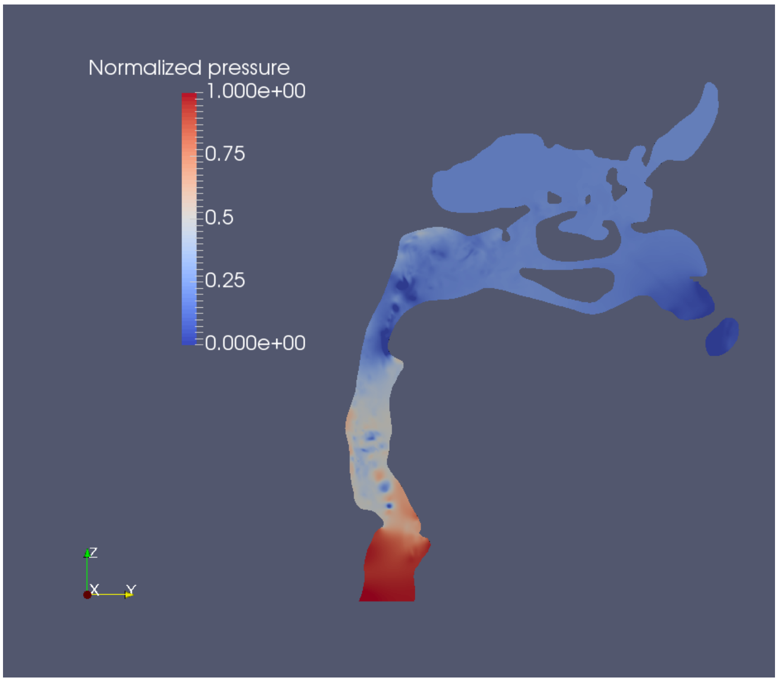

Figure D.7: Contour of the normalized pressure $\frac{P-P_{nostril}}{P_{trachea}-P_{nostril}}$ at peak expiration.

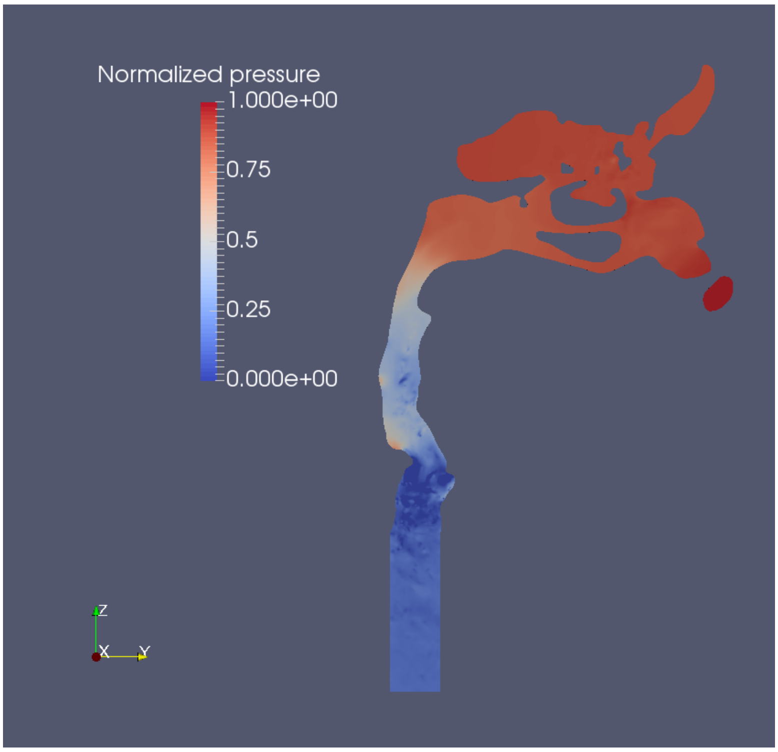

Figure D.8: Contour of the normalized pressure $\frac{P-P_{nostril}}{P_{trachea}-P_{nostril}}$ at peak inspiration.

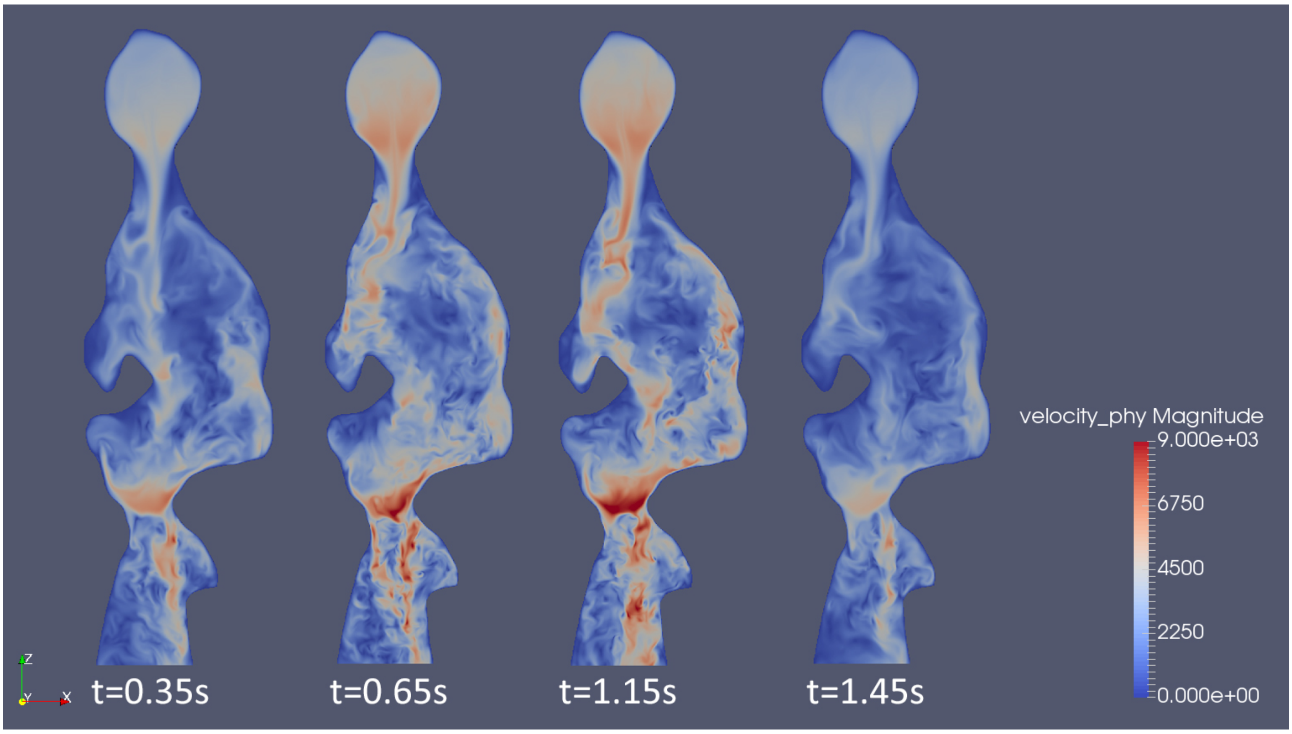

Figure D.9: Velocity magnitude $(\mathrm{mm/s})$ over time in pharynx and larynx plane (Plane V11 in figure 5.1) during inhalation.

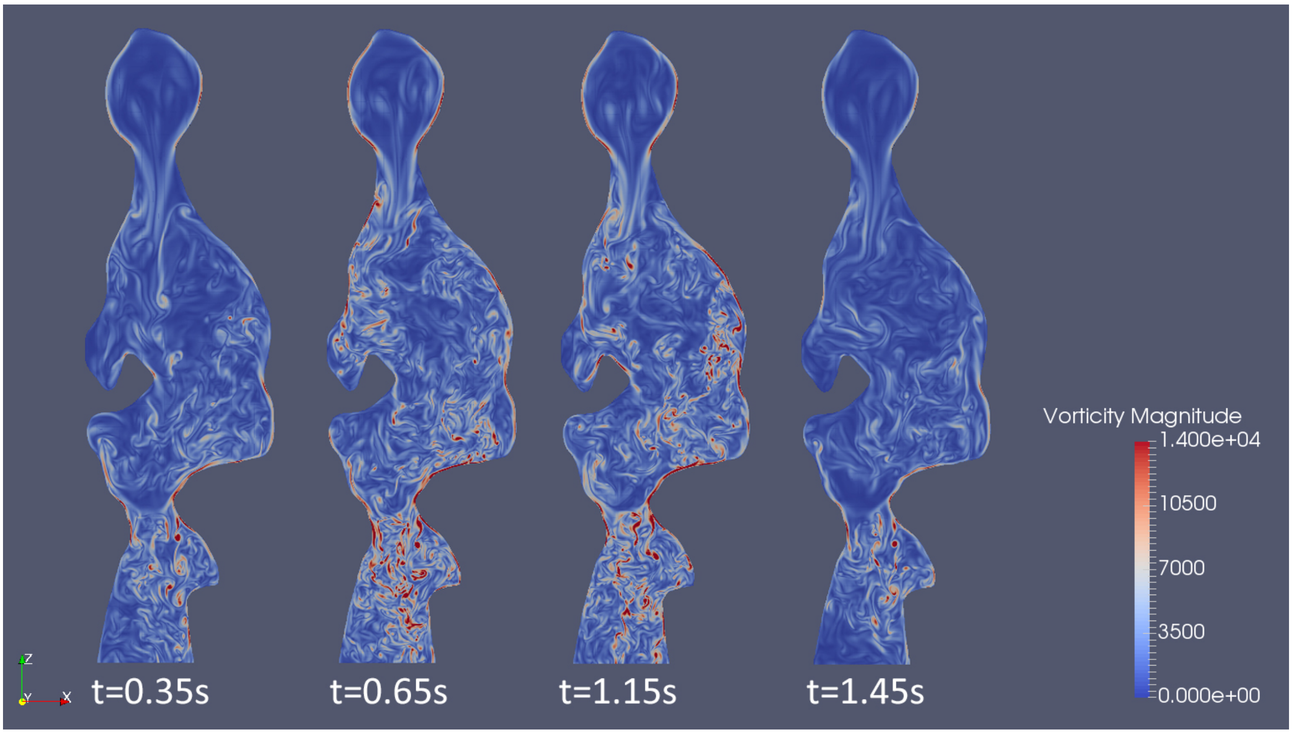

Figure D.10: Vorticity magnitude $(1/\mathrm{s})$ over time in pharynx and larynx plane (Plane V11 in figure 5.1) during inhalation.

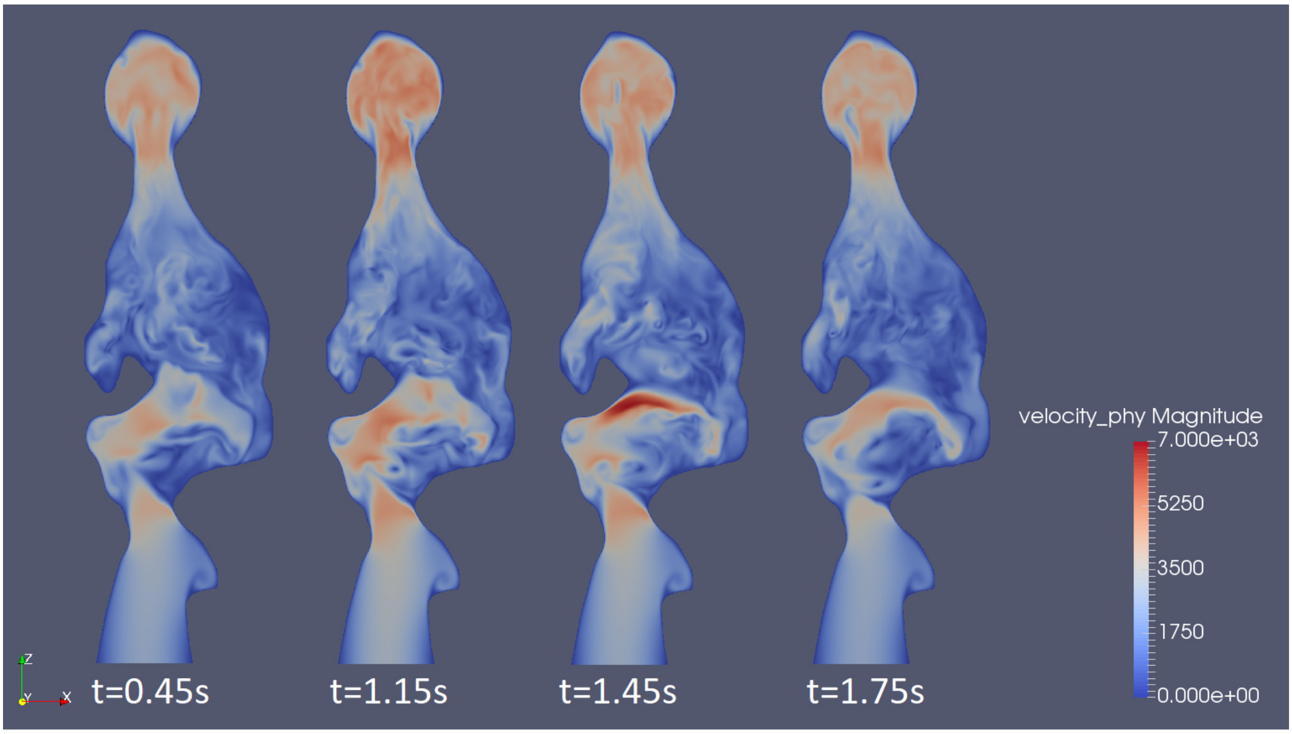

Figure D.11: Velocity magnitude $(\mathrm{mm/s})$ over time in pharynx and larynx plane (Plane V11) during exhalation.

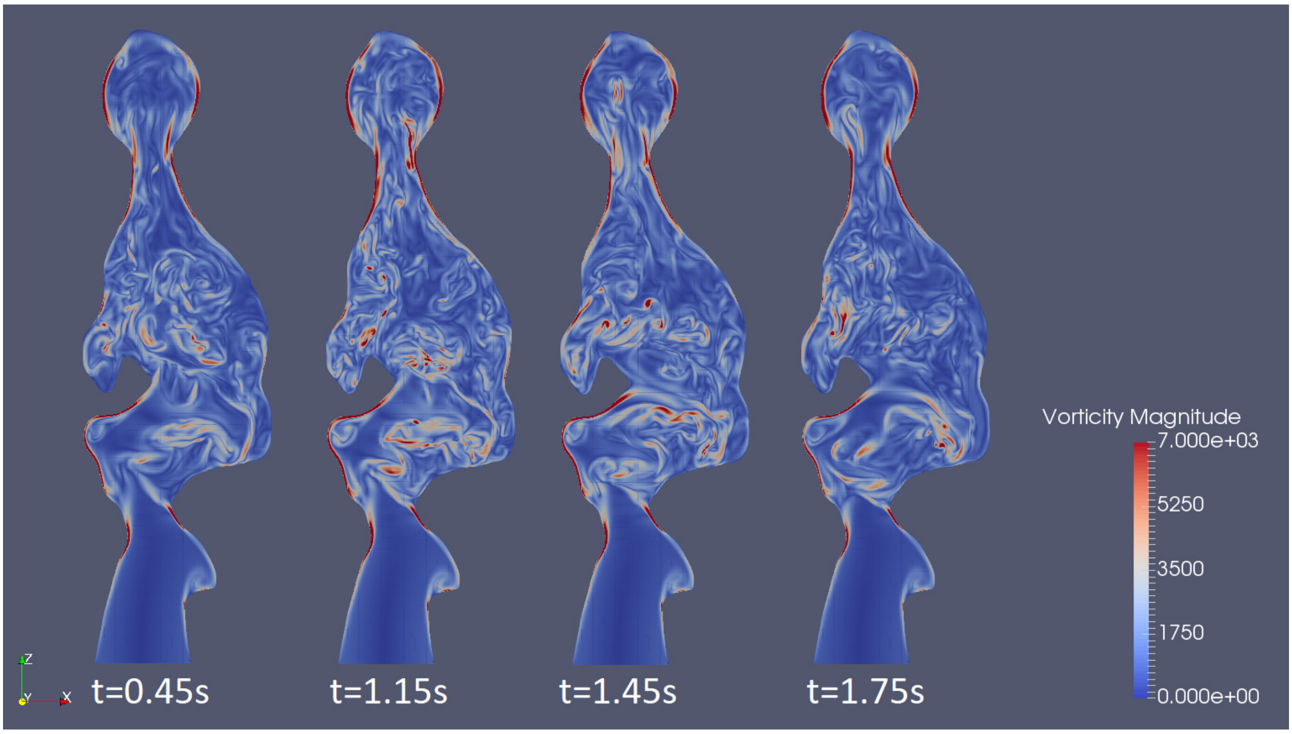

Figure D.12: Vorticity magnitude $((1/\mathrm{s}))$ over time in pharynx and larynx plane (Plane V11) during exhalation.

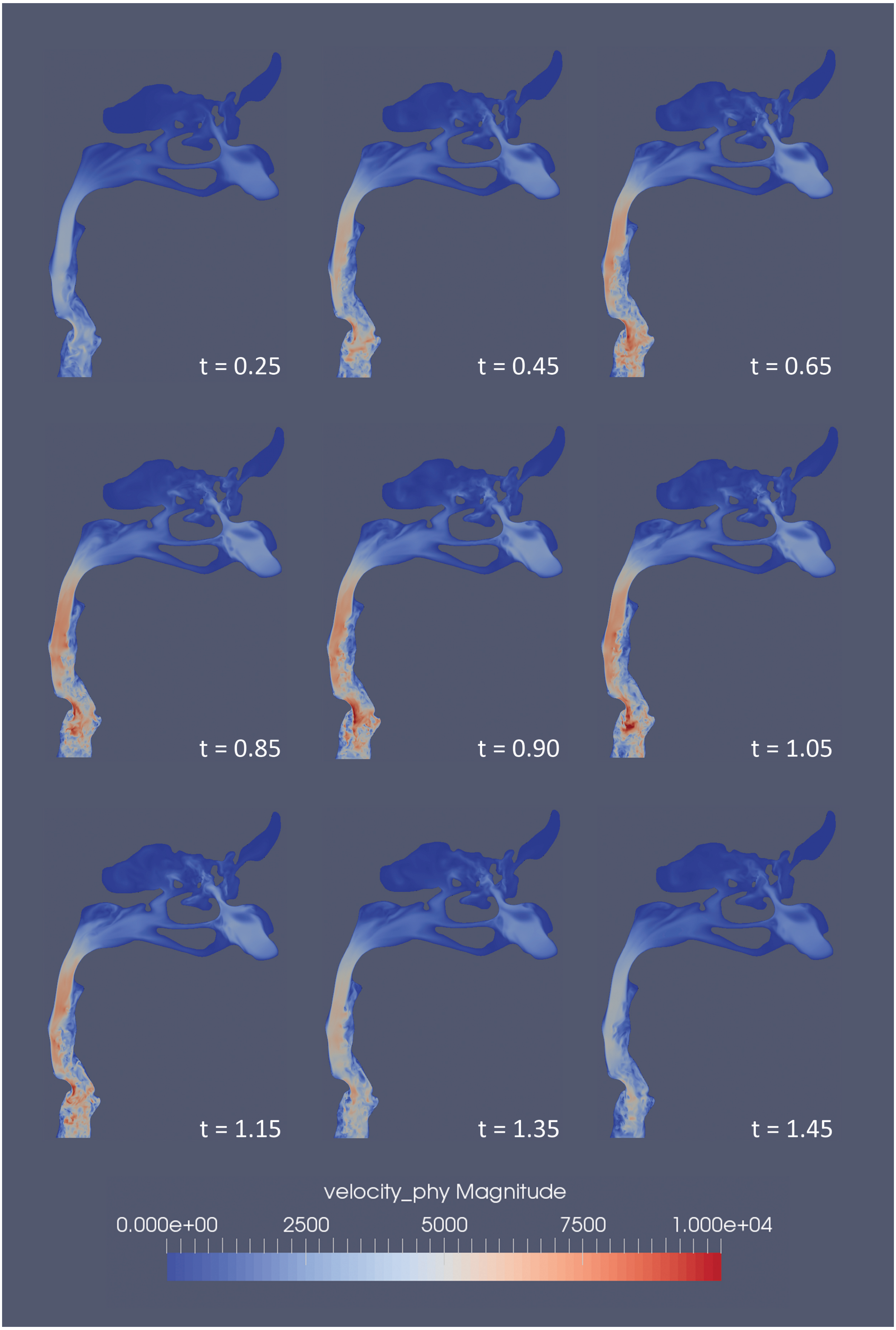

Figure D.13: Velocity magnitude $(\mathrm{mm/s})$ over time at plane 3R during inhalation

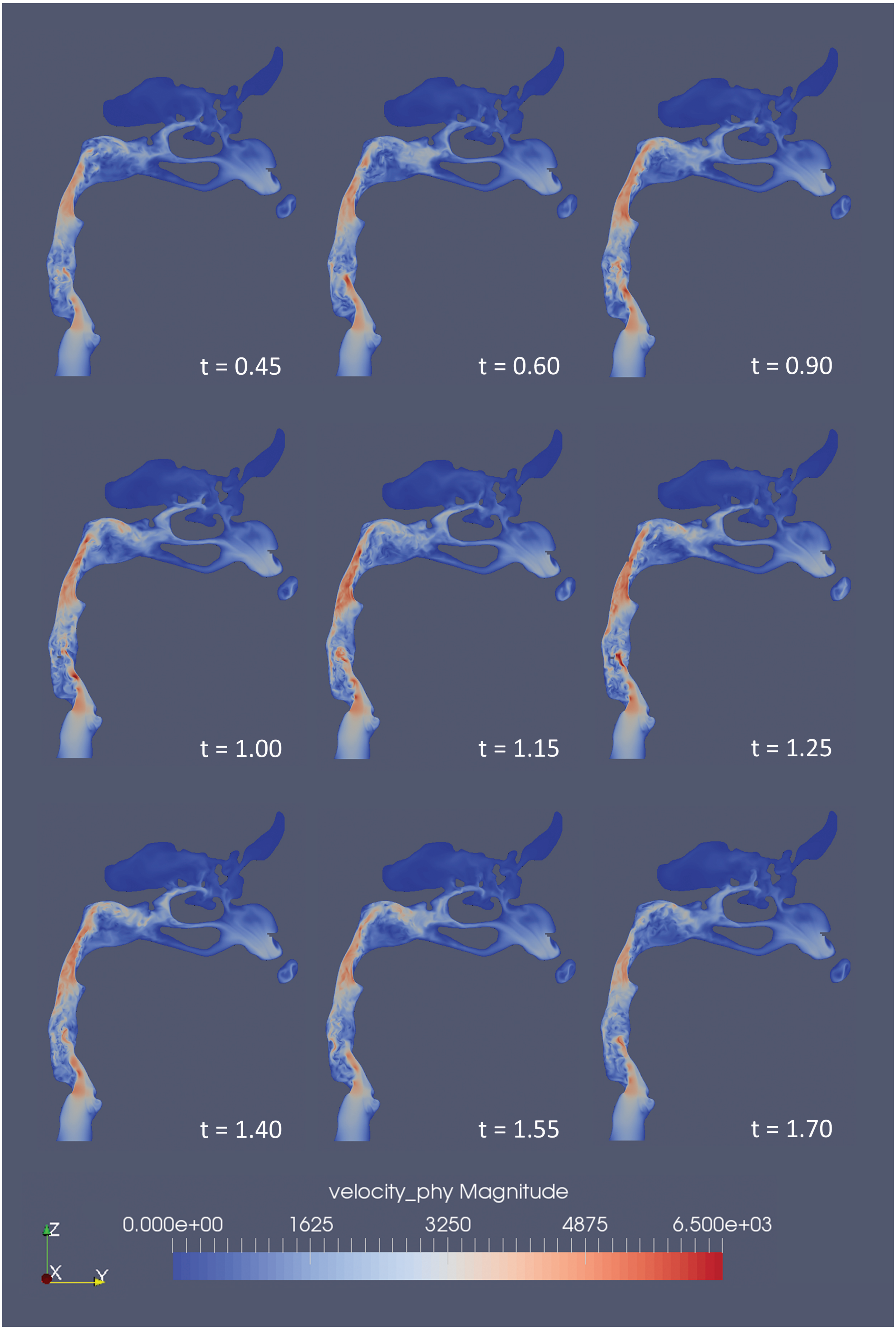

Figure D.14: Velocity magnitude $(\mathrm{mm/s})$ over time at plane 3R during exhalation

D.1 Discussion

Figures D.15 and D.16 show the pressure difference between the pressure over a line and the mean nostril pressure. It can be seen that the pressure results obtained at both walls (start and end of the plot) are quite different than the pressure results in the middle of the geometry due to local turbulent behaviour. Pressure during experiments are measured at the walls while pressure at the simulations are measured in the middle of the geometry, which therefore show small deviations.

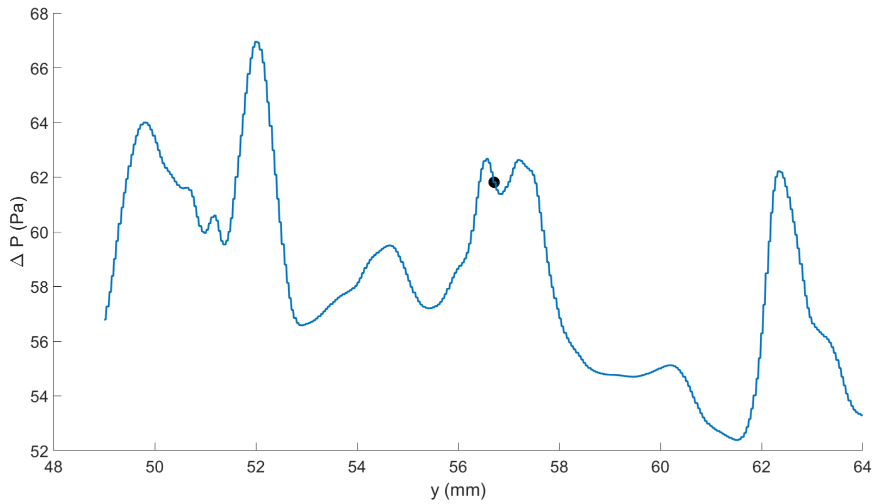

Figure D.15: Plot of the pressure drop (Pa) at the line between the points [83.5 49 40] and [83.5 64 40] at peak inspiration. The black dot represents the place of point 16, the most left location is the place where pressure is measured in experiments.

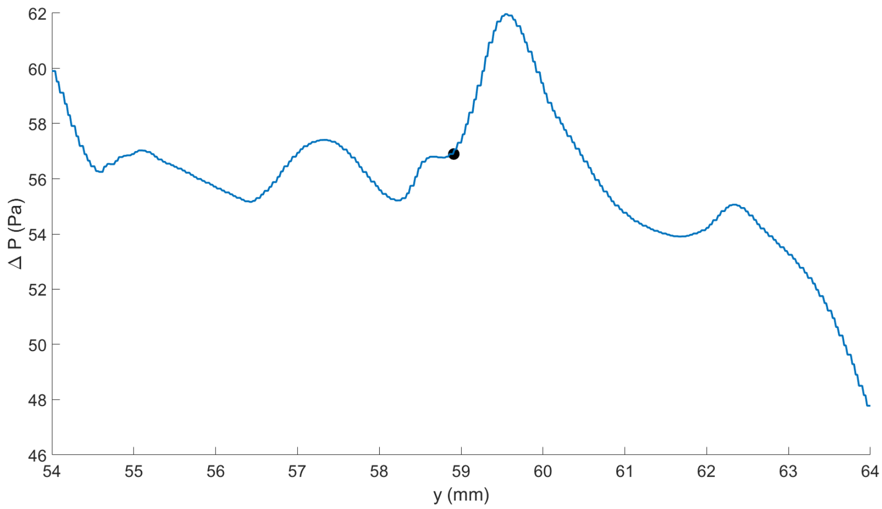

Figure D.16: Plot of the pressure drop (Pa) at the line between the points [83.5 54 50] and [83.5 64 50] at peak inspiration. The black dot represents the place of point 15, the most left location is the place where pressure is measured in experiments.